DIPLOMARBEIT

Ion-induced surface modifications investigated with scanning probe microscopies

ausgeführt am

Institut für Allgemeine Physik

der Technischen Universität Wien

unter Anleitung von

Ao. Univ.-Prof. Dr. Friedrich Aumayr

und Univ.-Ass. Dr. Ille C. Gebeshuber

als verantwortlich mitwirkender Universitätsassistentin

durch

Robert Ritter

Rallenweg 32

1220 Wien, Österreich

Wien, am 02.04.2008

Abstract

The aim of this diploma thesis was the investigation of ion-induced surface modifications with scanning probe microscopies, namely atomic and magnetic force microscopy and scanning tunneling microscopy. Investigated effects were nano-hillock formation on insulator crystals (CaF_2) as well as on lamellar materials (HOPG and mica) induced by the impact of slow highly charged ions; magnetic force microscopy was used to study ion-induced magnetic transitions in thin films of Fe grown on a Cu single crystal.

The formation of nano-sized hillocks is linked to the potential energy of the incident ions and only recently a threshold for hillock production on CaF_2 was found. Experiments were performed at very low kinetic energies to prove the dependence on potential energy and to corroborate previous results. HOPG and mica were irradiated to possibly discover shifts in potential energy threshold due to the lamellar structure of the materials. For all samples and charge states, dimensions of the found hillocks were determined in a defined manner. Furthermore the efficiency, i.e. the number of defects produced per incident ion, was evaluated.

The structural and magnetic properties of ultrathin Fe films grown by thermal deposition on Cu(100) substrate depend on film thickness. In a regime of 5 - 10 monolayers, the films show an out-of-plane surface ferromagnetism below room temperature because of a surface reconstruction and an fcc (face-centered cubic) structure at room temperature with no magnetic moment. Ion bombardment influences the film structure, resulting in a transformation of the fcc phase to a bcc (body-centered cubic) phase, coupled with a change in magnetic phase. Magnetic force microscopy allows for investigation of this effect on the nano-scale.

Kurzfassung

Das Ziel dieser Diplomarbeit war die Untersuchung ionen-induzierter Oberflächenverän-
derungen mittels rastersondenmikroskopischer Methoden, nämlich Kraftmikroskopie und
Tunnelmikroskopie. Untersucht wurde die Entstehung von Nanodefekten ("Hillocks")
auf Isolatorkristallen (CaF_2) sowie auf geschichteten Materialien (HOPG und Glimmer)
durch langsame hochgeladene Ionen; magnetische Kraftmikroskopie wurde zur Unter-
suchung ionen-induzierter magnetischer Phasenübergänge in dünnen Fe Filmen herange-
zogen, die auf einem Cu-Einkristall aufgedampft wurden.

Die Entstehung von Hillocks ist an die potentielle Energie der einfallenden Ionen gekop-
pelt und es wurde erst kürzlich eine Energieschwelle für die Erzeugung auf CaF_2 ent-
deckt. Experimente wurden bei äußerst niedrigen kinetischen Energien durchgeführt, um
die Abhängigkeit von der potentiellen Energie zu zeigen und vorangegangene Ergebnisse
zu bestätigen. HOPG und Glimmer wurden bestrahlt um mögliche Verschiebungen der
Energieschwelle zu finden, die durch die Schichtstruktur der Materialien bedingt werden.
Für alle Proben und Ladungszustände wurden die Dimensionen der gefundenen Hillocks
nach einem festgelegten Schema ausgewertet. Zusätzlich wurde die Effizienz, die Anzahl
der Defekte pro Ion, berechnet.

Die strukturellen und magnetischen Eigenschaften von Eisenschichten, die auf Cu(100)-
Substrat aufgedampft werden, hängen von ihrer Dicke ab. Im Bereich von 5 - 10 Mono-
lagen zeigen die Filme unterhalb der Raumtemperatur Oberflächen-Ferromagnetismus
normal zur Oberfäche bedingt durch eine Rekonstruktion und bei Raumtemperatur eine
fcc (face-centered cubic) Kristallstruktur ohne magnetisches Moment. Ionenbeschuss
beeinflusst die Filmstruktur und führt zu einer Umwandlung der fcc Struktur in eine
bcc (body-centered cubic) Struktur, gekoppelt mit einer Änderung der magnetischen
Phase. Magnetische Kraftmikroskopie ermöglicht eine Untersuchung dieses Effekts auf
der Nanoskala.

Contents

1 Introduction

1.1 Motivation and research

The idea of modifying surfaces on the nanoscale in a defined and reproducible way, for example "writing" on a surface, has captured the interest of researchers for some time [1]. Among the tools for such lithographic surface modification, although perhaps the least developed technique in the field, are ion beams [2]. This is partly due to the not yet fully understood interaction mechanisms between ions and surfaces.

Due to primarily technical reasons, earlier studies on ion-surface interactions were mainly conducted at relatively high kinetic energies and low ion charge states. Swift heavy ion (MeV - GeV) irradiation of solid targets has been extensively studied and shown to induce severe structural modifications not only at the surface but also in the bulk ([3], [4]). For several ionic fluoride single crystals, e.g. LiF, CaF_2, BaF_2, the occurrence of nanoscopic protrusions (hillocks) has been reported ([5] - [8]) and their dimensions evaluated by means of atomic force microscopy (AFM). Formation of these hillocks, however, sets in only above a critical electronic energy loss of the swift ions. Above this threshold ($\sim$ 5 keV/nm) both diameter and height of the hillocks increase with increasing electronic stopping power [6]. The above mentioned damage of deeper layers is a major limitation for the use of high-energy ions in nanotechnological applications.

Research in the field of slow (eV - keV) highly charged ions (HCI) and their interaction with surfaces has been fueled by the desire to confine energy deposition to the topmost surface layers and the continuous development in ion source technology and scanning probe microscopy.

HCI carry a large amount of potential energy which is equal to the total ionization energy required for their production [1]. It is nowadays possible to perform experiments where the potential energy of the incident projectiles becomes comparable with or even greatly exceeds their kinetic energy. In such a way, "potential effects" become dominant and any "kinetic effects" play a less important role. The larger part of this work is dedicated to the investigation of hillock formation under such conditions on different target materials, namely CaF_2, HOPG and mica.

Experimental evidence will be given that the size of the generated nanostructures depends heavily on the potential energy of the impinging ions, whereas the kinetic energy has very little influence. Furthermore, a variety of materials (e.g. CaF_2, LiF, mica) exhibit a more or less sharp potential energy threshold ([2], [9]), similar to the case of swift heavy ions, above which hillock formation sets in.

Special interest has been drawn by CaF_2 since it is widely used as an insulator material in the semiconductor industry. Eventually, findings might be of importance for high resolution patterning of thin CaF_2 films on Si and for the creation of nanostructured templates for adlayer growth during fabrication of CaF_2/Si based epitaxial insulator-semiconductor structures [9].

Another emerging research field in ion-beam lithography is the patterning of ultrathin magnetic films which has a huge potential for ultra-high density magnetic recording [10]. Thin Fe films (5 - 10 monolayers) grown epitaxially on a Cu(100) single crystal adopt the face-centered cubic (fcc) structure of the underlying substrate although the stable bulk structure of Fe is body-centered cubic (bcc). The films show an out-of-plane surface ferromagnetism with Curie temperatures below room temperature which can be related to a surface reconstruction but no magnetic moment at and above room temperature.
Ion bombardment of the films, however, influences the film structure and results in a phase transition from fcc structure to ferromagnetic bcc structure with in-plane magnetic anisotropy. This change of magnetic properties can be neatly observed by means of a surface magneto-optic Kerr effect (SMOKE) system. SMOKE measurements, however, require a sufficiently large irradiated surface area since resolution is limited by the beam diameter of the laser employed in the system.
In the course of this work, first exploratory investigations were performed with magnetic force microscopy (MFM) to observe the effect on the nanoscale using Fe-Cu samples patterned with an Ar^+ focused ion beam (FIB).

1.2   About this work

Both effects investigated in this work (hillock formation and magnetic phase transition) are ion-induced phenomena. In the following, a short summary of each chapter and its relation to the experimental work is given.

In chapter 2 the interaction of (highly charged) ions with various target materials is discussed and linked to the applicability of HCI as nanostructuring tools.

Information about the structural and magnetic properties of ultrathin Fe films grown on a Cu(100) single crystal and how these properties change under ion bombardment are given in chapter 3.

Chapter 4 describes the experimental methods that have set the stage for HCI/surface interaction studies and have been a part of the presented experimental work, i.e. sources for HCI and scanning probe microscopies.

As the experiments performed on hillock formation are a continuation and extension of previous studies on the respective materials, a detailed summary of the state of the art in this field is given in chapter 5.

In the results chapter 6, obtained scanning probe microscopy data will be presented and evaluated: AFM results of the hillock formation on CaF_2, mica and HOPG and MFM results of the ion-induced magnetic phase transition in the Fe/Cu system.

Finally, in chapter 7 the obtained results will be summarized and possible applications as well as directions of future research will be discussed.

Parts of this diploma thesis have meanwhile been submitted for publication:

1. *Creation of nano-hillocks on CaF_2 surfaces by single slow highly charged ions,*
   A. S. El-Said, R. Heller, W. Meissl, R. Ritter, S. Facsko, C. Lemell, B. Solleder,
   I. C. Gebeshuber, G. Betz, M. Toulemonde, W. Möller, J. Burgdörfer
   and F. Aumayr

2. *Ion-beam induced ferromagnetism of ultrathin Fe films,*
   W. Rupp, B. Kamenik, R. Ritter, A. Biedermann, Ch. Klein, E. Platzgummer,
   M. Schmid and P. Varga

2 Interaction of ions with surfaces

2.1 Ions

Ions in low charge states are easy to produce and thus have been subject to experimental investigation for a long period of time. Contrary to neutral particles, they can be easily guided by electric and magnetic fields. The production of highly charged ions, however, is a more sumptuous undertake. Fast highly charged ions can be produced by "stripping", i.e. removing the electrons of ions in lower charge states via bombardment of thin films. Since the development of the EBIT (electron beam ion trap) and the ECRIS (electron cyclotron resonance ion source), it has become possible to perform experiments with slow HCI. Since these inventions are of fundamental importance for the realization of the investigations made throughout this work, they are described in detail in section 4.1.

2.1.1 Energy deposition - Definition of slow highly charged ions

Ions carry internal (potential) energy, according to their production. For an ion of charge state q, q electrons must be removed from the neutral atom. For every removal the ionization energy of the respective electron is required, which increases considerably as deeper shells are reached. The total ion potential energy can thus be written as the sum of all ionization energies E^i of the removed electrons:

$$W_{pot,q} = \sum_{j=1}^{q-1} E_j^i \tag{2.1}$$

In Fig. 1 the ionization energies and potential energies for the noblegases Ar ($Z = 18$) and Xe ($Z = 54$), which in this work have been commonly used for irradiation experiments, are shown.

An ion of charge state q passing a potential difference ΔU gains the kinetic energy

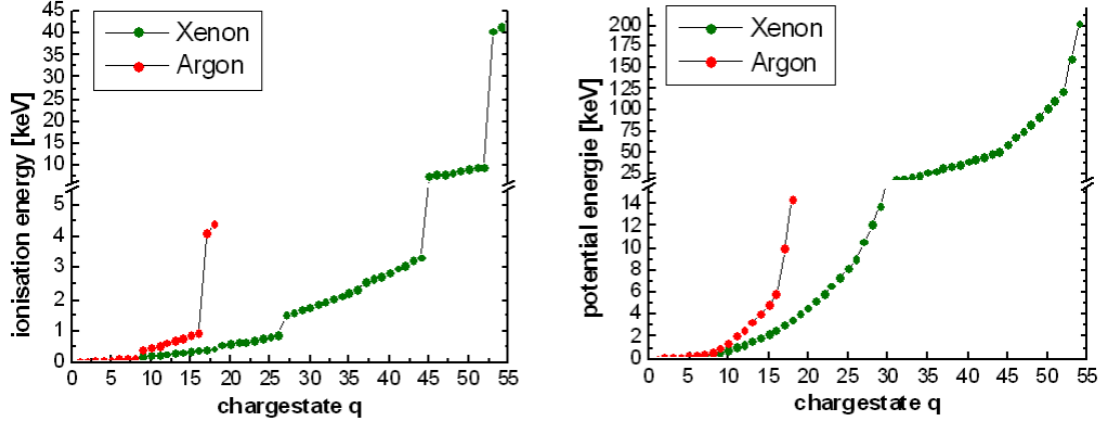$$\Delta E_{kin} = q \cdot \Delta U \ . \tag{2.2}$$

Figure 1: Ioniziation energies (left) and potential energies (right) for Argon and Xenon [21].

Nature and intensity of ion-surface interactions depend heavily on both the kinetic and the potential energy carried by the projectile [11]. Depending on the relative values of these energies, energy deposition takes place in markedly different ways.

The kinetic energy of an energetic ion penetrating the solid, can be transfered to target electrons, resulting in ionization, atomic or collective electron excitations. Alternatively the projectile may interact with target atomic cores. The kinetic energy loss of the projectile (stopping power) can therefore generally be subdivided into an "electronic" (inelastic) and a "nuclear" (elastic) part.

Nuclear stopping is the dominant mechanism in the case of slow singly charged ions or neutral atoms (case 1 in Fig. 2). The energy transfer to the target cores results in atomic displacements or excitation of phonons. Due to the low kinetic energy of the incident particles, energy deposition is restricted to the surface near region.

For swift ions or atoms (case 2 in Fig. 2), electronic stopping outweighs the scattering from target nuclei and leads to high ionization densities around the ion trajectories which are practically straight in the surface near region. Fast electrons, produced via inner shell ionization processes, can greatly enlarge the area in which electronic excitation/ionization takes place (formation of a so-called "ion-track").

Multiply charged ions (MCI, case 3 in Fig. 2), apart from their kinetic energy, can also deposit their potential energy. For very slow highly charged ions (HCI), this internal energy can approach or even exceed the kinetic energy of the ion. Transfer of the potential energy to the electronic system proceeds within a shallow region close to the impact zone. For low impact energies, energy transfer even sets in well above the target surface through various neutralization, reionization and deexcitation processes,
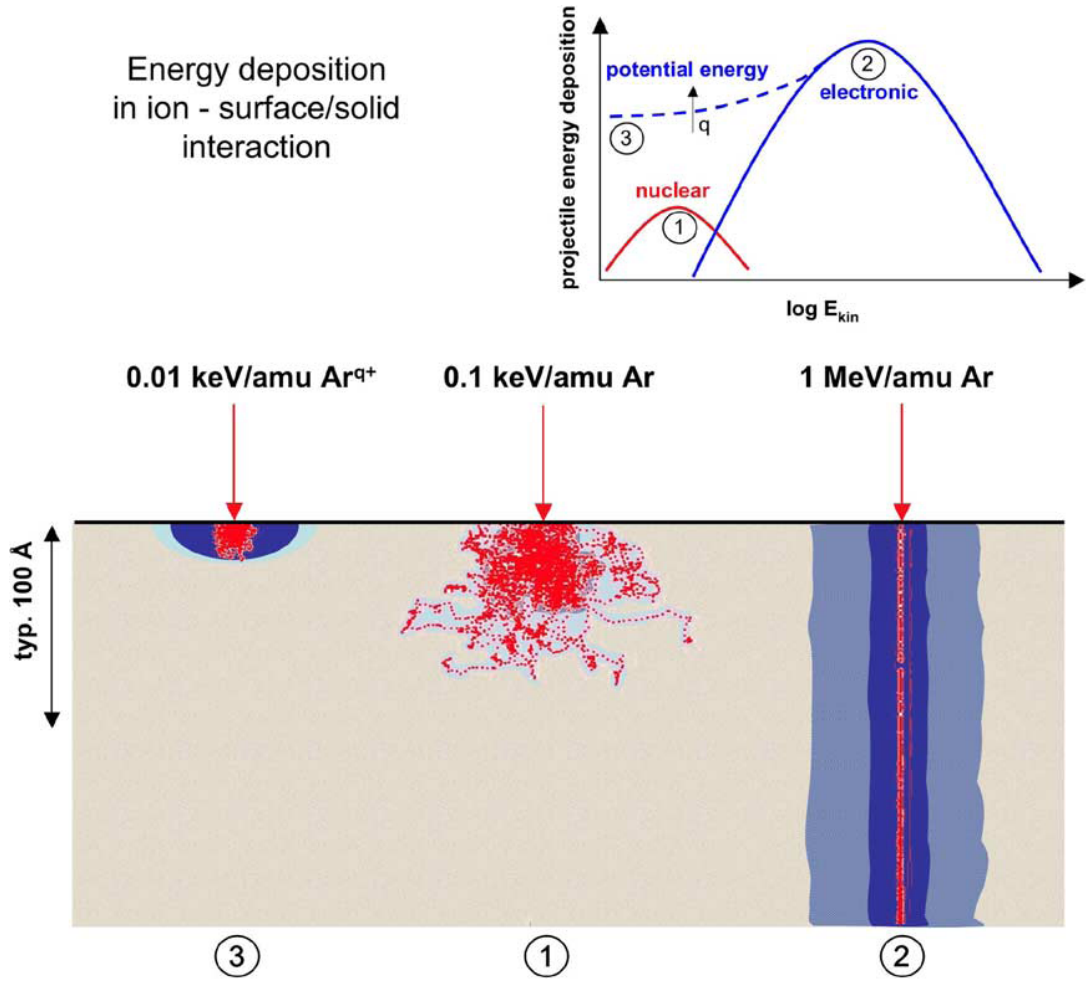
Figure 2: Energy deposition during interaction with a solid surface of slow singly charged ions or neutral atoms (1), swift ions or neutral atoms (2) and very slow multiply charged ions (3) [11].

eventually leading to the formation of exotic, so-called "hollow atoms" (see section 2.2.2 and [11], [12], [13]).

In terms of velocity, there is no general definition of "slow" projectiles. A possible definition is to set an upper limit of impact velocity, e.g. of 1 atomic unit of velocity (a.u. $= 2.18 \times 10^6$m/s) [12]. This condition corresponds to projectile energies below 25 keV per atomic mass unit (amu) and is met by all the experiments performed throughout this work. The term "highly charged ion" is usually employed, when potential energy effects are more important than those originating from kinetic energy deposition. Hence the ratio of these two energy contributions may be considered a valid definition for HCI.

2.2   Interaction processes

The bombardment of solid surfaces with ions gives rise to a multitude of processes and effects, which include:

- Electron emission

  Potential emission, kinetic emission

- Emission of photons

  Soft X-rays

- Backscattering

  Rutherford backscattering, Trampolin effect [14]

- Removal of matter

  Kinetic sputtering, potential sputtering, kinetically assisted potential sputtering, secondary ions,...

- Creation of defects/damage

  Nanostructuring, hillocks, phase transitions,....

The emphasis of this thesis is on the last point of this list, especially the formation of hillocks on different target materials as a consequence of slow HCI bombardment. Any theoretical explanation on the driving mechanism of these surface modifications requires a sound understanding of the processes involved in the interaction of slow multiply charged ions with surfaces. The investigation of these processes is of particular interest for a broad variety of research fields [12]:

- Astrophysics and cosmology (MCI-induced desorption from interplanetary and interstellar clusters and grains).

- Atomic physics of multiply excited species (hollow atom spectroscopy).

- Information technology (high-density storage media based on MCI-induced micro-structures).

- Plasma-chemistry and -technology.

- Semiconductor industry (novel cleaning procedures, e.g. preferential removal of insulating layers).

- Thermonuclear fusion reactor development (plasma wall interaction, forced radiation cooling in the plasma edge region).

The following sections give a brief summary of some of the observed effects.

2.2.1   Electron emission

In the early 1950's, pioneering work on the electron ejection as a consequence of ion bombardment of solids was done by Hagstrum, as he studied electron yields from Tungsten bombarded with singly and multiply charged ions with varying kinetic energies. Electrons may be ejected from the surface by deposition of both kinetic energy ("kinetic emission" (KE), [15], [16]) and potential energy ("potential emission" (PE), [17], [18]). From his experimental work [19] and theoretical conclusions [20], it soon became evident, that the total electron yields and energy distributions for ion-induced PE are a result of electronic transitions between the projectile and the metal surface. PE can be associated with the projectile's potential energy alone (no impact velocity threshold) and is the principal source of electron emission as long as the kinetic energy remains less important. Based on his own data and earlier studies on electron transitions between singly charged ions and metal surfaces, Hagstrum considered four electronic transitions as relevant for PE:

Resonant electronic transitions
Resonant transitions (Fig. 3) from target states to excited projectile states dominate the interaction and can take place already at quite large distance from the surface. In this case of one-electron transitions, no electrons are emitted, but they are precursors to subsequent electron-emitting transitions, which involve two electrons.
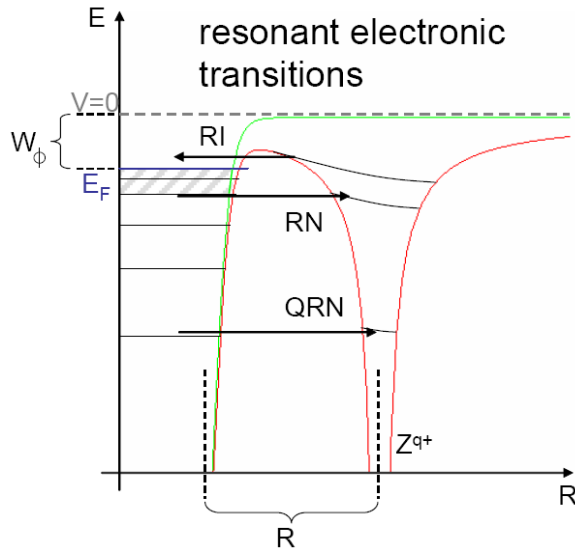

Figure 3: Schematic drawing of resonant electronic transitions. The potential curve of the solid in absence of the ion is drawn in green, the joint curve in red. Arrows indicate the direction of transitions ([19] - [21]).

Resonant neutralization (RN) involves transfer of an electron in the target valence band to an unoccupied state of the incident ion. This process is possible, as soon as the initially unoccupied final state becomes energetically degenerate with the electrons in the valence band. The most probable capture is in Rydberg states with large spatial extensions and hence a big overlap.

Resonant ionization (RI) is the inverse process to RN and can only occur if the binding energy of occupied excited projectile state becomes smaller than the target work function W_Φ and if empty levels in the valence band are available.

A third possible (near) resonant transition is the quasi-resonant neutralization (QRN) from tightly bound target states to projectile states. Close collisions are necessary for a sufficient overlap of the involved inner electronic orbitals.

The following processes describe two-electron transitions, which are characterized by very short time scales of 10^{-13} - 10^{-16} s.

Auger neutralization

Auger neutralization (AN, Fig. 4) results in ejection of an electron from the target valence band and requires an unoccupied projectile state with a binding energy of at least twice the work function W_Φ.
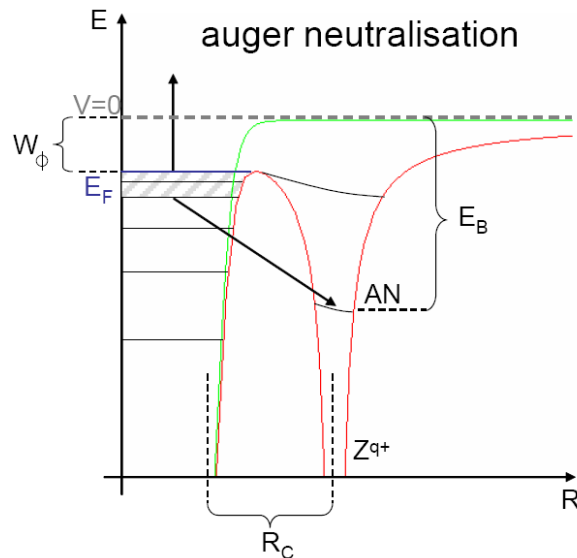

Figure 4: Schematic drawing of Auger neutralization ([19] - [21]).

Two metal electrons are involved, one neutralizing the projectile, the other being ejected with a kinetic energy of

$$E_e \leq W_i^* - 2W_\Phi \tag{2.3}$$

by gaining sufficient energy via electron-electron interaction. W_i^*, the neutralization energy, decreases considerably as AN processes take place closer to the surface and the projectile levels are shifted upward due to interaction with the image charge.

Auger deexcitation

In the case of Auger deexcitation (AD, Fig. 5), an excited projectile electron is deexcited to a lower state and the resulting energy gain transfered to a metal electron which can escape. This process occurs when the binding energy of the projectile electron is larger than the surface work function. The kinetic energy of the ejected electron follows

$$E_e \leq W_{ex} - W_\Phi, \tag{2.4}$$

with W_{ex}, the excitation energy, remaining nearly independent of the distance between particle and surface. This is due to the similarity in initial and final charge states and the comparable level shifts as a consequence thereof.
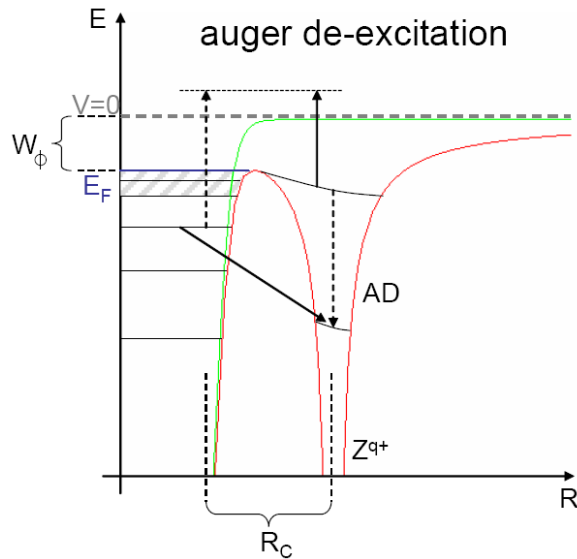

Figure 5: Schematic drawing of Auger deexcitation ([19] - [21]).

Auto-ionization

Auto-ionization (AI, Fig. 6) is the intra-projectile AD and can occur for initially double or multiply excited projectiles, created e.g. via RN processes. One or more electrons are ejected in combination with deexcitation of the excited electrons.
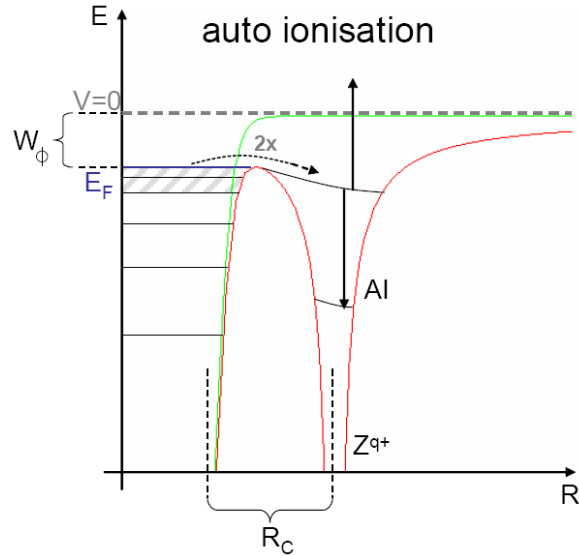

Figure 6: Schematic drawing of auto-ionization ([19] - [21]).

Finally, deexcitation of projectiles can also proceed by means of photon emission. This process is highly improbable for singly charged ions, as the radiative transition rates involved of 10^8 s^{-1} are about 10^6 times smaller than those for the above described processes. For HCI on the other hand, radiative deexcitation can become competitive, since the transition rates increase approximately proportional to the fourth power of the effective ion charge [12].

2.2.2   Hollow atom formation

The large amount of potential energy stored in a HCI is available for inducing several inelastic processes upon impact on the surface. In the course of these processes, the projectile Z^{q+} will recapture its q missing electrons to become again fully neutralized [13]. The deposition of potential energy is completed in a short time ($\sim$ 100 fs) within a small volume ($\sim$ a few nm^3). Through the neutralization sequence of the HCI at the surface, a multiply excited neutral particle is formed, which has been termed "hollow atom" ([12], [22] - [24]), referring to the empty inner shells.
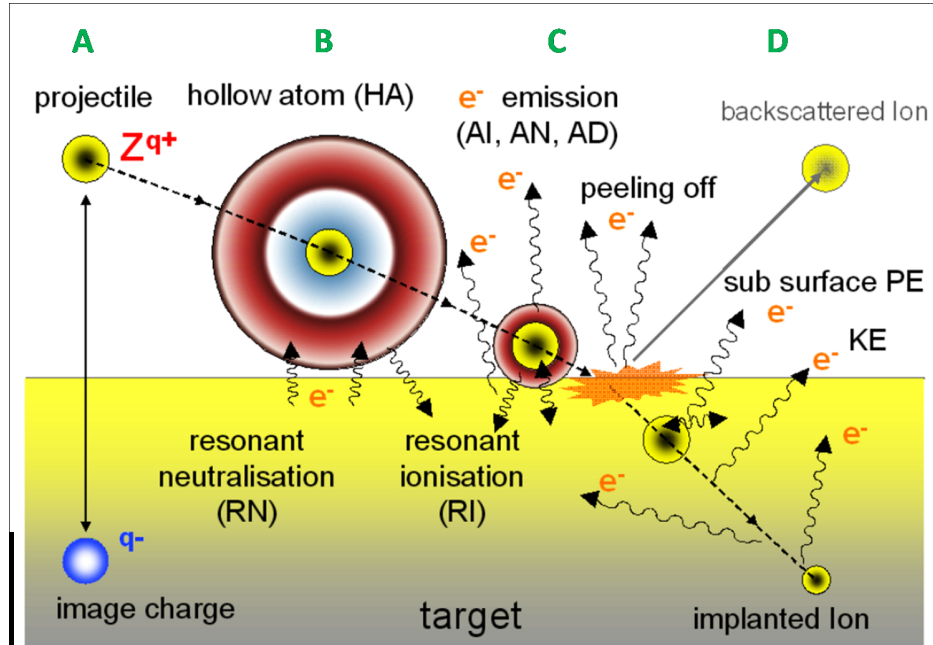
Figure 7: Schematic drawing of the interaction scenario as a HCI appoaches a solid surface [21].

The complete scenario of ion-surface interaction can be divided into 4 stages (Fig. 7): Approach of the projectile toward the surface (A), close contact with the surface (B, C) and penetration into the surface (D) or backscattering into the vacuum. The first two stages are well described within the classical-over-the-barrier model (COB model, [25] - [27]), which will be described in more detail in the following section. In short, the HCI gains kinetic energy via image charge interaction as it approaches the surface and the formation of a primary hollow atom through RN processes begins. Although the HA is subject to auto-ionization, it will be kept dynamically neutral by ongoing RN. Screening by the metal electron gas sets in as close contact is reached (stage C), leading to the "peel off" of remaining outer shell electrons. In the final stage, deexcitation of the so

formed secondary hollow atom will proceed as all remaining inner shell vacancies are filled, resulting in the emission of fast Auger electrons and/or soft X-rays.

All processes involved in the formation and decay of the HA can neither be precisely distinguished nor separated in time. However, slow electron emission yields as well as spectra of fast Auger electrons and soft X-rays can give information on the HA configuration at different stages.

2.2.3   Classical-over-the-barrier model

As stated above, the electron ejection as a result of neutralization of an impinging ion has two main contributions: One from the region below the surface and another from the above-surface portion of the trajectory. The neutralization dynamics of the latter process can be described within the COB model [25], which was originally developed for one-electron capture in HCI-atom collisions.
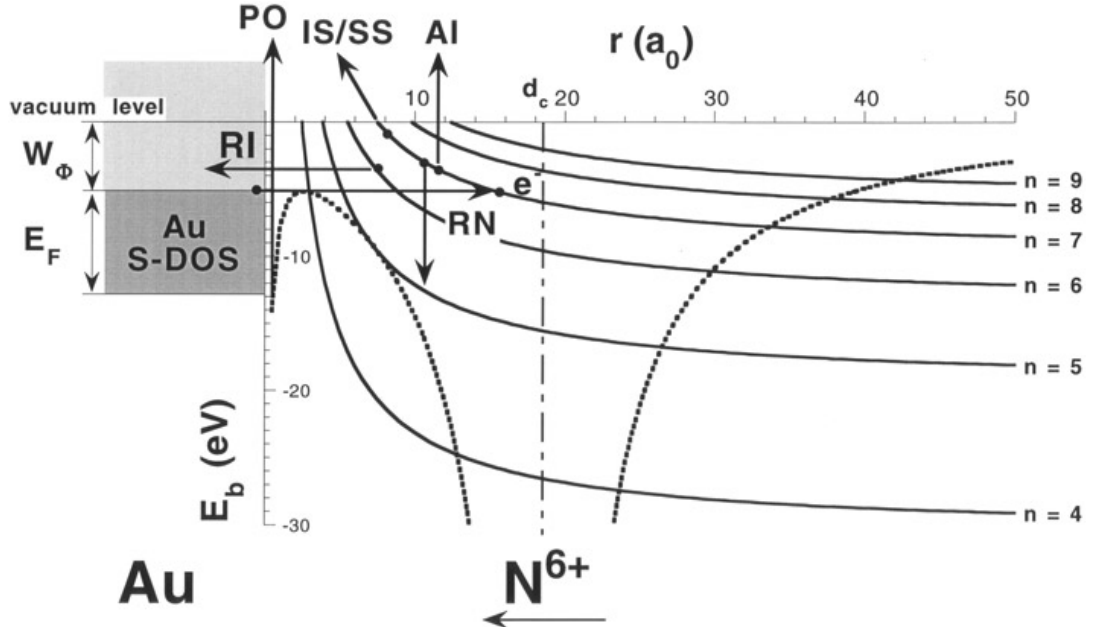

Figure 8: At a critical distance ($\sim$ 18 a.u.), the potential barrier between the target surface (Au) and the HCI (N^{6+}) falls below the Fermi level of Au and resonant electronic transitions become classicaly allowed [13].

The approach of a slow HCI of charge state q and velocity $v \ll v_f$, v_f being the Fermi velocity of the metal target electrons, induces a collective response of the metal electrons which, at sufficiently large distances, can be described by the classical image potential. The HCI is accelerated by this potential toward the surface and the interaction sets a lower limit to the projectile impact velocity which, in turn, limits the time available for

ion-surface interaction upon impact. A second consequence of image interaction is the shifting of weakly bound projectile states which results in a decrease of the potential barrier between the impinging ion and the metal surface (Fig. 8). Electronic transitions become possible as soon as the potential barrier height falls below the fermi level at a critical distance d_q between the projectile and the surface which can be approximated by [25]

$$d_q \simeq \frac{\sqrt{2q}}{W_\Phi} \text{ (atomic units).} \tag{2.5}$$

From this point ("classical lower limit"), electrons near the Fermi edge of the metal surface may be transferred into the incident ion, whereas resonant transitions into highly excited projectile states are the most probable process.

Projectile levels are continuously shifted upwards as a consequence of image interaction (IS) and screening of the projectile charge by captured electrons (SS) in the further approach and lower shells of the projectile become available for population, via e.g. AI processes. At the same time, previously populated higher levels are subject to RI and AI processes. This interplay of electronic transitions will continue throughout the approach and gradually shift the population towards lower n-shells. The population and subsequent deexcitation of the projectile states happens within just a few femtoseconds, pointing to the non-stationary character of the involved states.

Slow electrons emitted in the course of the approach will be instantly replaced by RN and the projectile stays dynamically neutral above the surface. Image charge acceleration continues until neutralization is completed. The corresponding kinetic energy gain of the projectile is closely related to the critical distance for electron capture and (assuming a stepwise neutralization) results in [25]

$$\Delta E_{q,im} = \frac{1}{3\sqrt{2}} \cdot W_\Phi \cdot q^{\frac{3}{2}}. \tag{2.6}$$

Measurements of this energy gain have been found to be in good agreement with the predictions ([28], [29]) and thus give a satisfactory verification of the COB model.

2.2.4   Potential sputtering

In kinetic sputtering, the kinetic energy and momentum transfer between incident ions and target atoms due to collisions can lead to the ejection of target atoms into a vacuum [30]. Direct collisions with the target atoms are the main energy loss mechanism for singly charged ions of a few keV kinetic energy (nuclear stopping), whereas electronic energy loss (electronic stopping) plays a dominant role for faster and especially swift heavy ions (see also section 2.1.2). In any case, a minimum kinetic energy (at which the maximum energy transfer equals the binding energy of a surface atom) is necessary to induce a sputtering event.

For certain target species, the high amount of potential energy stored in an MCI which is liberated during impact on a solid surface, can lead to a different form of ion-induced sputtering [31], which can also occur well below the threshold for kinetic sputtering. In analogy to kinetic sputtering and referring to the sole responsibility of the potential energy of the incident ions (no impact velocity threshold), this phenomenon has been termed "potential sputtering" [32].

First experimental evidence for the occurrence of potential sputtering was found, as secondary ion yields of Ar^{q+} ($q \leq 5$) bombarded Si and alkali-halide surfaces ([33], [34]) showed a rapid increase with incident ion charge state. In later studies on Xe^{q+} ($q \leq 44$) and Th^{q+} ($q \leq 70$) bombarded SiO_2 surfaces [35], a similar charge state dependence was observed above a "threshold" of q = 25.

Such measurements of secondary ion emission, however, cannot provide conclusive information about the total sputter yield. Determination of total sputter yields ([32], [36] - [41]) of various conducting, alkali-halide and other insulating surfaces for impact of Ar^{q+} ($q \leq 14$) and Xe^{q+} ($q \leq 28$) ions (at kinetic energies below 2 keV) could be performed by means of a quartz crystal microbalance technique developed at the TU Wien [42].

For Au samples, as depicted in Fig. 9, the measured total yields follow the data points from SRIM [43] calculations, an algorithm which only considers kinetic sputtering. Also for semiconducting targets (GaAs and Si), no pronounced charge state dependence was detected. For both conducting and semiconducting samples, the total yields increase with ion impact energy above a certain threshold, pointing to "pure" kinetic sputtering. For the investigated alkali-halide samples (LiF, NaCl) on the other hand, measured yields display a strong increase with increasing charge state down to lowest impact energies (Fig. 10).
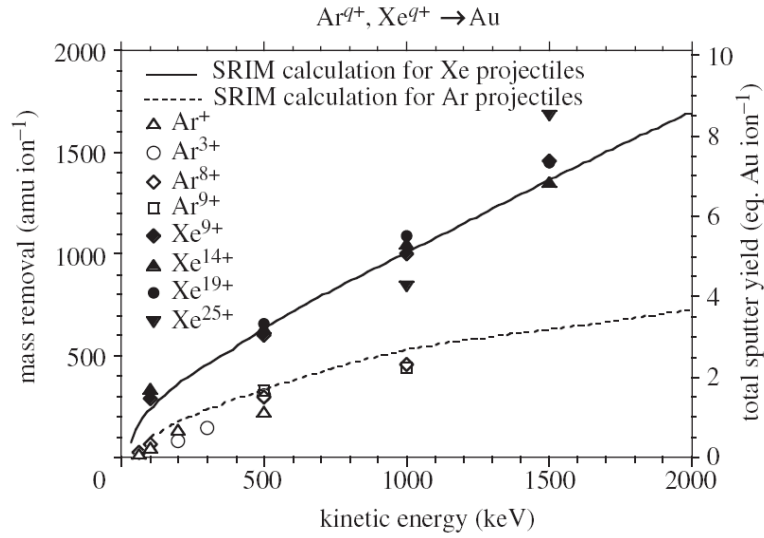
Figure 9: Measured sputter yield of Au for impact of Ar^{q+} and Xe^{q+} ions. Yields for neutral Xe (Ar) atoms from SRIM calculations are shown as a solid (dashed) line [31].
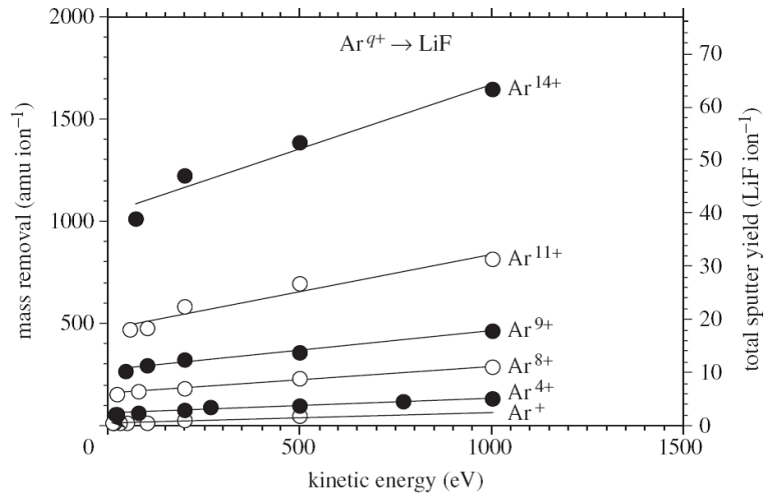

Figure 10: Measured sputter yield of LiF for impact of Ar^{q+} ions as a function of ion impact energy [31].

From experiments with various species of singly and doubly charged ions, the minimum potential energy required to induce potential sputtering from LiF surfaces was found to lie between 9.4 eV (Zn^+) and 10.4 eV (S^+) [39].

For some oxide samples (SiO_2 and Al_2O_3), the measured total yields show a similar behaviour as in the case of alkali-halides, i.e. a strong increase for higher charge states and finite yields when extrapolated to zero impact velocity ([38], [40]). A very different behaviour was found for the sputtering data of thin MgO (actually MgO_x because XPS measurements reveal an oxygen-enriched surface layer) films [41]. Here, the potential energy of the incident ions, although it greatly enhances the total sputtering yield, is not able to induce sputtering events on its own, i.e. some kinetic energy is necessary to achieve sizeable sputter yields (Fig. 11). For all oxide samples, the total yields decrease noticeably with increasing ion doses which can be assigned to preferential sputtering of oxygen [41].
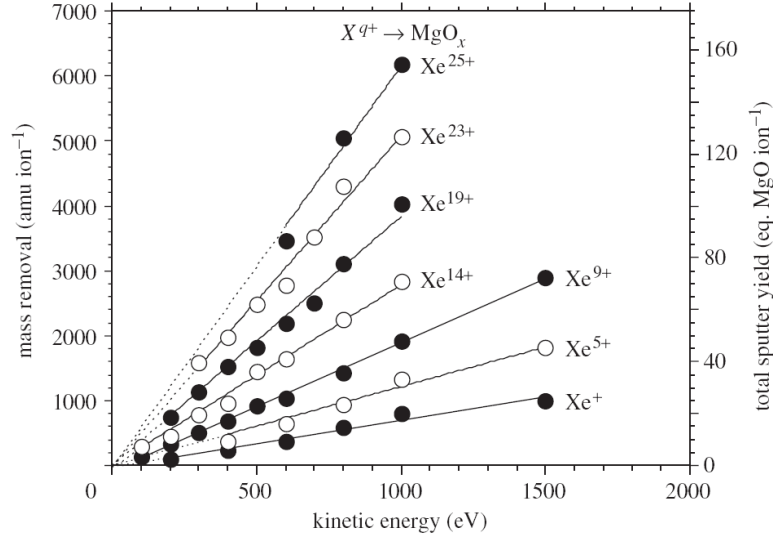

Figure 11: Measured sputter yield of MgO_x films for impact of Xe^{q+} ions [31]. Extrapolation to zero kinetic energy corresponds to zero sputter yield.

As stated in section 2.2.3, the available time for ion-surface interaction is limited by the image charge interaction. For this reason only a fraction of the total potential energy is released above the surface. The ongoing conversion of potential energy in close contact or below the surface into kinetic energy of emitted electrons or electronic excitation will lead to results that are specific for the target material. It can be assumed that for metal surfaces sudden perturbations of the electronic structure can be almost instantly restored. Due to their reduced electron mobility, the same assumption cannot be made for insulating targets and, contrary to the case of metal surfaces, ion-induced structural

modifications (defect formation, sputtering, etc.) are likely to occur.

In the following, a brief description of the theoretical models for the conversion of electronic excitation into kinetic energy of sputtered atoms or ions is given [31]:

Coulomb explosion

In the "Coulomb explosion" (CE, [44]) model, the large number of electrons ejected in the course of the neutralization of an MCI (which can by far exceed the incident ion's charge) leads to the creation of a positively charged volume in the surface-near region. Coulomb repulsion of the target ion cores can eventually lead to CE of this volume, resulting in the emission of secondary ions. Emission of neutral atoms/clusters is caused by shockwaves that are generated by the CE. Experimental evidence for the validity of this model is rare and it is nowadays believed that CE, if possible at all, can only be considered in the case of projectiles with very high charge states.

Sputtering by intense, ultrafast electronic excitation

This model describes the destabilization of atomic bonds in covalent solids from bonding states to antibonding states, resulting in a repulsive force between individual atoms. It was originally developed to describe non-thermal phase transitions in semiconductors induced by intense, ultrafast electronic excitations from femtosecond lasers [45]. The critical laser fluence derived from this model can also be reached for slow, very highly charged ions.

Defect mediated sputtering

In certain insulator materials (alkali-halides, SiO_2) valence band excitations (electron-hole pairs, "hot" holes in the deeper part of the valence band) can become localized. The strong electron-phonon coupling in these materials can result in trapping of excitons and holes in a self-produced lattice deformation [46]. Decay of the so created "self-trapped excitons" (STEs) and "self-trapped holes" (STHs) into colour centres (e.g. H and F centres for alkali-halides) leads to the desorption of neutralized anions (halide atoms, oxygen). An H-centre in LiF is a molecular F_2 ion at an anion lattice site, while a localized electron at the next or second next anion site is an F-centre ([46], Fig. 12). There are two mechanisms for the neutral cations created in this way to be removed from the surface: Either by evaporation (heating of alkalil-halide samples) or by momentum transfer from the incoming ions.
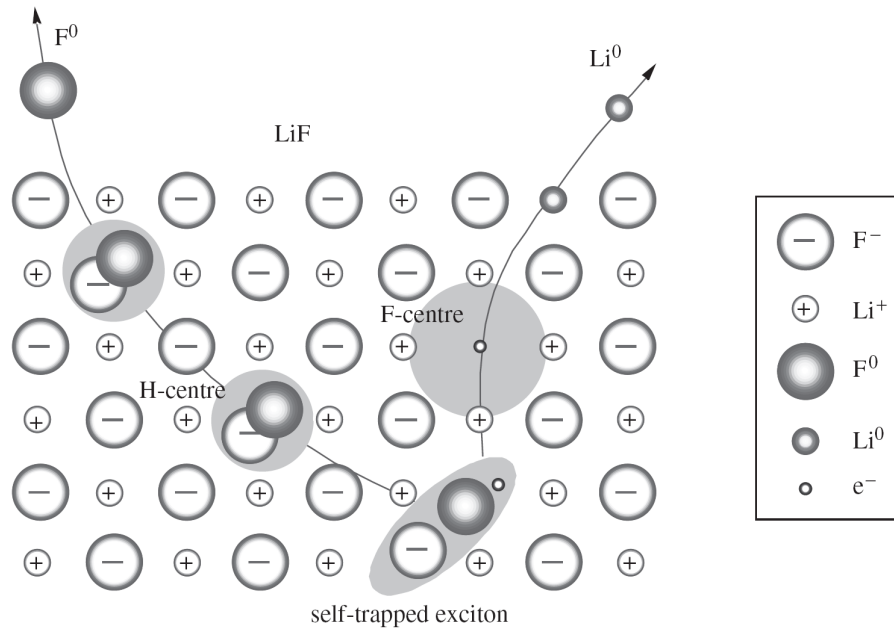
Figure 12: The creation of localized defects and their decay into colour centres induce potential sputtering in LiF, according to the DS model [31].

The experimental findings presented above greatly support the theory of defect mediated sputtering (DS):

1. Measured yields only show a behaviour which can be ascribed to potential sputtering for materials for which strong electron-phonon coupling and the formation of localized defects are known (LiF, NaCl, SiO_2, Al_2O_3), whereas sputtering data of materials without these properties (Au, Si, GaAs) point to kinetically induced sputtering. MgO, although it falls under the latter category of materials, is an exception and will be discussed later.

2. As the number of electronic defects (and consequently the number of STHs and STEs) is expected to be roughly proportional to the potential energy (charge state) of the projectile, the number of sputtered particles should exhibit the same dependence. The measured yields indeed show a nearly linear increase with increasing potential energy (Fig. 10).

3. The observed dose dependence of yields of oxide samples (SiO_2, Al_2O_3) can be explained by the two forms of mass removal proposed in the DS model. Contrary to alkali-halides, ejection of neutralized cations from oxide surfaces is only possible via momentum transfer from the impinging projectile.

At very low impact energies only oxygen is sputtered away, resulting in a Si or Al enriched surface and the observed decrease in potential sputtering with increasing ion dose.

4. Calculations [39] show that the potential energy threshold of ~ 10 eV (between 9.4 eV for Zn^+ ions and 10.4 eV for S^+ ions) for LiF coincides exactly with the energy required for the creation of a "cold hole" (STH) [39]. For doubly charged ions, the creation of at least one additional STH and hence an increase in the sputter yield is expected if the remaining potential energy after the first neutralization step lies above 10 eV. Yields for all doubly charged ions display this behaviour with the exception of Na^{2+}. In this case, although the total potential energy lies above 50 eV, the bigger part of the potential energy is consumed in the first neutralization step. The inability to induce the formation of a second STH with the remaining energy (5.1 eV) explains the exceptionally small sputter yield for Na^{2+}.

Kinetically assisted potential sputtering

The unusual behaviour which was found for the yield of MgO_x neither falls in the "pure" category of potential sputtering nor of kinetic sputtering. As the yields increase considerably with the potential energy of the incident ions, but only in combination with a sufficient amount of kinetic energy, this new form of sputtering was termed "kinetically assisted sputtering" (KAPS, [41]).

According to the DS model, a localization of electronic excitation is essential for effective conversion of electronic energy into kinetic energy of the particles to be desorbed. For materials which do not exhibit self-trapping of electronic excitations, such a localization can only occur at already present defects [47] created by other processes or interfaces. Transient trapping centers for electronic defects may be provided by strong temporary lattice distortions created in the collision cascade of the projectile. This assumption can be expressed in a set of rate equations for the sputtering yield Y which is generally applicable for any insulating target, [31]:

$$\frac{dY}{dt} = c_P N_{ST} + c_{KP} N_{LD} N_{ED} \qquad (2.7)$$

The parameter c_P stands for the conversion rate of a self-trapped electronic defect into desorption of surface particles and c_{KP} for the corresponding conversion rate of a pair of electronic and kinetically induced lattice defects. The parameters N_{ST} (number of self-trapped defects), N_{LD} (number of lattice defects), N_{ED} (number of electronic defects) are defined over analogous rate equations.

The first term in (2.7) equals zero in the case of MgO_x (no self-trapping) and accounts for sputtering at zero kinetic energy for materials with $c_P \neq 0$ (potential sputtering). The

second term (KAPS) describes a linear increase with kinetic energy (SRIM calculations indicate that N_{LD} is proportional to the kinetic energy of the projectile). Since N_{ED} increases with higher charge states, the slope of Y is a steep increasing function of q. Closer inspections of the measured sputter yields show that the KAPS mechanism also contributes for materials with strong electron-phonon coupling and $c_P \neq 0$ (LiF, SiO$_2$, Al$_2$O$_3$). For example, in Fig. 10 the yield also increases linearly with the kinetic energy which cannot be interpreted as conventional kinetic sputtering.

3   Ultrathin Fe films on Cu(100)

Under certain conditions, it is possible to constrain a material to the lattice of a single-crystal substrate and thereby achieve a stabilization of nonequilibrium crystal structures at room temperature and under ambient pressure [48]. Such a stabilization allows for observation of structural and magnetic properties which are unavailable in the bulk materials [49].

A promising model system to study and specifically manipulate magnetic properties of nonequilibrium crystal structures are ultrathin Fe films grown on a Cu(100) single crystal. In this system, as will be shown, a one step transition from a non-ferromagnetic state to a ferromagnetic state can be induced by ion irradiation, making it principally possible to write magnetic dots, lines or other structures [50].

3.1   Structural and magnetic properties

Investigations of the surface magneto-optic Kerr effect (SMOKE, [51]) are a convenient way to obtain hysteresis loops of thin film systems [52] and hence information on the magnetic behaviour of the films. The magneto-optic Kerr effect (MOKE) is the modification of polarization of the reflected light by a material sample subjected to a magnetic field. Three geometries are considered in SMOKE experiments (Fig. 13), corresponding to the three possible forms of the effect:

- Polar magneto-optic Kerr effect:

The magnetic field is oriented perpendicular to the surface and the plane of polarization of the reflected light is rotated.

- Longitudinal magneto-optic Kerr effect:

The magnetic field is oriented parallel to the surface and the plane of incidence. Again the plane of polarization is rotated.

- Transverse magneto-optic Kerr effect:

The magnetic field is oriented parallel to the surface and perpendicular to the plane of incidence. The incident light must be polarized in the plane of incidence. The intensity of the reflected light is modified without a rotation of the plane of polarization.
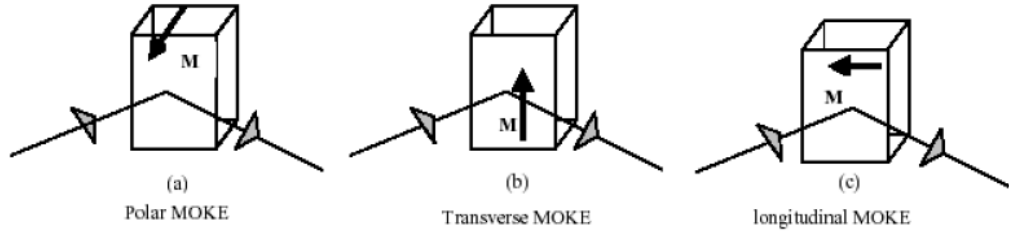
Figure 13: The three different geometrical setups in SMOKE experiments.

Two parameters can be defined to describe the effect of the magnetic field on the reflection of incident light: the Kerr angle ϕ and the ellipticity ε (Fig. 14). Typically, after reflection the originally linear polarized light is elliptically polarized. The major axis of the ellipsis is rotated by an angle ϕ with respect to the principal plane of polarization. The ellipticity depends on the ratio of the half-axes.
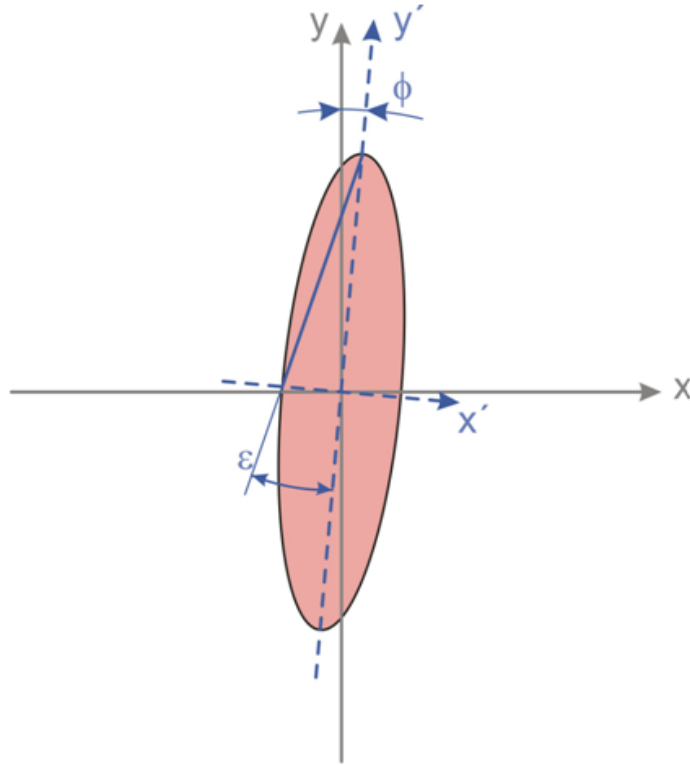
Figure 14: Geometrical representation of the Kerr angle ϕ and the ellipticity ε [58].

A multitude of experimental studies have been carried out to determine both the magnetic properties ([52] - [54]) and the crystallographic structure ([55] - [57]) of ultrathin Fe films grown on Cu(100). The obtained data, unsurprisingly, imply a close correlation between film morphology and the magnetic properties. In the following, the present knowledge on the properties of the films in the respective growth stadiums will be summarized.

Before doing so, it is worthwhile to take a look at the phase diagram of pure Fe, depicted in Fig. 15. Bulk Fe under standard conditions is characterized by a ferromagnetic bcc phase. Whether the paramagnetic fcc phase can be stabilized at room temperature as a result of pseudomorphic growth on the (100)-oriented fcc Cu substrate depends critically on the film thickness.
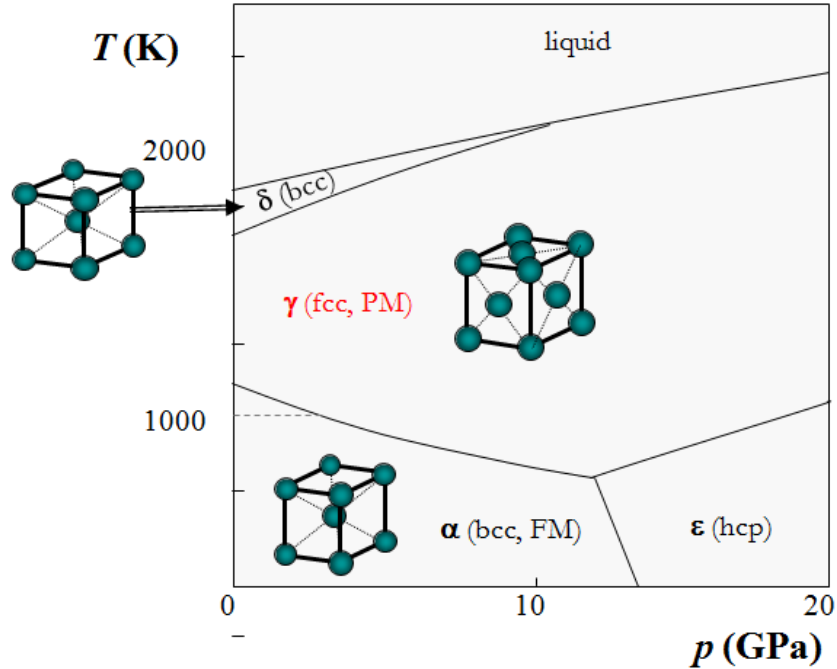
Figure 15: Phase diagram of pure iron [58].

Thickness regime below 2 ML
In the early stages of film growth, intermixing processes are dominant and can be seen as roughening of monoatomic steps and Fe inclusions in the Cu surface. STM images of the surface after a deposition of only 0.2 monolayers (ML) already show Fe clusters with bond angles of $\sim 75°$ which is close to the bcc(110) bond angle of 70.5° . Similar bond angles are also found for larger Fe areas in 1.7 ML films and seem to be characteristic for strained bcc structures in all thickness regimes [57].

Thickness regime of 2 - 4 ML

Fig. 16 shows a steeply increasing ellipticity (measure of magnetization) with increasing film thickness and Curie temperatures greater than 300 K. This increase points to a bulk ferromagnetic phase with perpendicular anisotropy. The existence of this phase, however, is somewhat surprising as one might intuitively rather expect a pseudomorphic fcc structure.
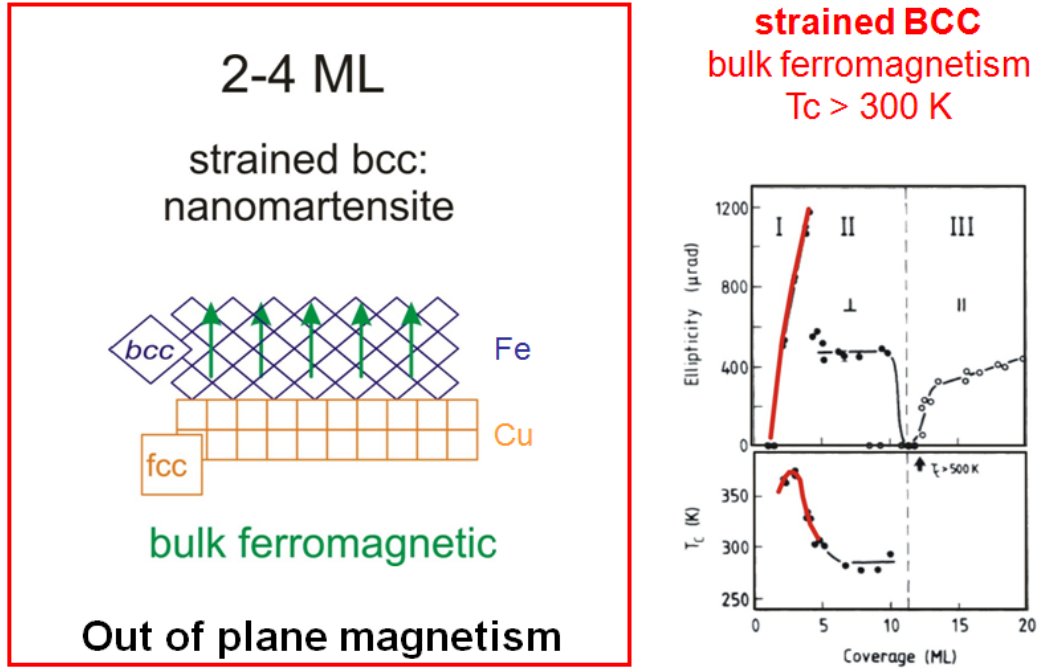

Figure 16: Structural and magnetic properties of 2 - 4 ML Fe on Cu(100) (right, [58]). SMOKE measurements in polar geometry (left, [53]).

Careful STM investigations have shown that the outstanding magnetic properties in this thickness regime can be related to a stable nonpseudomorphic bcc-like phase ([56], [57]). The atomic structure of this phase is characterized by zigzag atomic rows with a spatial wavelength of 5 - 6 atoms, depending on the film thickness. Again these structures can be described as a result of sheering the fcc lattice by 14 - 15°, effectively converting the bonding angle from its fcc value (90°) to $\sim 75°$. This sheering corresponds to an elevation of the atom rows by about a quarter of the interlayer distance and transforms the fcc(100) into a bcc(110) surface (Fig. 17).
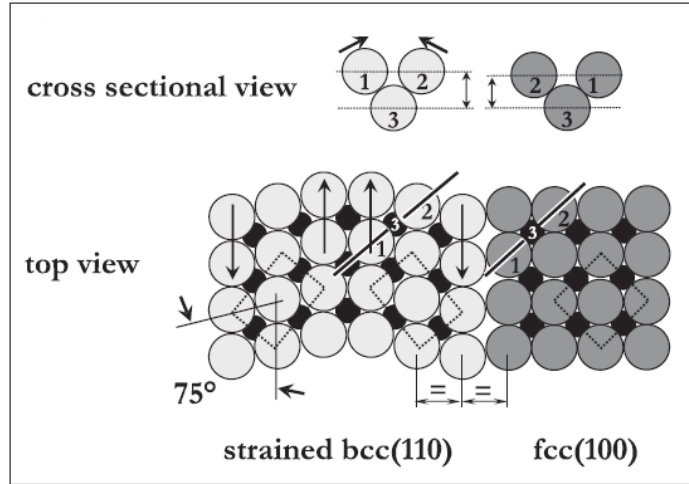
Figure 17: Schematic transformation of the fcc(100) oriented surface into a bcc(100) oriented surface [57].

3 ML thick films show the highest content of bcc-like structures ($> 50\%$) and the widest bcc-like stripes whereas films close to 2 ML and above 4 ML show more narrow bcc-like stripes and a higher fcc content. The obtained magnetization in the respective regimes can be clearly correlated with these structural differences.

As the observed zigzag structures consist of a regular arrangement of 2 - 4 atoms wide bcc twins they have been termed "nanomartensic", in contrast to the irregular twinned arrangements on a larger scale known as the twin variety of Fe martensite [57].

Thickness regime of 5 - 10 ML

Above 4 - 5 ML film thickness the previously described nanomartensic phase disappears and a pseudomorphic growth of Fe in fcc structure sets in. Within this structure, however, a nucleation of bcc iron is observed, referred to as bcc needles (Fig. 18). The local atomic arrangement within these needles is equivalent to the nanomartensic structure but their width (8 - 10 atomic rows) is very different. The overall needle density is quite small at room temperature (1% - 3%) but can considerably increase when cooling the film (10% or even higher at 80K).

Comparing the atomic geometry to the ideal bcc structure reveals a large strain within the observed needles [55]. A tensile strain of $\sim 9\%$ perpendicular to the axis of the needle is necessary to close the gap to the surrounding fcc lattice (Fig. 19).
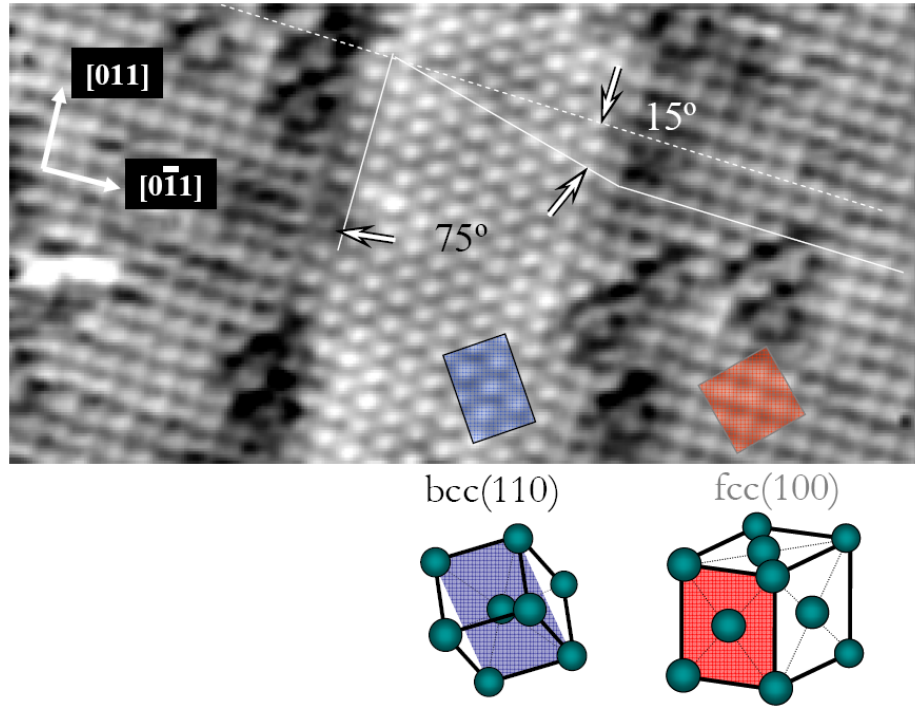
Figure 18: STM image of a bcc needle and surrounding fcc lattice [55].
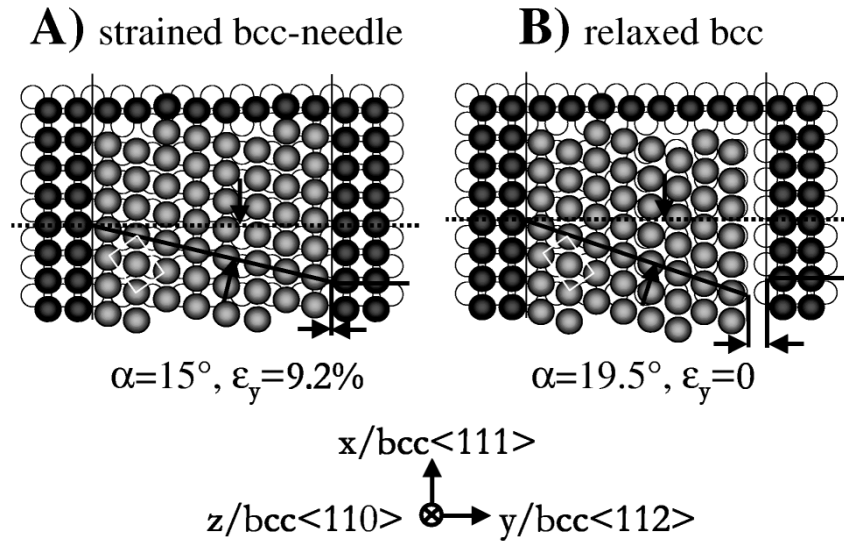

Figure 19: Schematic comparison of a strained bcc needle and a relaxed bcc needle in the surrounding fcc lattice [55].

The Kerr signal, as illustrated in Fig. 20, shows practically no dependence on the film thickness indicating that the bulk of the film does not contribute and that the magnetism should be localized either at the surface or at the Fe-Cu interface. In [53] it was found that the Curie temperature is lowered by 40 K upon CO exposure of 0.5 Langmuir which points to magnetism arising from a ferromagnetically ordered surface layer ("magnetic live layer"). This surface magnetism with a perpendicular orientation of the magnetic moment can be related to an expanded interlayer distance at the surface which results from a (2 x 2)p4g surface reconstruction [57].
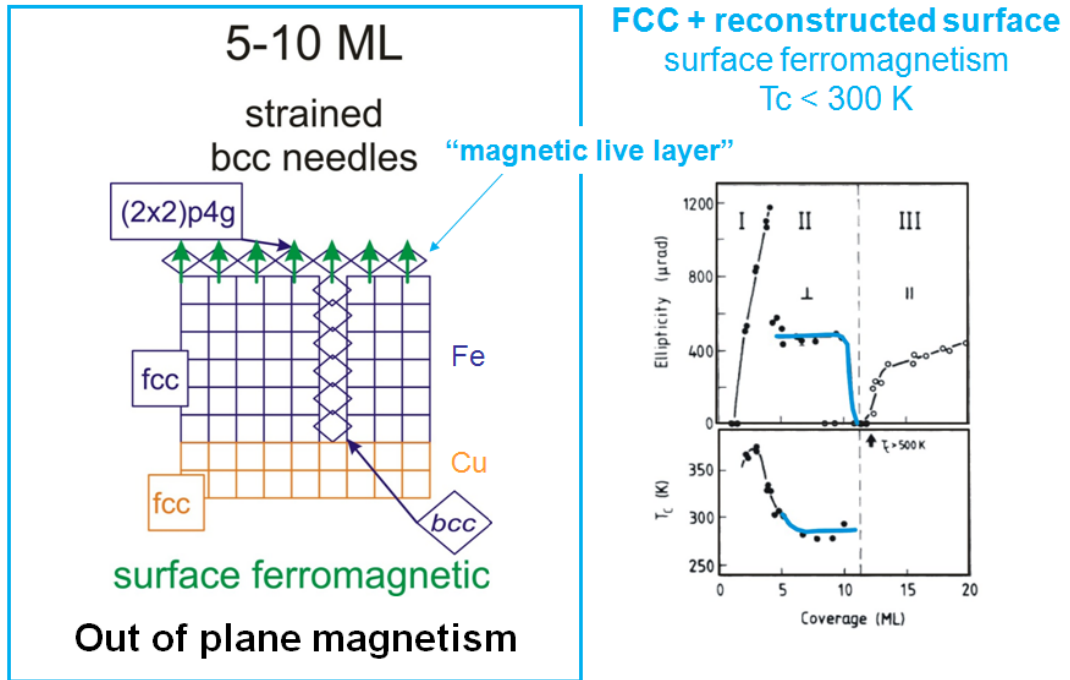
Figure 20: Structural and magnetic properties of 5 - 10 ML Fe on Cu(100) (right, [58]). SMOKE measurements in polar geometry (left, [53]).

Thickness regime > 10 ML
Once the thickness exceeds ∼ 11 ML, the film relaxes to regular bcc structure with bulk in-plane ferromagnetism, i. e. magnetic ordering parallel to the surface and Curie temperatures above 500 K. The setup of the SMOKE measurement must hence be changed to longitudinal geometry. The Kerr signal increases with increasing film thickness but does not reach the values found in the other thickness regimes (Fig. 21).
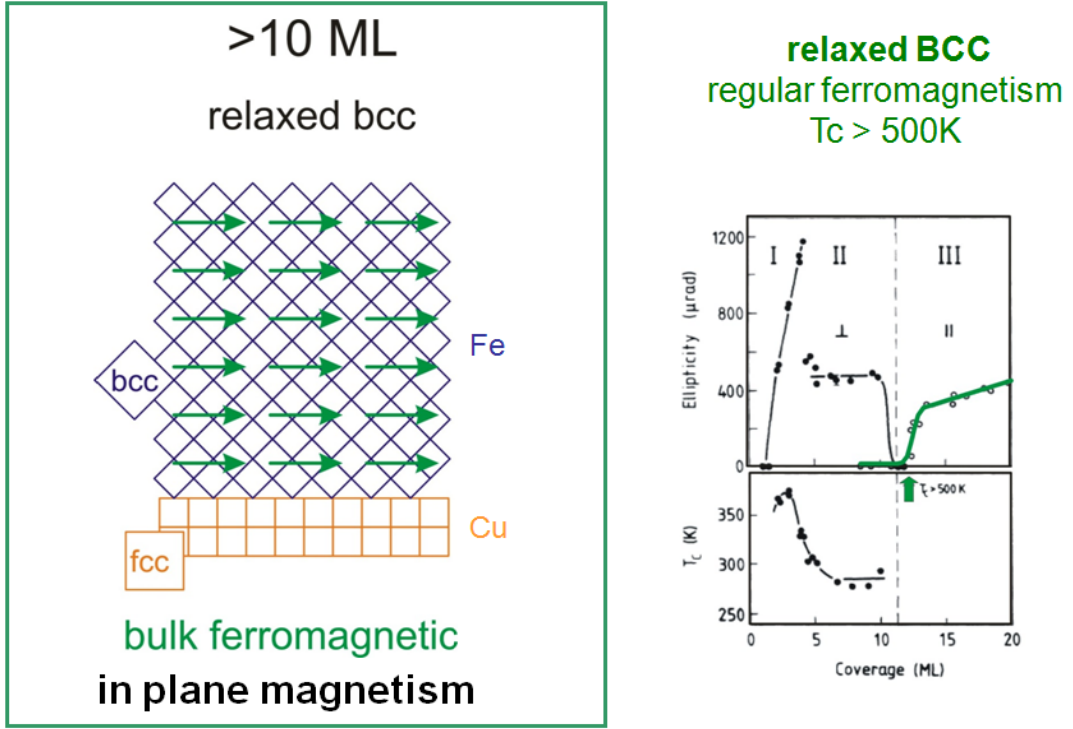
Figure 21: Structural and magnetic properties of > 10 ML Fe on Cu(100) (right, [58]). SMOKE measurements in longitudinal geometry [53].

3.2　Ion-induced phase transition

Ion irradiation of the Fe films in the thickness regime between 5 and 10 ML results in a transformation of the fcc structure to strained bcc structure with in-plane ferromagnetism at room temperature. This transformation can be experimentally observed with both STM and SMOKE investigation of the film surfaces.

From the STM images it can be inferred that the bcc needles which exist in low density also in the non-treated films quickly grow in length with increasing ion doses, but slowly in width. After exposure to fairly high ion doses, the STM images show a rough surface where the fcc and bcc areas are hard to distinguish. The expansion of the bcc areas in the film can also be monitored by means of low energy electron diffraction (LEED), where the bcc structure leads to elongated spots (Fig. 22).

Smoke measurements reveal a paramagnetic behaviour of the non-treated films at room temperature with no hysteresis. After a small dose corresponding to 0.02 ions/surface atoms a hysteresis loop starts to develop indicating the beginning transformation from a paramagnetic to a ferromagnetic state with an in-plane easy axis (Fig. 23).
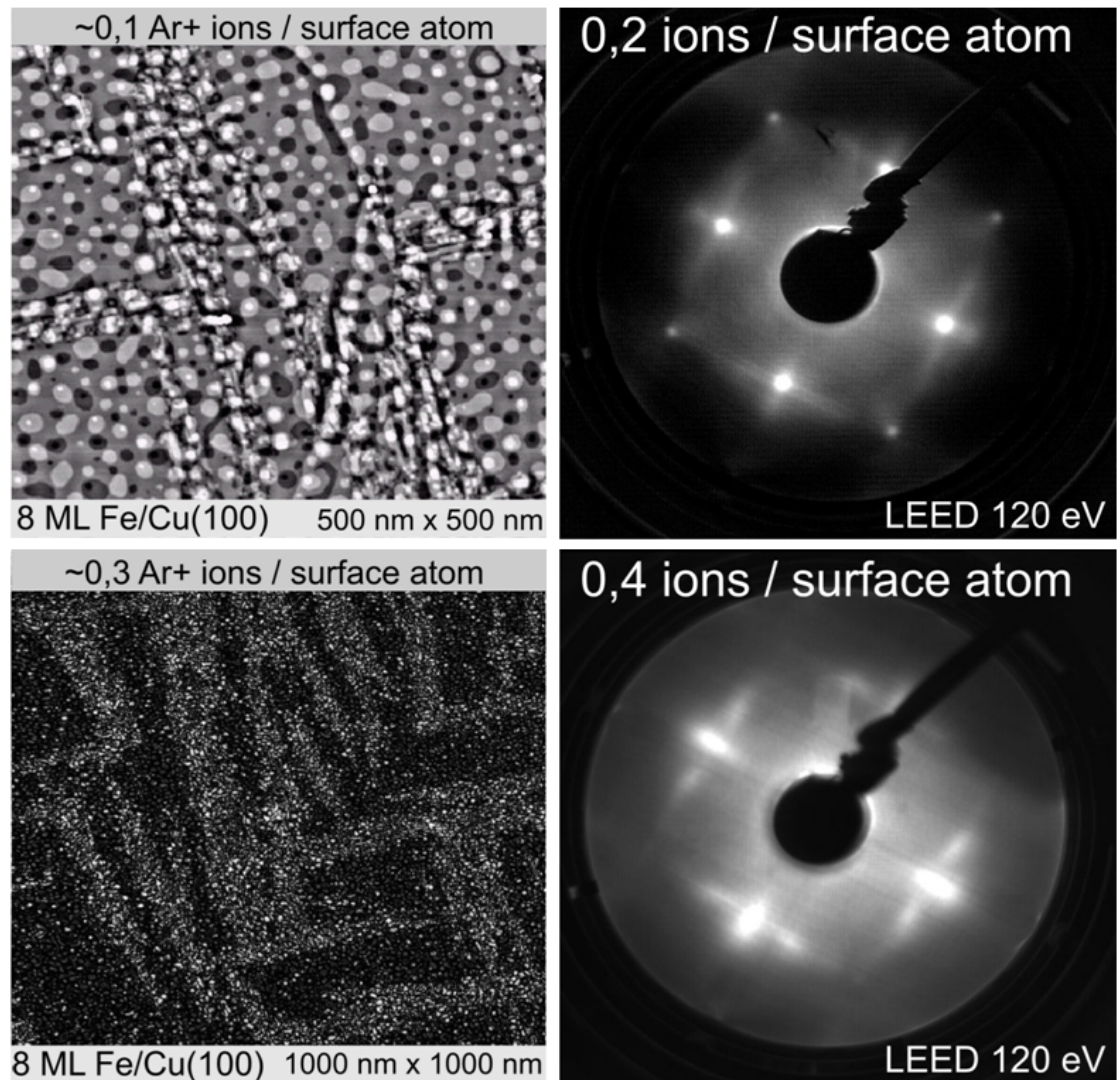
Figure 22: Expansion of bcc needles in an 8 ML Fe film grown on Cu(100) as a result of 1 keV Ar^+ ion bombardment as seen with the STM (left) and with LEED (right) for increasing ion doses from top left to bottom right [50]. Note the different scansizes in the top left and the bottom left STM image.
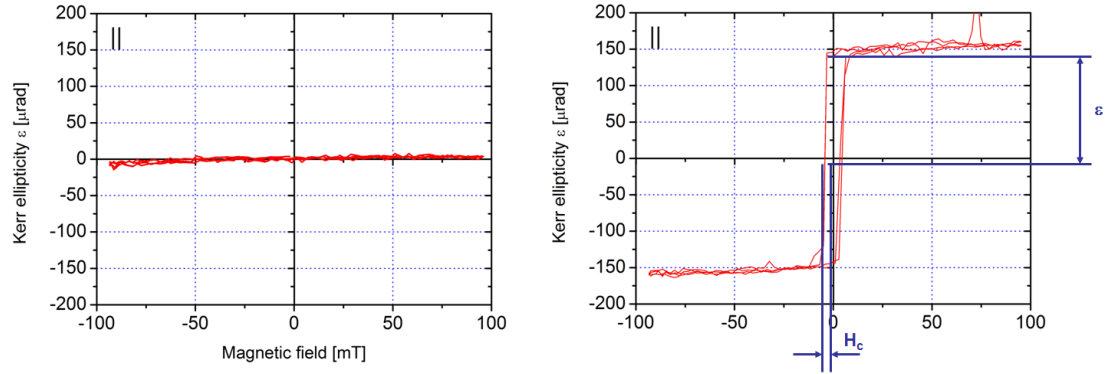
Figure 23: Kerr signal in longitudinal geometry from an 8 ML Fe film on Cu(100) as grown (left) and after irradiation with 1 keV Ar^+ ions (0.6 ions/surface atom, right). From the hysteresis loop the remanence ε and the coercive field H_c can be obtained [58].

Fig. 24 shows that the speed of the transformation and the attainable saturation magnetization depend heavily on the energy of the impinging Ar^+ ions. The fastest transformation is achieved with 1 keV ions. Transformation proceeds slower with 2 keV ions, but the same magnetization is reached. For even higher Ar^+ ion energies, transformation is further slowed down without achieving the magnetization values of the lower energy ions.
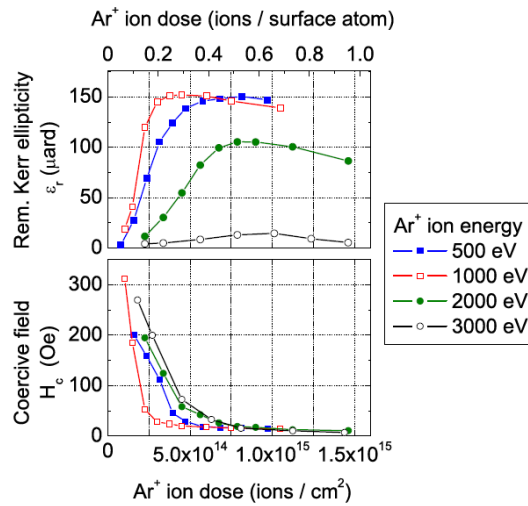
Figure 24: Ar^+ fluence dependence of the remanent Kerr ellipticity (top) and the coercive field (bottom) of 8 ML Fe grown on Cu(100) for different ion energies [50].

This behaviour can be qualitatively described as a consequence of local melting and recrystallization. The number of Cu atoms in the melt, which is formed due to the high kinetic energies of the target atoms after ion impact, depends strongly on the energy of the incoming ions. Calculations show that the Cu fraction in the melt considerably increases with increasing ion energies which subsequently impedes the fcc to bcc transformation of iron [50].

4 Experimental methods

4.1 Ion sources for highly charged ions

4.1.1 Electron beam ion trap

Working principle

In an electron beam ion trap (EBIT), a dense electron beam, focused by the strong magnetic field of a superconducting Helmholtz pair, forms a radial well for ions by its space charge, which is closed axially by potentials applied to cylindrical electrodes (drift tubes) surrounding the beam [59] (Fig. 25).
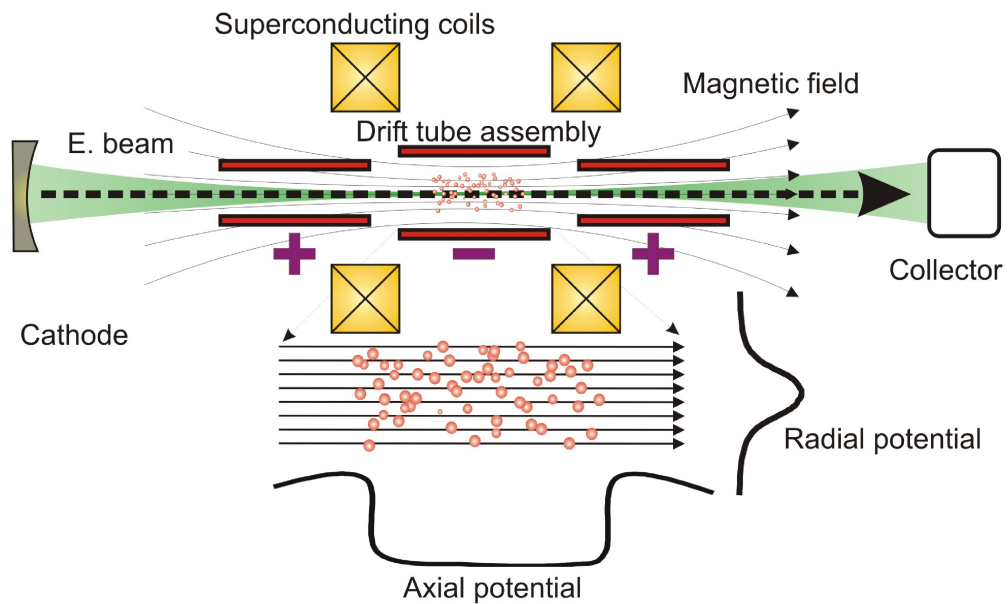
Figure 25: Schematic of the typical EBIT setup: The elecron beam is accelerated towards the drift tube assembly and decelerated upon arrival at the collector to minimize heat deposition and x-ray production. Ionized atoms are trapped and undergo further ionization steps within the trap volume [60].

Inside the electron beam, atoms are ionized and trapped to undergo further stepwise ionization. This process will continue until either the stripping limit of the electron energy is reached or the ions are axially extracted by a change of the drift tube potentials. The EBIT is actually a derivative of the earlier developed electron beam ion source (EBIS) and is based on its working principle. The biggest difference between the two devices is that the EBIT trap length is much shorter than in an EBIS (roughly 1:25). But it has been shown that the transition between EBIS and EBIT modes is continuous and a distinction as different devices therefore arbitrary [59].

The Rossendorf two-source facility

The two-source facility [61] at Forschungszentrum Dresden-Rossendorf was constructed in 2004 and employs a combination of two powerful ion sources (Fig. 26). An electron cyclotron resonance ion source (ECRIS) provides high currents of low to medium charged ions and an EBIT (more exact a Dresden EBIT, see next paragraph) provides lower currents of very highly charged ions. Ion irradiation experiments on CaF_2, described in chapter 6, were performed with ions extracted from this EBIT.
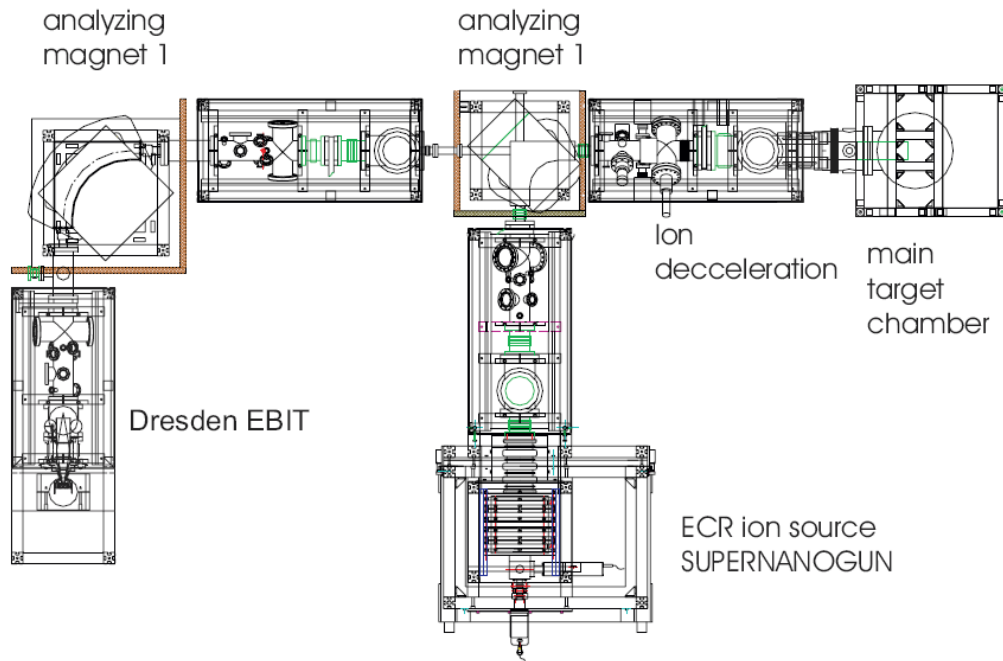
Figure 26: Setup of the two-source facility at Forschungszentrum Dresden-Rossendorf: The device allows to run experiments simultaneously with ion beams extracted from both ion sources or separately [61].

Characteristics of the Dresden EBIT

The Dresden EBIT (DEBIT, [62] - [67]) differs substantially from EBITs in the typical setup (Fig. 25) in one aspect: The superconducting Helmholtz coils are substituted for two $SmCo_5$ permanent magnets (magnetic field ~ 0.25 T). The apparatus can thus work at room temperature without any cryogenic system, making it a low-expense, compact alternative to other devices. Naturally, the electron density in a room temperature EBIT is much smaller than in a cryogenic EBIT corresponding to the differences of the focusing magnetic fields (0.25 T $\leftrightarrow$ some T).
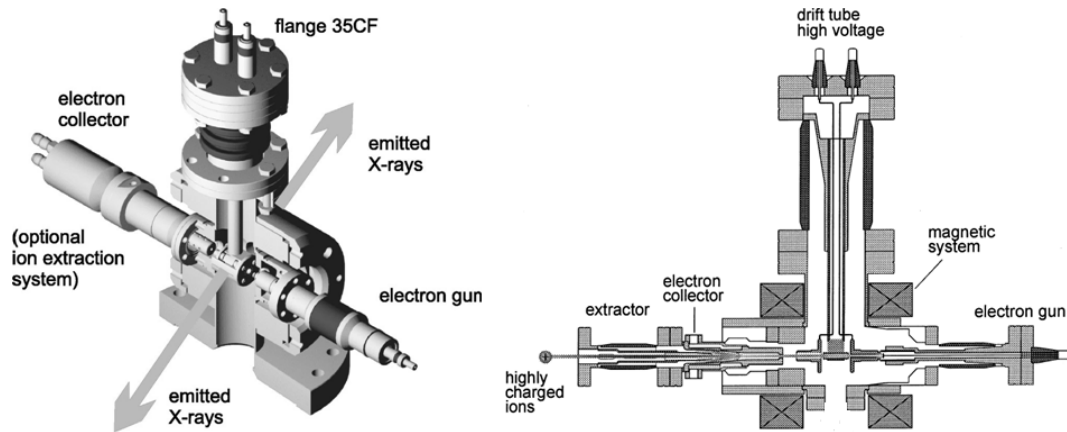
Figure 27: 3D-representation (left, [66]) and sketch of the DEBIT (right, [64]).

Nevertheless, it has been shown that the DEBIT is able to produce bare nuclei for elements up to about $Z = 30$ and helium-like to neon-like ions for heavier elements, respectively.

Extraction, charge state separation and deceleration

The two-source facility is based on an acceleration-deceleration principle. As the target is grounded and the ion sources are on the voltage ΔU, the beam guiding system is set to a negative potential. The quantity $q \times \Delta U$ mainly determines the final kinetic energy of the ion species with charge state q.
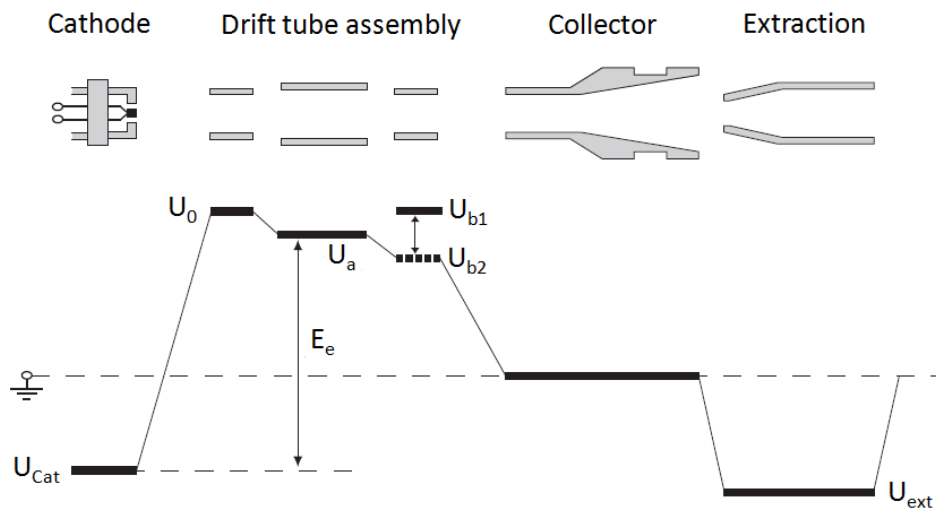
Figure 28: Axial potential distribution and extraction. Image modified from [68].

Fig. 28 depicts the axial confinement of ions in the DEBIT realized by a threepart drift tube assembly. For the irradiation experiments ions were extracted in the pulsed mode. Here the potential barrier is periodically lowered to allow the ions to axially escape the trap whereas in leaky mode the potential applied to the third drift tube (U_b) is fixed in a way that ions with sufficient kinetic energy can escape continuously.

After acceleration by means of an extraction electrode (U_{ext}), the ions are guided by ion-optical elements to an analyzing magnet which separates the ion charge states according to their charge to mass ratio (Fig. 26). Ions of the desired charge state finally pass a deceleration lens upon impact on the target. The potentials of this lens can be chosen to reduce the kinetic energy to values as low as q x 5 eV (Fig. 29).
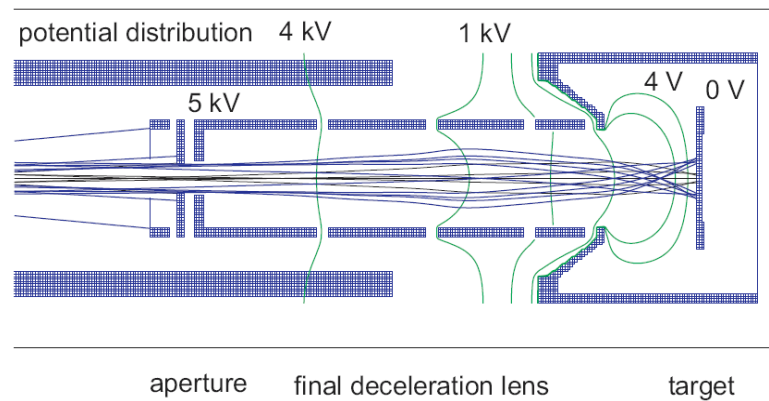
Figure 29: Beam propagation through the final deceleration lens [61].

The possibility to reduce the kinetic energies of the projectiles to such low values in order to study potential energy effects is a crucial advantage over e.g. the extraction system of the Heidelberg EBIT where the final impact energies are determined by the effective ion extraction potential and can thus not be chosen in such a wide range.

4.1.2   Electron cyclotron resonance ion source

Working principle

The basic idea of an electron cyclotron resonance ion source (ECRIS) is microwave electron cyclotron resonance heating of the electrons in a plasma and magnetic confinement of the ions created therein [59].
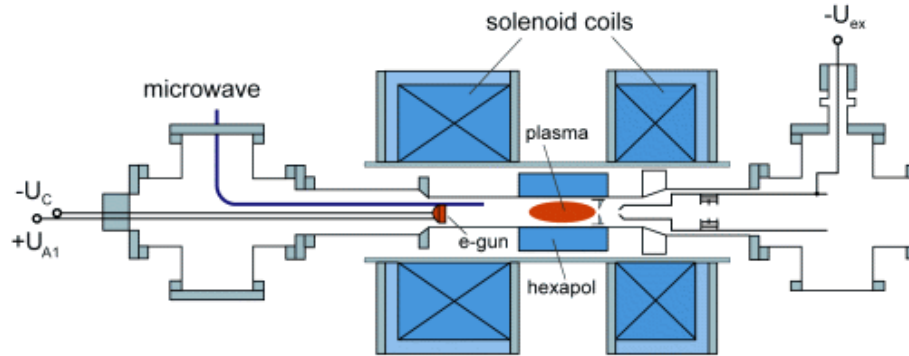

Figure 30: Schematic setup of an ECRIS [69].

To confine the plasma a special magnetic field configuration is necessary. This is achieved by the superposition of the radial magnetic field of a (typically) permanent magnetic multipole (most often hexapoles) and an axial magnetic mirror field (e.g. produced by a pair of solenoid coils, Fig. 30). This geometry results in a minimum-B-structure, i.e. an increase of the magnetic field in all directions from the geometrical middle. The confined plasma electrons gyrate around the magnetic field lines with the cyclotron frequency

$$\omega_c = \frac{e}{m} \cdot B. \tag{4.1}$$

Injected microwaves can resonantly heat the electrons if the respective frequencies are equal. For an ECRIS employing a 14.5 GHz microwave, equation (4.1) gives a corresponding resonant magnetic field of 0.52 T.

Passing the resonance region, an electron can gain 1 - 2 keV energy for further impact ionization processes. Ions, due to their heavy mass, are not accelerated and are confined by the space charge of the electrons.

When electrons leave the plasma through the loss cone of the magnetic mirror, following ions can be extracted and subsequently separated with an analyzing magnet.

The ARIBE facility

The ARIBE (Accélérateurs de Recherche Interdisciplinaire avec des Ions de Basse energie - Accelerators for interdisciplinary research with low-energy ions, [70]) facility, located at GANIL (Grand Accélérateur National d'Ions Lourds, Caen), employs a variety of ion sources and beam lines for different experimental demands.

Irradiation experiments on HOPG and mica (see chapter 6) were performed on one of the high intensity beam lines [71] at ARIBE. A total of seven beamlines can be supplied with highly charged ions from an 14.5 GHz ECRIS (SUPERSHYPIE, a derivative of the earlier developed ECR4M ion source) at kinetic energies between 3 and 25 keV per charge (Fig. 31).
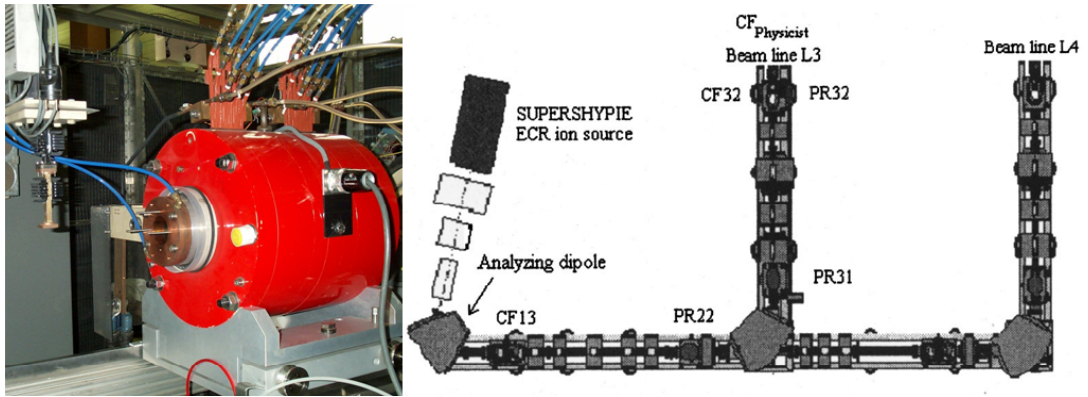
Figure 31: Photography of the SUPERSHYPHIE source (left) and schematic setup of beam lines (right, presently 5 additional beam lines are in use on the right-hand side). Experiments were performed on beam line L3 [71].

The axial magnetic field of the SUPERSHYPIE ion source results from a combination of two main coils and permanent magnet rings. The main contribution to the axial field comes from the coils whereas the magnet rings enhance the maxima B (Fig. 32).

The source is mounted on a high voltage platform able to provide a beam with an energy range between 3 and 25 q kV.
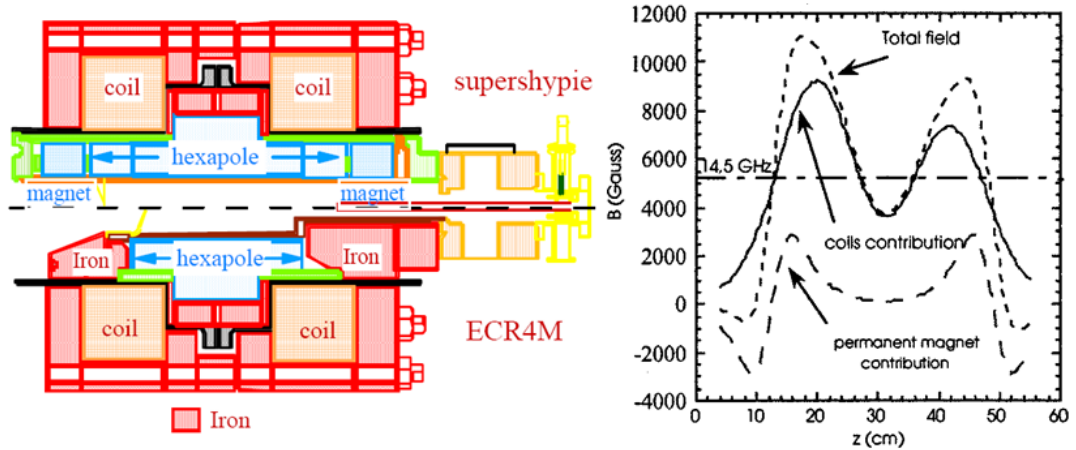
Figure 32: Schematics of the ECR4M and its successor SUPERSHYPIE (left): Iron pieces have been replaced by permanent magnet rings. Axial field distribution in the source (right): Crossings with the microwave frequency appear at B = 5200 Gauss and represent the resonance regions [71].

The beam lines are dedicated to transport high current intensities with very high emittance at a typical pressure of 10^{-9} mbar. The resulting irradiation times to achieve fluences of about 10^{11} ions/cm^2 are in the order of minutes for medium Xe charge states (q = 23, 27) while hours are needed for comparable fluences in case of the DEBIT. The DEBIT, however, can deliver considerably higher maximum charge states.

4.2   Scanning probe microscopies

Since the invention of the scanning tunneling microscope (STM) in 1981, the first scanning probe microscope (SPM), a multitude of devices has been introduced and there is still no end in sight. Although these devices may seem very different and unrelated at a first glance, they all share the same general concept:

A sharp probe is raster-scanned across a sample by means of piezoelectronic translators, while a certain signal (current, force, torsion, electromagnetic radiation, etc.) is recorded by the probe for every single image point [72]. The most important aspect of this concept is to use this local signal for monitoring the probe-sample separation and hence obtain topographical information in real space. In order to accomplish this task, one can identify the following components as common features of SPMs [72]:

- Sharp probe.

- Piezoelectric translator to move the probe relative to the sample.

- Detection system for the signal delivered by the probe.

- Feedback system to keep the signal constant by height readjustment of the probe.

- Imaging system to convert the single data points to an image.

The two, perhaps most powerful SPMs which are preferentially used in surface science today and have been used in the experiments presented in this work shall be described in the following.

4.2.1   Scanning tunneling microscopy

The scanning tunneling microscope (STM) probes the current between a sharp metal tip and a conductive sample [73]. A bias voltage applied between tip and sample allows electrons to "quantum tunnel" through the vacuum between them. Since there is an exponential relation between the tunneling current and the tip-surface separation, the tunneling current is an extremely sensitive measure to control that separation [72]. A change in the separation of only 0.1 nm will change the tunneling current by a factor of 5 - 10. This means that in principle a vertical resolution of 1 pm can be reached if the current is kept constant within a few percent. On closer examination, however, a variety of parameters must be taken into account: The density of states in the sample and tip and their interaction at small distances, different Fermi levels of tip and sample, etc.
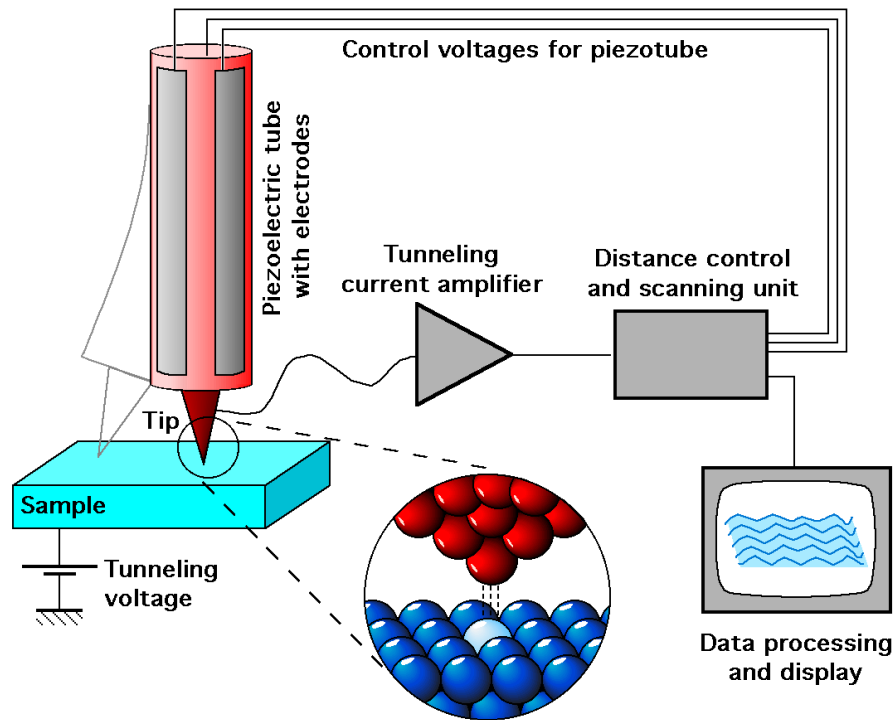
Figure 33: Operating principle of an STM [74].

The most common mode of operation is the constant current mode. A control loop adjusts the tip-sample separation in a way that the tunneling current remains constant while scanning across the surface and the z-piezo voltage (height) is simultaneously recorded. The tip follows contours of the local density of states near the Fermi level. The microscope thus doesn't actually image the surface topography but rather the electronic structure. Typical tunneling currents are in a range of 0.1 - 10 nA, voltages applied are typically 1 mV to some V at tip-sample separations of 0.5 - 1.5 nm.

4.2.2 Atomic force microscopy

The basic idea of atomic force microscopy (AFM) is the measurement and interpretation of the ultrasmall forces (< 1 nN), that occur between the AFM tip and the sample surface at very small distances or in contact [75]. To do so, a laser beam is aligned with a cantilever, on which the AFM tip is mounted, and changes in the cantilever position are detected by a deflection sensor, commonly a four-quadrant photodiode (Fig. 34). Devices not using a laser beam can measure the deflection with tunnelling or capacitive detectors.

There are two basic modes of operation in AFM, the static mode and the dynamic mode.
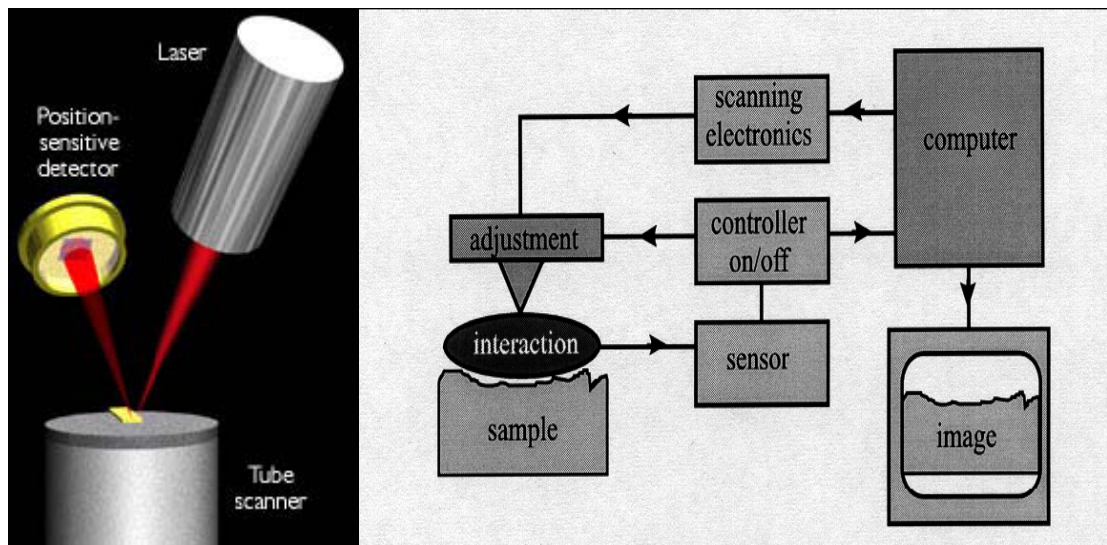
Figure 34: Basic setup of an atomic force microscope [76].

Static AFM

In contact mode the tip scans the sample in close contact with the surface or the sample is moved and the tip rests immobile. The force on the tip-atoms is caused by electronic orbital overlap with the surface atoms. It is repulsive with a mean value of 10^{-9} N. The cantilever is pushed against the sample surface with a piezoelectric positioning element. During the scanning process, the deflection of the cantilever is permanently sensed and compared in a DC feedback amplifier to a preset value of deflection (setpoint). The higher the chosen value of the setpoint, the stronger the tip pushes into the surface. Therefore one practically starts with small deflections and increases the setpoint slowly. If the measured deflection is different from the desired value, the feedback amplifier applies a voltage to the piezo to raise or lower the sample relative to the cantilever in order to restore the preset value of deflection. The voltage applied to the piezo is directly

correlated to the piezo movement and therefore to the height of features on the sample surface. It is displayed as a function of the lateral position of the sample.

Excessive imaging forces applied by the probe to the sample cause the most distinct problems in contact mode AFM. The effects can be reduced by minimizing imaging force of the probe on the sample, but there are practical limits to the magnitude of the force that can be controlled in ambient environment: Under ambient conditions, sample surfaces are covered by a water layer. When the probe makes contact with this layer, a meniscus forms and the cantilever is pulled toward the sample surface by surface tension. This meniscus force and other attractive forces may be minimized or even neutralized by operating with the probe and the sample totally immersed in liquid. There are many advantages to operate AFM with the sample and cantilever immersed in a fluid. These advantages include the elimination of capillary forces, the reduction of van der Waals forces and the ability to study technologically or biologically important processes at the liquid-solid-interface [72].

Dynamic AFM

Another possible way of operating the microscope is in non-contact mode. This can be very useful in situations where tip contact may change the surface properties in different ways. The tip hovers 5 - 15 nm above the sample surface and attractive van der Waals forces between the tip and the sample are detected. Since the attractive forces from the sample are substantially weaker than the forces used in contact mode, the tip must be given a small oscillation at its resonant frequency so that detection methods can be used to detect the small forces between the tip and the sample by measuring the change in amplitude, phase, or frequency of the oscillating cantilever in response to force gradients from the sample. The fluid layer is usually thicker than the range of the van der Waals force gradient and therefore, attempts to image the surface with non-contact AFM under ambient conditions fail, as the oscillating probe may be trapped in the fluid layer or hovers beyond the effective range of the forces it attempts to measure [72]. However non-contact mode AFM is a very successful and useful method in ultra high vacuum.

The third common AFM mode is the so-called tapping mode. This technique is ideal for imaging sample surfaces that are easily damaged, loosely attached to their substrate or difficult to image by other AFM techniques. The tip is alternately brought in contact with the surface to provide high resolution and then moved away from the surface to avoid scratching over the surface. In tapping mode the cantilever is oscillated at or near its resonant frequency using a piezoelectric crystal. The cantilever oscillates with a high amplitude (typically greater than 20 nm), when the tip is not in contact with the surface. The tip is approached to the surface until it begins to lightly touch or tap the

surface.

The amplitude of the cantilever oscillation is reduced due to energy loss caused by the tip contacting the surface. This reduction can be used to identify and measure surface features. In contact mode, the preset scanning parameter is the deflection, while in tapping mode the cantilever oscillation amplitude is kept constant by a feedback loop (to the value chosen as setpoint). The amplitude is reduced when the tip passes over a bump in the surface, since it has less room to move. Passing over a depression, the cantilever has more room to oscillate and the amplitude increases and approaches the maximum free air amplitude. The oscillation amplitude is permanently measured and the digital feedback loop adjusts the tip-sample separation to re-attain the setpoint-amplitude.

Through this process the height data of the sample under investigation can be obtained. Another useful application of tapping mode is phase imaging. Phase data from a sample are obtained from the difference between the driven and the actual oscillations of the cantilever. This phase offset is caused by interaction with the surface and will be different for different materials, since it depends on various parameters such as adhesion, friction or viscoelasticity. Therefore phase imaging can help distinguish different areas of interest on the sample, see Fig. 35.
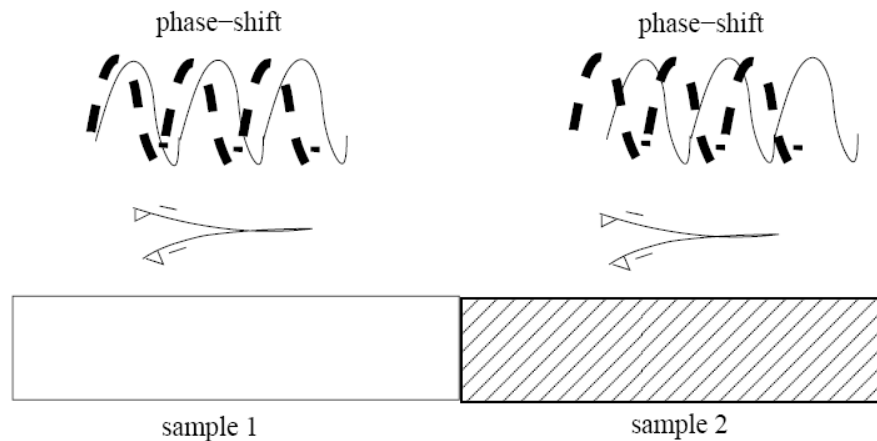
Figure 35: Different surface properties give rise to different phase shifts.

The high frequency (up to 500 kHz) makes the surfaces stiff (viscoelastic), and the tip-sample adhesion forces are greatly reduced. Unlike contact and non-contact modes, when the tip contacts the surface, it has sufficient oscillation amplitude to overcome the tip-sample adhesion forces. Additionally the surface material is not pulled sideways by shear forces since the applied force is always vertical [72].

In tapping mode AFM, three types of data may be collected (Fig. 36):

- Height data:
  Vertical motions of the tip are recorded as changes in the length of the z-piezo and displayed as a function of the lateral position. A topographic map of the investigated surface is created, with well defined heights of single scan elements, but no sharp edges visible.

- Amplitude data:
  The feedback loop attempts to keep the desired value of the amplitude at a constant value (setpoint). When the tip encounters abrupt height changes, the amplitude temporarily changes (error signal) and ideally returns to the setpoint value when scanning smooth sample areas. Effectively, when investigating imperfect samples, there is always an error signal. Its strength helps to detect sharp edges.

- Phase data:
  The phase signal of the input (to the piezo) is put in relation to the cantilever output signal and the phase shift is displayed.
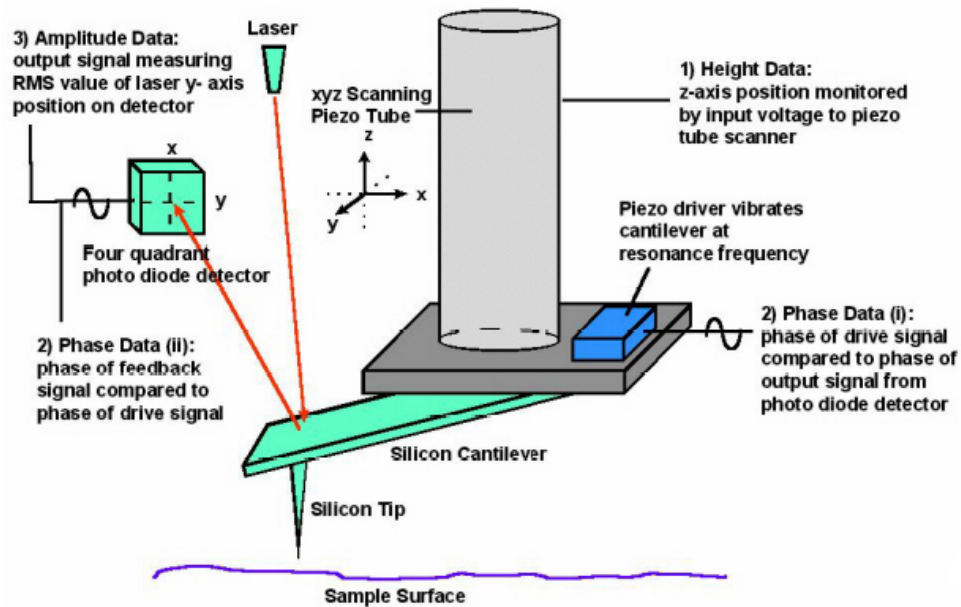
Figure 36: Schematic drawing of data types recorded in tapping mode [76].

Force curves

As the name suggests, an AFM can also record the force on the cantilever, when the probe tip is brought in close contact with, or even indented into the sample surface and then retracted. Force curves give detailed information on the local chemical and mechanical properties such as adhesion and elasticity. In addition, the correct interpretation of a force curve can help to measure the thickness of adsorbed molecular layers and to choose appropriate loading forces for measurements on different materials.
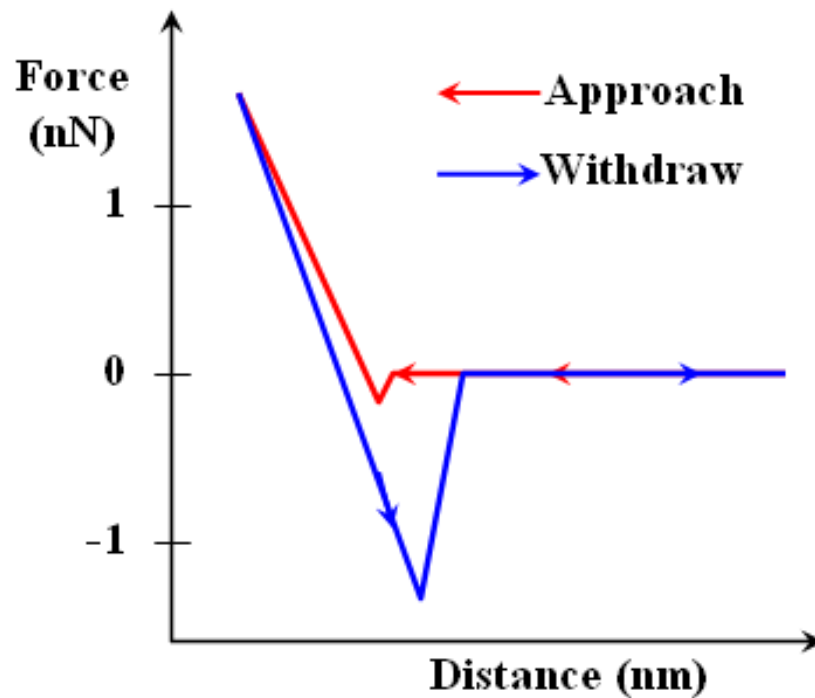
Figure 37: Idealized force curve from a hard sample [77].

Fig. 37 shows an idealized force curve. The starting point is far from the surface, where the cantilever feels no forces. As the probe tip approaches the surface, the attractive forces increase and the tip jumps into contact once they are sufficient. Once contact has been established, cantilever deflection (proportional to force) will increase, as the fixed end of the cantilever is moved closer to the surface. Depending on the spring constant of the cantilever, the tip may even indent the surface at this point. In this case, the slope or shape of the force curve in the repulsive regime can give information about the elasticity of the surface. After a desired value of force has been reached, the process is reversed and the cantilever withdrawn. This is the adhesive part of the force curve, where the deflection is lower than zero. Depending on the strength of the adhesive forces, the cantilever may stick to the surface some distance greater than the initial point of

contact in the approach. The point where the cantilever snaps free from the surface is of great interest as it provides information on the rupture forces necessary to break adhesive bonds.
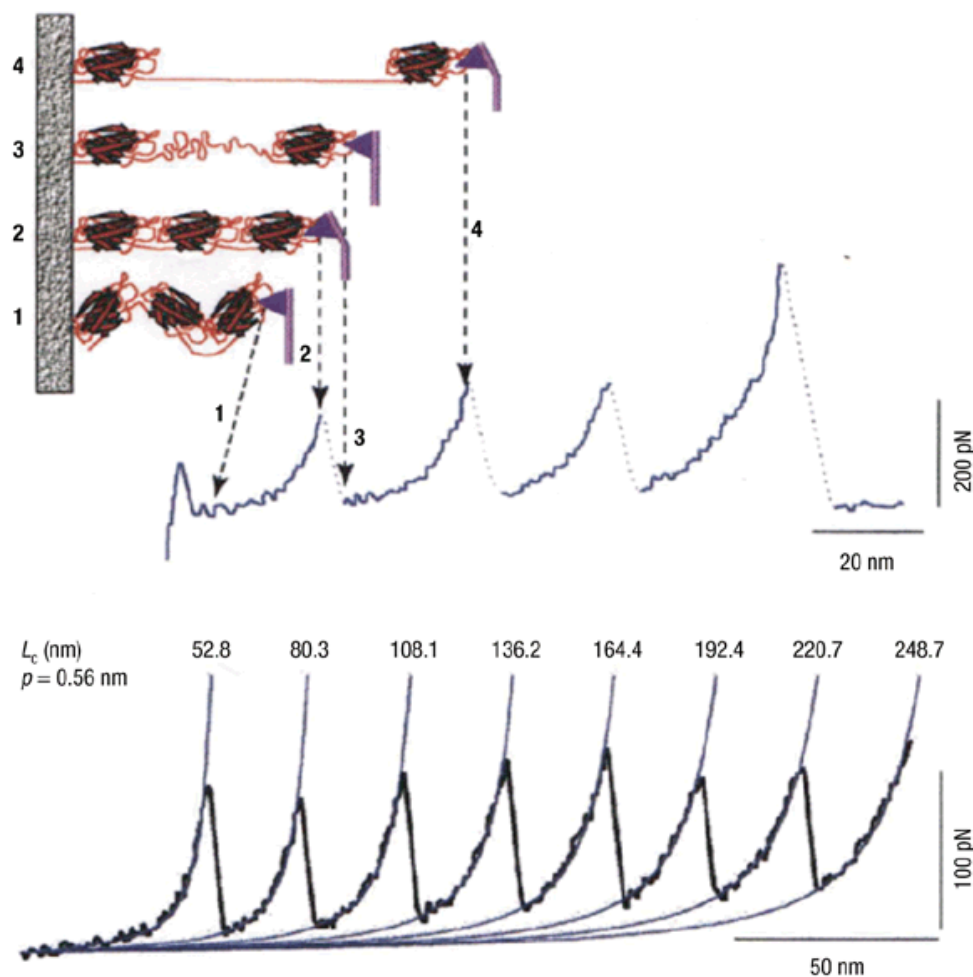

Figure 38: Peaks in the force curve mark unfolding events of protein domains [78].

This concept has found application in protein unfolding: Proteins are often folded in several subunits and can be pinned and stretched with a sharp tip. As the distance between the cantilever and the surface increases, the protein elongates and the cantilever bends. Upon the unfolding of a subunit, the force on the cantilever reaches a maximum value and approaches zero after the unfolding event, resulting in the saw-tooth pattern of peaks shown in Fig. 38.

Magnetic Force Microscopy

Another application that was introduced shortly after the invention of the AFM is the measurement of magnetic surface properties, termed as magnetic force microscopy (MFM). This technique employs a special probe coated with magnetic material. Interaction of the tip's magnetic moment with the magnetic stray fields near the sample surface determines the vertical motion of the tip during the scanning process [79].

MFM is based on the same operating principles as AFM and both static and dynamic detection methods can be applied. Due to the better sensitivity, the dynamic mode is preferentially used: The cantilever vibrates close to its resonance frequency and amplitude and phase of the oscillation are permanently measured with respect to the drive signal. Probe-sample interaction modifies the spring constant of the cantilever, where c is the natural spring constant and is the derivative of the interaction force relative to the perpendicular coordinate z.   An attractive interaction with $\delta F/\delta z > 0$ will make
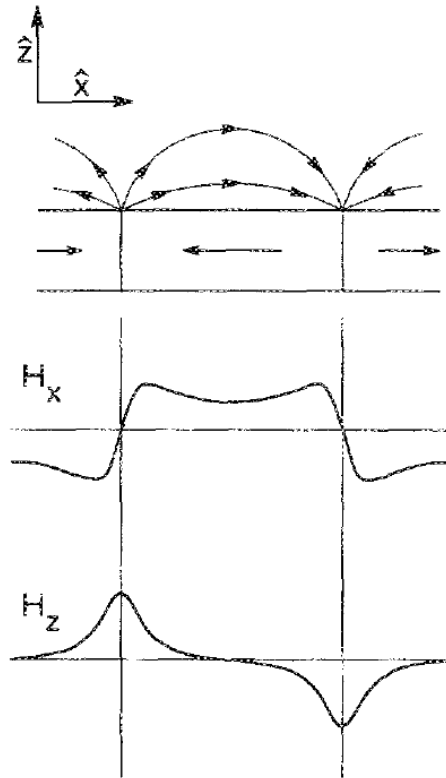
Figure 39: Geometry of magnetic stray field above longitudinal magnetic medium; typical variation of H_x and H_z above the medium [79].

the cantilever spring softer and the resonance frequency will decrease. This shift will also have an effect on the amplitude and the phase of oscillation, which can be used to

measure the lateral variation of the force gradient. The force derivative originates from various sources such as electrostatic interactions, damping, van der Waals or capillary forces. MFM relies on forces arising from a long-range magnetostatic coupling between probe and sample. The force acting on an MFM tip can be calculated as the negative gradient of the magnetic potential energy of the magnetized tip in the stray field of a sample:

$$F = -\nabla E = -\mu_0 \int \overrightarrow{M}_{tip} \cdot \overrightarrow{H}_{sample} \cdot dV_{tip} \qquad (4.1)$$

Because this coupling heavily depends on the internal magnetic structure of the probe, the mechanism of contrast formation in MFM imaging is quite complicated. Consequently, MFM can generally not be performed in quantitative way, i.e. measuring a stray field in absolute units.

The critical element of a magnetic force microscope is the cantilever/tip assembly. Cantilevers with integrated sharp tips are fabricated from silicon-based materials and can be coated with layers of magnetic material. In these layers, a pattern of magnetic domains will arrange, reducing the effective magnetic moment of the tip. The exact domain structure remains unknown and is likely to change during the scanning process.

Spatial resolution depends on the tip-sample distance as well as the magnetized part of the tip which is actually exposed to the stray field. For maximal lateral resolution, the magnetically sensitive region should be as small as possible, ideally a single-domain ferromagnetic particle. Superparamagnetism sets a physical limit for the dimensions of these particles.
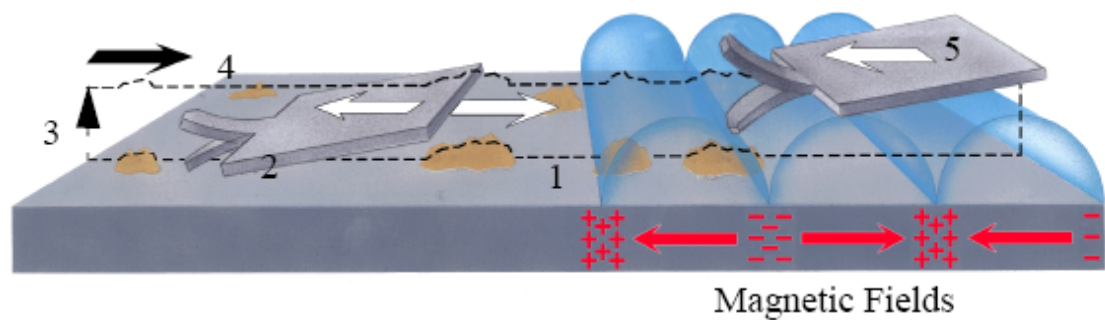

Figure 40: Schematic drawing of MFM: 1, 2: topographical trace and retrace, z sensor positions are recorded and stored; 3: lifting of cantilever to chosen delta height; 4, 5: magnetic trace and retrace, tip-sample separation is kept constant as the tip follows the height profile of the sample [80].

To achieve strong signals, it is necessary to maximize the magnetic moment of the tip. Furthermore it is desirable to maintain a well-defined magnetic state of the tip during

scanning. High switching fields can be realized through the influence of shape anisotropy, which forces the magnetization vector field near the probe apex to align with its axis of symmetry.

The most crucial part of the imaging procedure in MFM is distinguishing between nonmagnetic and magnetic interactions. This can be achieved by letting the tip follow the surface height profile, thus keeping the topography influence constant. In a first scan topographical information is recorded and stored. Then the tip is lifted to the so-called "delta height" and magnetic information is measured at constant tip-sample separation with the feedback turned off (Fig. 40).

As stated above, magnetic data can be recorded as variations in amplitude, frequency or phase of the cantilever oscillation. Frequency modulation and phase detection offer the better sensitivity and a higher signal-to-noise ratio. All measurements presented in this work employed the method of phase detection. The drive frequency is set to the center of the cantilever resonance, using the "Auto tune" mode of the instrument. The phase curve decreases with increasing frequency and crosses the center line (90° phase lag) at the peak frequency, similar to the case of a harmonic oscillator. A vertical gradient in the magnetic force results in a shift ΔF_0 in the resonance frequency, which in turn gives rise to a phase shift $\Delta \phi$ [80] (Fig. 41).
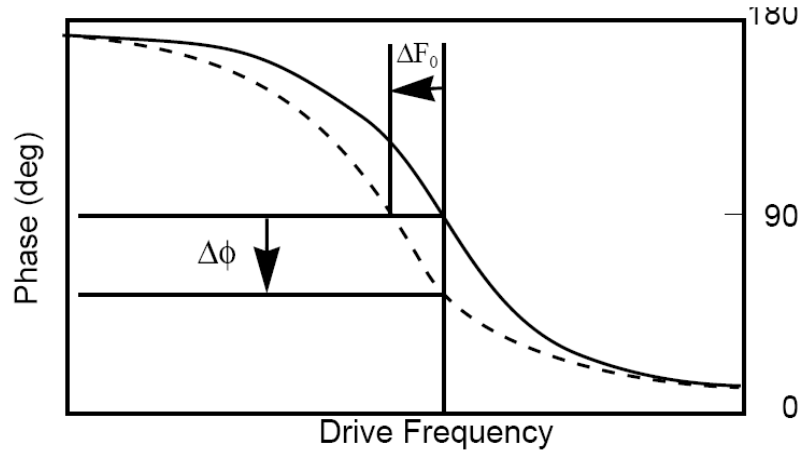
Figure 41: Frequency shifts due to magnetic force gradients give rise to phase shifts.

An attractive interaction ($\delta F/\delta z > 0$) causes a negative phase shift, displayed as dark contrast in the image, while a repulsive interaction ($\delta F/\delta z < 0$) gives a positive phase shift and bright contrast.

Figs. 42 and 43 show a topographic image and the magnetic signal of the same area of a 40 GB hard disk; topographic and magnetic contributions are separated successfully.
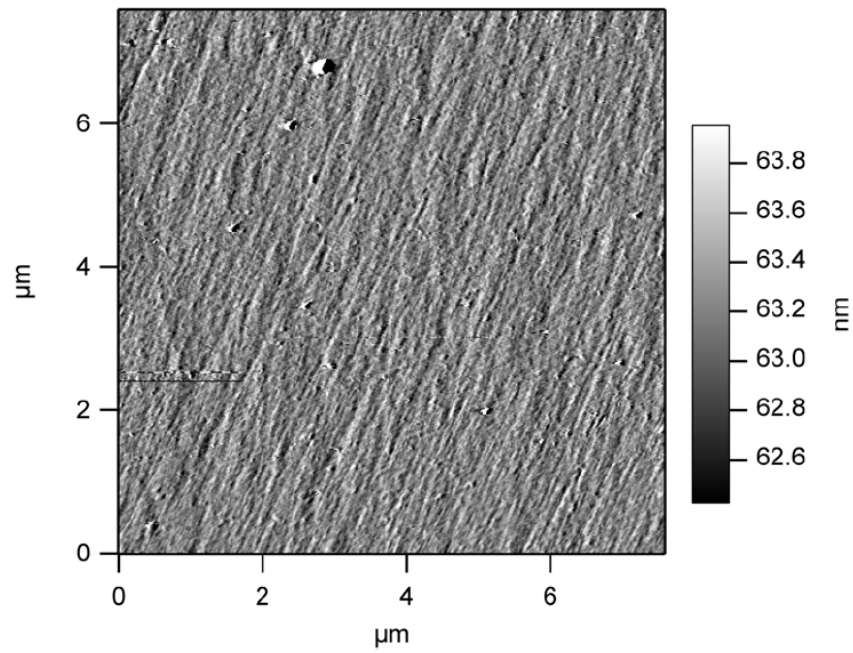
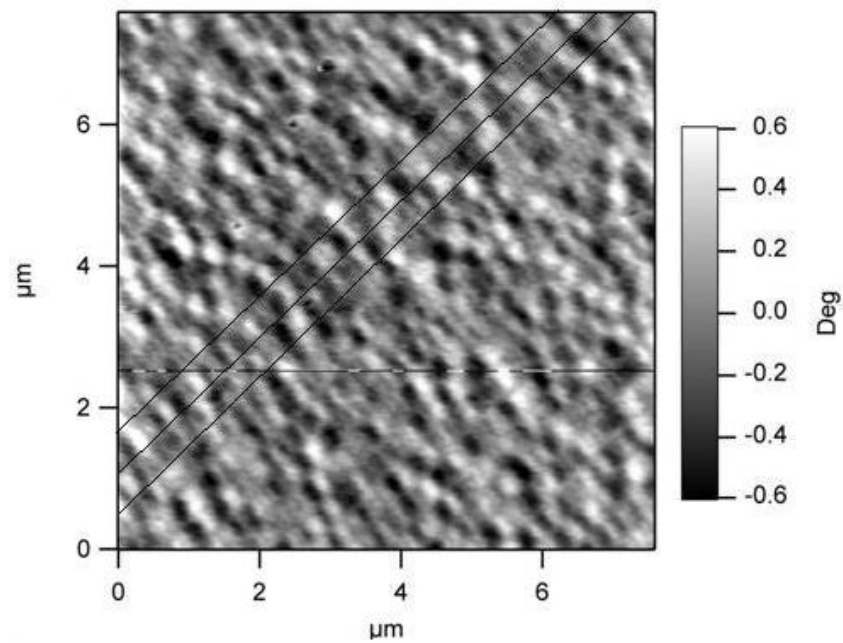Figure 42: Amplitude trace of a 40 GB hard disk.

Figure 43: Magnetic signal from the same area, "delta height": 50 nm, black lines separate adjacent lines of data.

5 Hillock formation: State of the art

For all investigated materials (CaF_2, HOPG and mica), a short description of structure and properties will be given followed by a summary of experimental data and knowledge about the hillock formation on the respective materials up to date. In chapter 6, the recent experiments will be presented and the results be compared to previous data.

Since all of the investigations on CaF_2 were performed within the TU Wien group and the most experimental data were collected, the emphasis will be placed on this material.

5.1 CaF_2

Calcium fluoride (CaF_2) is a water insoluble ionic compound of calcium and fluorine. It is also known as fluorite or fluorospar. Crystals adopt a cubic structure wherein calcium is coordinated to eight fluorine anions and each F ion is surrounded by four Ca^{2+} ions.
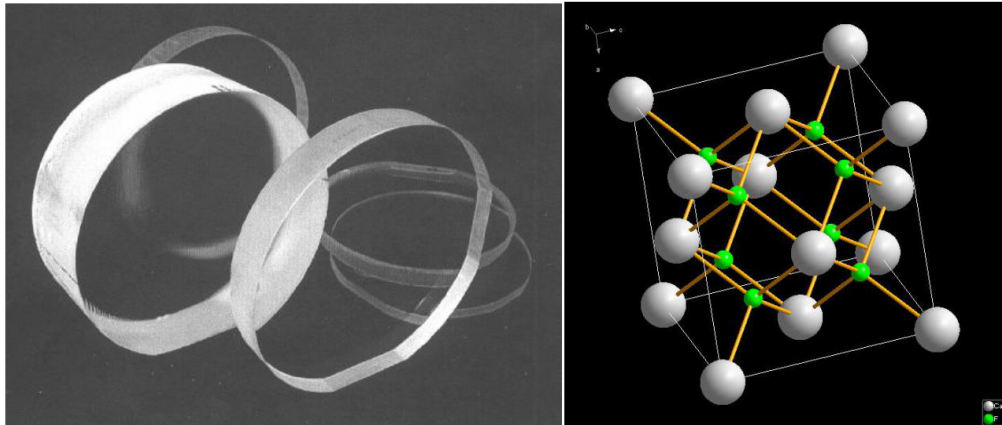
Figure 44: CaF_2 single crystals [81] and schematic crystal structure [82].

Applications:

- Naturally occurring CaF_2 is the principal source of hydrogen fluoride.

- Used as a window material and in camera lenses.

- Uranium-doped CaF_2: solid state laser.

5.1.1   First Results

First experiments [83] in which freshly cleaved CaF$_2$ single crystals at room temperature were irradiated with slow HCI were performed in 2006 with ^{129}Xe^{44+} ions extracted from the EBIT at the Max Planck Institut of Heidelberg. Cleavage of CaF$_2$ is known to result in a fluorine-terminated surface which is stable in air.

Several freshly cleaved CaF$_2$ samples were mounted in a vacuum chamber of pressure in the 10^{-10} mbar range and irradiated normal to the (111) surface . Two different ion impact energies (2.2 and 3.3 keV/amu) were used at typical ion fluxes of 10^4 ions/s, measured via an electron emission detection system [84] developed at the TU Wien, with close to 100% detection efficiency. Irradiation times of several hours resulted in a total ion fluence of ~ 2 x 10^9 ions/cm^2.
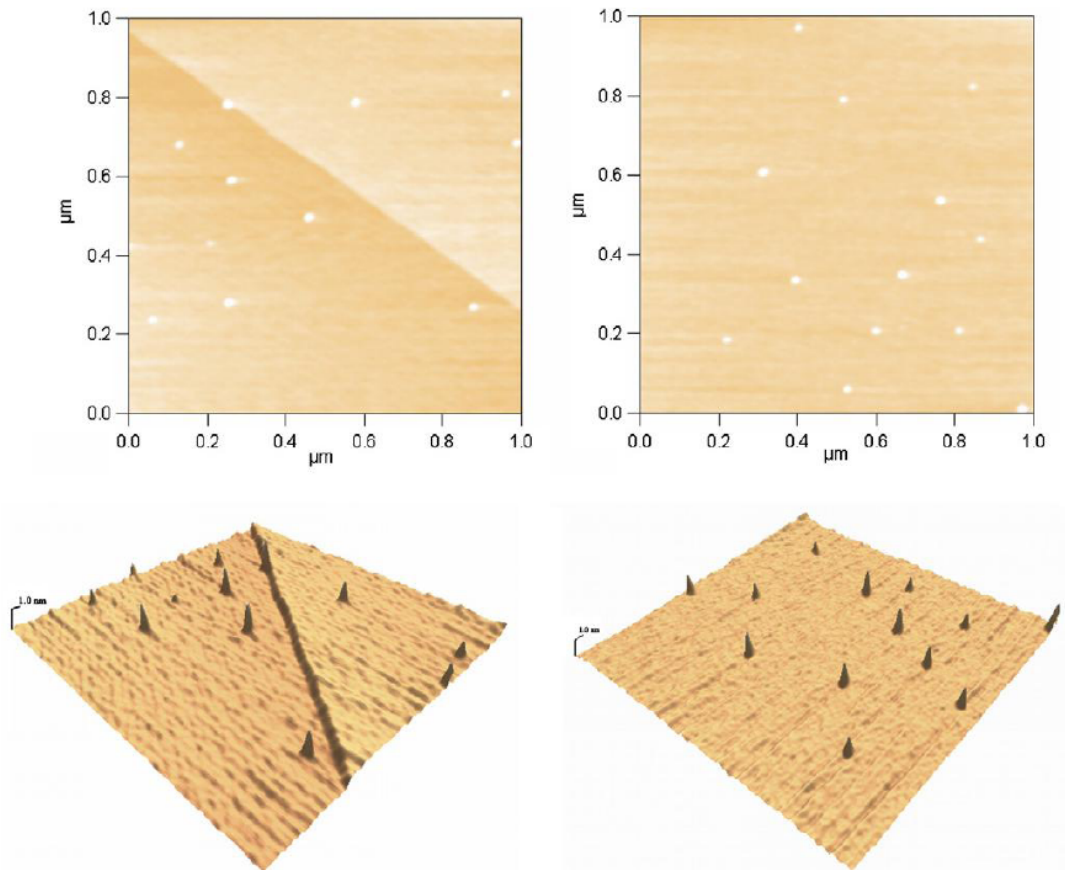
Figure 45: CaF$_2$ irradiated with Xe^{44+} ions at impact energies of 2.2 keV/amu (left) and 3.3 keV/amu (right) [83] .

The samples were investigated with an MFP-3D atomic force microscope (Asylum Research, Santa Barbara, USA) under ambient conditions. Images were obtained in contact mode using non-conductive Si$_3$N$_4$ cantilevers (supplied by Veeco, nominal spring constant: 0.1 N/m) and constant loading forces in the order of 10 nN. Fig. 45 shows typical AFM images of the irradiated samples taken from [83]. The number of hillocks was found to be in good agreement with the total dose, i.e. each individual projectile creates a protrusion. The existence of hillocks is somewhat surprising, as the electronic energy loss is much lower than the threshold of 5 keV/nm found in the case of swift heavy ion bombardment [6].

The diameter of an individual hillock is defined by the distance between two diametric points that mark the emergence of the hillock contour from the mean horizontal plane of the intact crystal surface [7]. Due to the finite AFM tip curvature radius, the evaluation of the hillock diameters might be afflicted with a systematic error in the order of a few nanometers. The accuracy in the determination of hillock height on the other hand is affected by the roughness of the sample rather than by the finite tip curvature radius. The mean dimensions were determined by fitting a Gaussian function (Fig. 46) to the hillock frequency-versus-diameter/-height histograms.
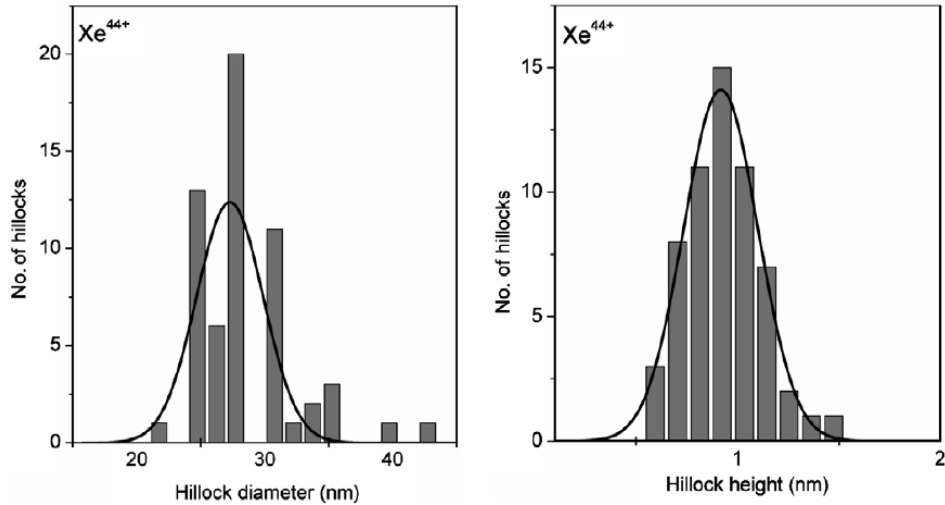

Figure 46: Evaluation of mean hillock dimensions for CaF$_2$ irradiated with 3.3 keV/amu Xe^{44+} ions [83].

Table 1 gives a summary of irradiation parameters and the evaluated mean values of hillock dimensions taken from [83] in comparison with data from swift Xe ion bombardment [7].

Ion-beam parameters and measured hillock sizes

	Slow Xe^{44+}	Slow Xe^{44+}	Swift Xe
Kinetic energy (keV/amu)	2.2	3.3	6400
Ion range (nm)	84	117	46000
Electronic energy loss (keV/nm)	1.09	1.31	19.5
Nuclear energy loss (keV/nm)	2.85	2.56	0.02
Mean hillocks diameter (nm)	28.1 ± 0.4	28.3 ± 0.5	23.5 ± 0.4
Mean hillocks height (nm)	0.9 ± 0.1	0.9 ± 0.1	3.8 ± 0.2

Table 1: Summary of irradiation parameters and mean hillock dimensions [83].

Since the estimated electronic energy loss was well below the kinetic energy threshold and the hillock dimensions are virtually independent on the ion impact energy (see Table 1), it was concluded that the potential energy stored in the Xe^{44+} projectiles (51 keV) is responsible for the hillock production.

These first promising results set the stage for more detailed investigations, i.e. on the variation of hillock dimensions with charge state and ion species and theoretical explanations thereof, which will be described in the following.

5.1.2   Charge state dependence - Potential energy threshold

A second series of irradiations was performed at the Heidelberg EBIT to determine the dependence of hillock dimensions on the potential energy of the incident ions [9].

HCI of less than 5 keV/amu were extracted at an acceleration voltage of 10 kV (and in addition 6.4 kV for Xe^{44+}), namely ^{40}Ar^{q+} (q = 11, 12, 14, 16, 17 and 18) and ^{129}Xe^{q+} (q = 22, 26, 28, 30, 33, 36, 40, 44, 46 and 48). The projectiles with a resulting kinetic energy of 10 kV times charge state q have projected ranges between 90 and 140 nm in CaF$_2$, assuming that stopping power and range are not affected by the high charge state.
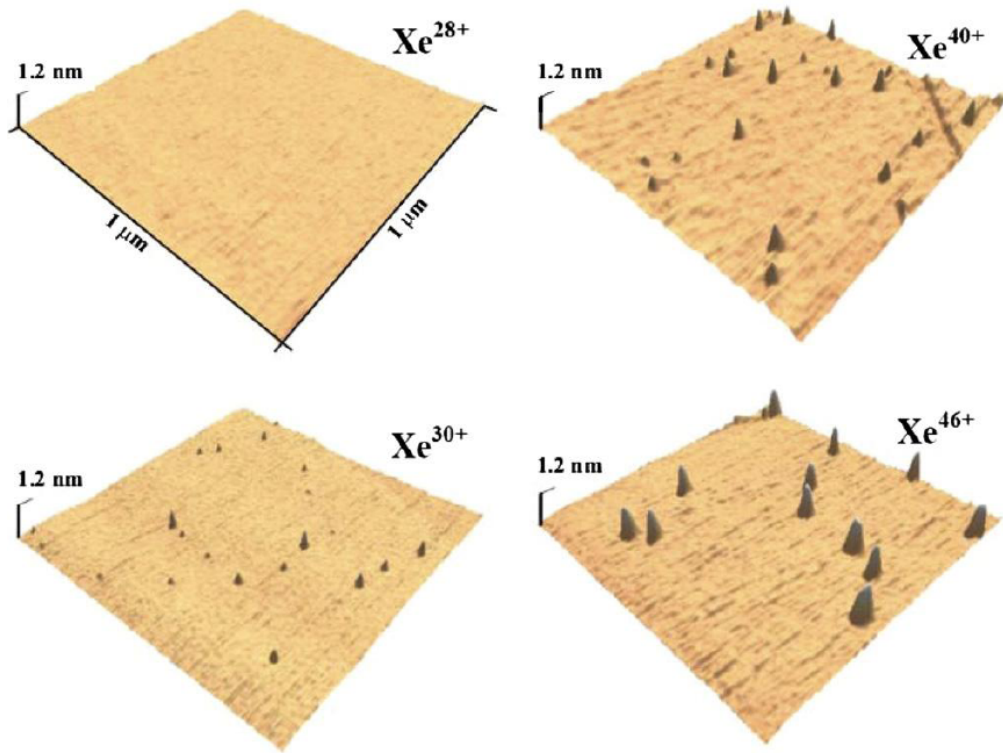
Figure 47: Hillock formation on CaF$_2$ for different Xe charge states at kinetic energies of 10 keV q.

Fig. 47 shows the evolution of hillock formation on Xe^{q+}(q = 28, 30, 40, 46) irradiated CaF$_2$ samples. Projectiles with charge states below q = 30 do not create hillocks, above the observed "threshold", diameters as well as heights of hillocks increase.

For Ar^{q+} irradiated samples only fully stripped ions (q = 18) are able to produce structures. The sharp transition e.g. between q = 17 and 18 of Ar cannot be associated with irradiation parameters in an obvious way. Moreover, results from measurements with 6.4 q keV (2.2 keV/amu) Xe^{44+} differ by less than 5% from the data of 10 q keV

(3.4 keV/amu) Xe^{44+} ions. This is a further indication that the kinetic energy has little impact on the dimensions of the nanostructures.

Evaluation of the AFM images reveals height ranges between 0.5 and 1 nm and diameters between 20 and 60 nm of the found hillocks. Determination of the hillock-density shows that a large majority ($> 70\%$) of incident ions produces an individual hillock each.
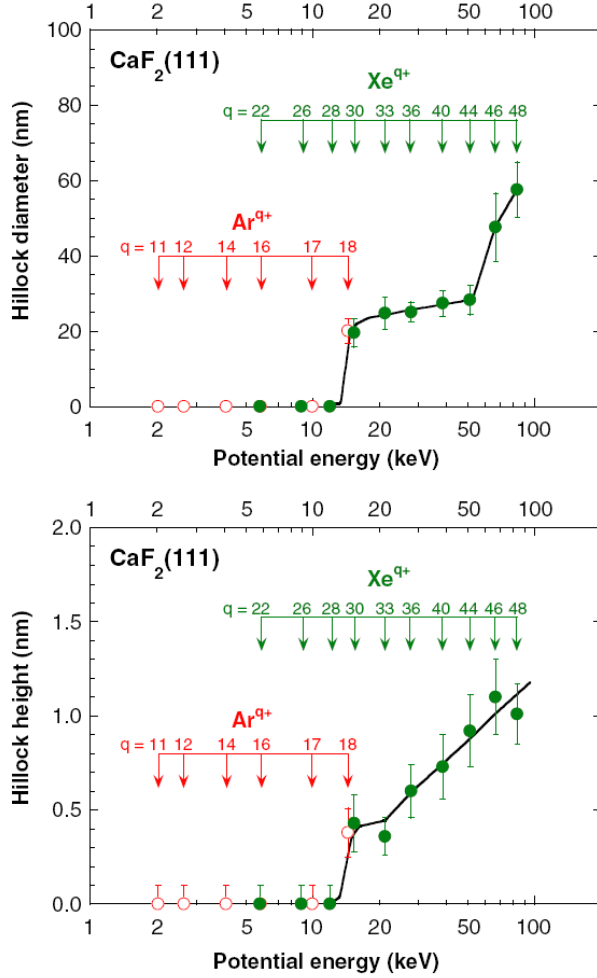

Figure 48: Mean hillock dimensions as a function of potential energy [9].

Additionally to the threshold between Ar^{18+} ($E_p = 12.2$ keV) and Xe^{30+} ($E_p = 14$ keV), a steep increase, especially in the basal diameter (cf. Fig. 48), is found in the between Xe^{44+} and Xe^{46+}, possibly indicating a second threshold.

First theoretical approaches ([9], [112]) associate the observed thresholds with phase transitions of melting and sublimation caused by the deposition of the potential energy in the electronic subsystem. A detailed description of the proposed scenario will be given in the chapter 6.

5.2   HOPG

HOPG (highly ordered pyrolytic graphite) is a highly ordered form of graphite. Graphite and diamond are the two allotropes of carbon, graphite being its most stable form under standard conditions. The structure can be described as lamellar, consisting of identical stacked planes. Atoms within the planes are covalently bond, whilst individual planes are loosely bonded together by weak van der Waals forces, explaining the characteristic cleaving properties. Three principal types occur naturally: Crystalline flake graphite, amorphous graphite and lump graphite

Graphite crystallizes either in hexagonal (alpha) or rhombohedral (beta) crystal structure, both forms showing similar physical properties. The acoustic and thermal properties of graphite are highly anisotropic as phonons travel quickly along tightly-bound planes, but slower from one plane to another. Vast electron delocalization within the carbon layers makes graphite an electrical conductor, but electricity is almost exclusively conducted within the plane of the layers.
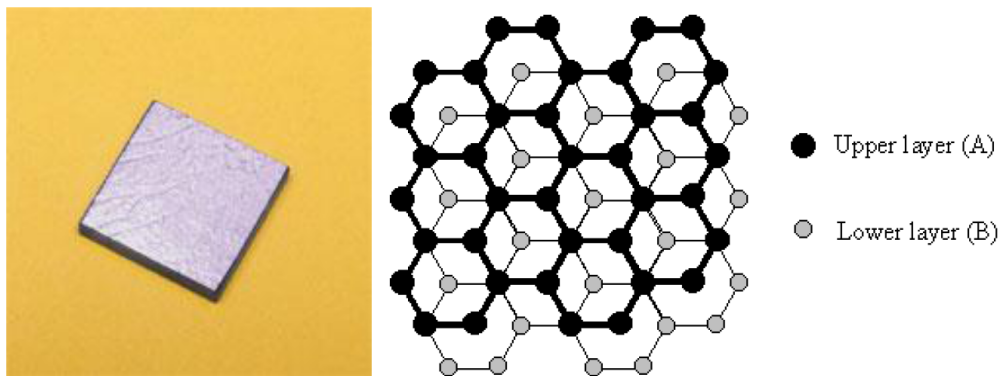
Figure 49: HOPG sample [85] and schematic crystal structure [86].

Applications of graphite [87]:

- Refractory materials: electrodes in electrical metallurgical furnaces.

- Chemical industries: anodes in electrolytic processes.

- Nuclear industries: moderator rods in nuclear reactors.

- Electrical industries: carbon brushes in electric motors.

- Mechanical applications: piston rings, thrust bearings, etc.

- Heat shield for space crafts and wall material in thermonuclear fusion experiments.

- HOPG: calibration tool for probe microscopies.

5.2.1   Previous experiments

Since the introduction of the scanning tunneling microscope in 1982 and the subsequent rapid developments in scanning probe microscopies, graphite, especially in its highly ordered form HOPG, has been subject to a multitude of experimental studies. The lamellar structure of HOPG allows for simple cleavage with adhesive tape, resulting in large atomically flat terraces which extend over several hundreds of nm. The simple preparation and reproduction of flat standard surfaces have made HOPG a favorable material for investigations on the effect of ion bombardments. Such investigations have been performed since the late 1980's by several research groups ([88] - [100]) and fueled by the advancement of ion sources and measurement devices until the present day. This section gives an overview of the experimental work up to date and conclusions made as a consequence thereof [2].

Early studies were performed with singly charged Ar ions at implantation energies of 50 keV by Porte et al. [88]. Researchers reported the occurrence of hillocks in the STM images with heights in the tenth of nanometer range and diameters in the nanometer range. A one to one correlation between the number of hillocks and the number of implanted ions was found. By changing the tunneling conditions in the STM mode, height barrier measurements were performed on the hillocks. As there was no evidence for change in the work function on the hillocks, the observed structures were associated with a crystalline modification of the surface, i.e. the raising of the surface was attributed to interplanar stresses which are generated along the ion track. At the time, however, no corresponding AFM data were collected in order to have evidence of real topographic modification.

Mochiji et al. [89] attempted to obtain first information about dependences of the defect size on potential energy and kinetic energy of the impinging ions. Samples were irradiated with Ar^+, Ar^{4+} and Ar^{8+} ions, extracted from an ECRIS at a voltage of 7 kV. Final impact energies were selected by means of an ion decelerator (1 - 0.25 kV x q). STM imaging revealed hillocks for all combinations of charge states and kinetic energies. Evaluation of the mean dimensions of the structures led to the conclusion that potential energy is more effective in producing defect size increase than kinetic energy. For example, a similar size was found for Ar^{4+} (E_p = 162 eV) induced defects at a kinetic energy of 2 keV as for Ar^+ (E_p = 15 eV) induced defects at a kinetic energy of 15 keV. Additionally, a strong increase of the defect size, particularly of the diameter, was observed as a function of charge state at fixed kinetic energies (Fig. 50).

Since the STM image is produced by the partial electron density near the fermi level, it is merely impossible to make definite conclusions on the topographic aspects of the features without corresponding AFM measurements. In the previously described study [89], however, no protrusions were found in the scanning force mode and the combination of STM and AFM data led the authors to the assumption that the surface modification is due to the enhancement of partial charge density of state at the surface as a result of carbon atom sputtering.
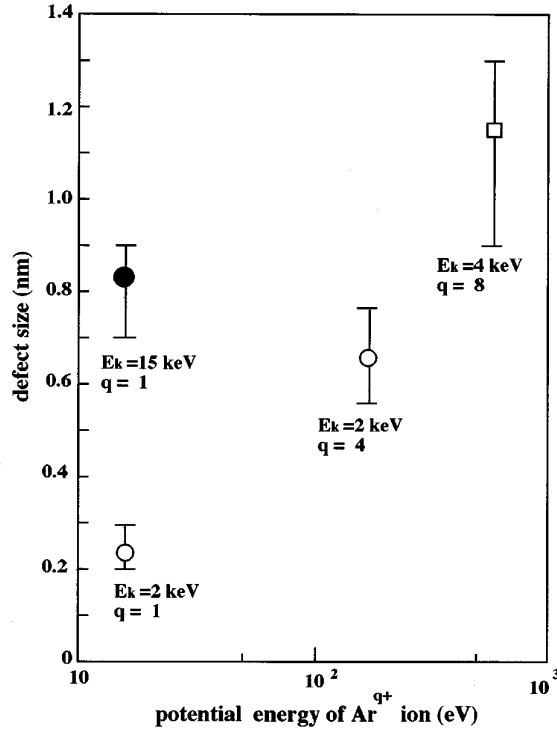
Figure 50: Hillock diameters on HOPG as a function of potential energy [89].

It should be noted that contact mode AFM in air, partially due to the large tip diameter ($\sim$ 5 - 10 nm), is poorly sensitive to atomic-scale defects. Moreover, the vertical resolution of this technique might not be sufficient to resolve the structures whose height (at least for the investigated charge states) is in the area of the standard noise level. Investigations of the TU Wien group ([90], [91]) implied a new technique, allowing for in-situ measurements (no breaking of the ultra-high vacuum (UHV)) of the bombarded samples by transporting them in an UHV suitcase (pressure below 10^{-9} mbar provided by a battery operated ion getter pump). With this method it became possible to rule out possible influences from target sample exposure to air.

Ar^{q+} (q = 1, 8 and 9) ions were extracted from a 5 GHz ECR source and decelerated to final impact energies of only 150 eV upon impact on the samples under normal incidence. Again, defects were found for all charge states in the STM images and their number was found to be in good agreement with the applied ion dose. An increase in lateral size and, to a lesser extent, height of the features was observed as the charge state and hence the potential energy became higher. Analysis of the tunneling current images via Fourier transformation and filtering showed a $(\sqrt{3} \times \sqrt{3})$ R 30° surface reconstruction in the vicinity of most defects (Fig. 51).
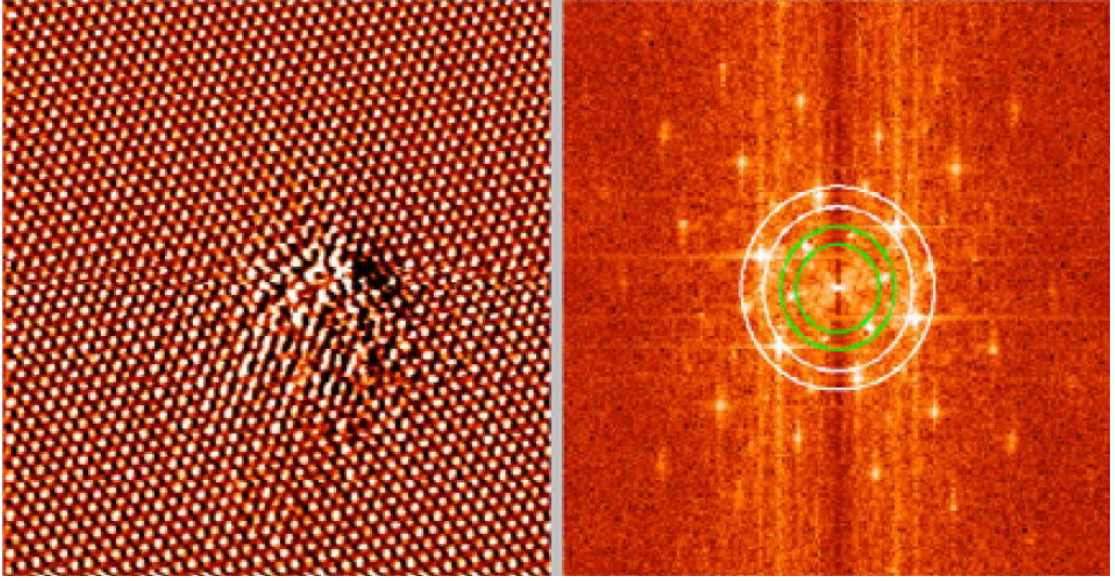
Figure 51: Typical STM image of an ion-induced hillock on HOPG (left) and Fourier transform of a tunneling current image (right) [91].

AFM imaging in UHV did not yield any evidence of topographic changes due to the ion bombardment. There are two types of defects caused by low energy ion bombardment in HOPG [101]: Vacancy defects (VD) and intersitial defects (ID), e.g. caused by trapping of the projectile beneath the first graphene layer, both resulting in an enhancement of the local charge density of states and hence seen as protrusions in the STM image. As the observed surface reconstruction is characteristic for ID creation, the researchers assumed that the hillocks are due to IDs or VDs created along with IDs.

The strong increase of defect diameter for higher charge states was interpreted as a "pre-equilibrium" effect of the stopping of slow multiply charged ions in HOPG: The conversion of the MCI to hollow atoms is coupled with a reduced screening upon final deexcitation within the solid which could result in a strongly increased energy loss of the projectiles. This effect, in turn, would lead to the creation of IDs located closer to

the surface and more VDs due to a higher momentum transfer to the first carbon plane.
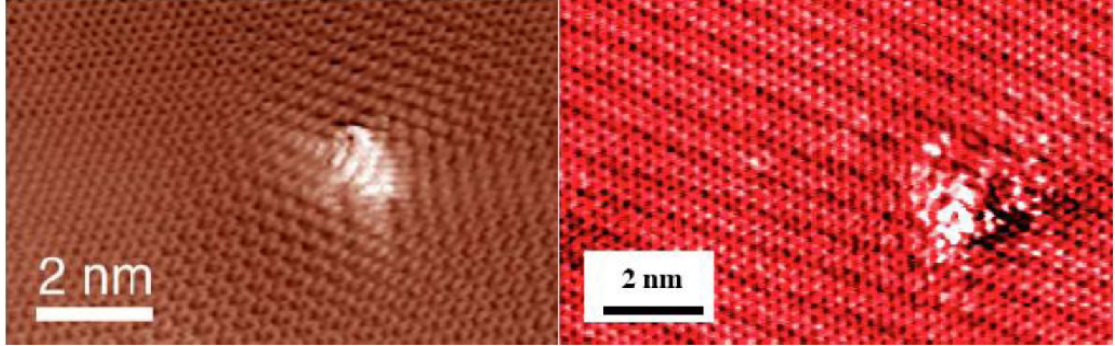

Figure 52: Defects induced by slow Ar^{9+} ion bombardment (left, [90]) and by swift Xe ions (right, [92]) show a comparable size.

Fig. 52 shows a typical STM image of an Ar^{9+} ion induced defect compared to a defect created by impact of a single Xe ion with 1.47 GeV [92]. The size of the defects is very similar and also the amount of electronic energy deposited in the first atomic layer of the target is in the same range for both cases.

Another interesting approach to the field was undertaken by Minniti et al. [93], who have developed a special combination of tools to establish ideal experimental conditions: They combine an EBIT source with an integrated STM, allowing for in-situ measurements on the irradiated samples. With this apparatus first experiments could be performed in the highly charged regime, extending the previously described potential energy studies by more than two orders of magnitude. Two charge states were considered (Xe^{23+} and Xe^{44+}) for investigation at a fixed kinetic energy of 276 keV. Evaluation of the found hillocks (Fig. 54) gave mean basal widths of 3.3 nm (Xe^{23+}) and 6.6 nm (Xe^{44+}). This steep increase can be explained in terms of different amounts of potential energy compared to kinetic energy deposited in the near surface region for the two cases: According to SRIM calculations [43], only about 16 keV of the ions' total kinetic energy is deposited within the first 5 nm of their path. For a Xe^{44+} ion ($E_p = 51.83$ keV) the potential energy dominates the kinetic contribution, while for a Xe^{23+} ion ($E_p = 6.58$ keV) the situation is reversed. As a result, the transfer of the potential energy from the Xe^{44+} ion plays a dominant role and is the expected cause for the observed charge state dependence.

The researchers considered two, earlier established, theoretical models as a starting point to explain the response of surfaces to HCI impact: The first is based on "Coulomb explosion" (see section 2.2.4): The neutralization of the impinging ion leaves behind multiple holes and a resulting near surface charge that can be greater than the HCI's
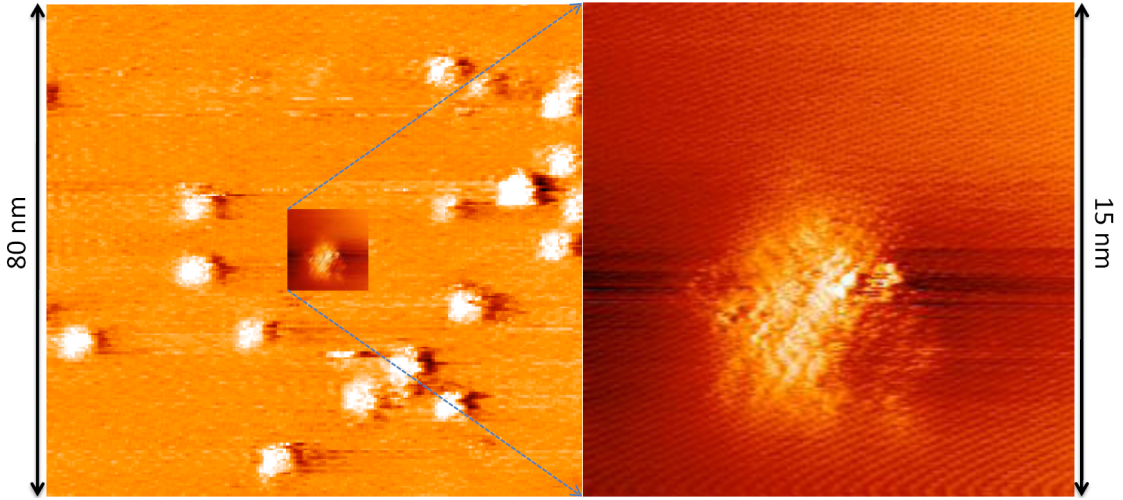
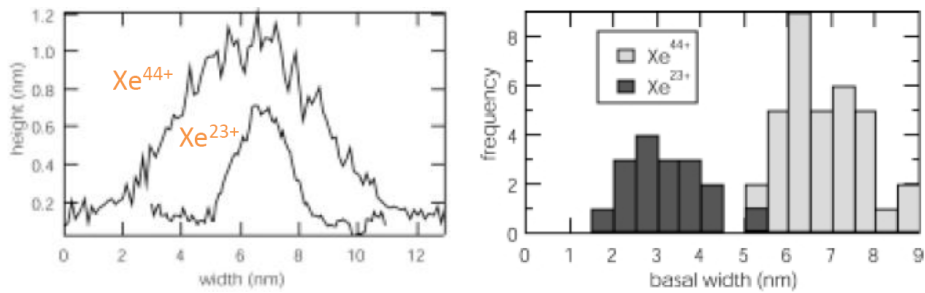Figure 53: Defects on HOPG induced by Xe44+ ions with a kinetic energy of 2.1 keV/amu [93].

Figure 54: Evaluation of mean hillock dimensions on HOPG after irradiation with Xe^{23+} and Xe^{44+} ions [93].

initial charge. This charged volume can "Coulomb explode", ejecting ions from the surface and initiating a shock wave which causes sputtering of neutral surface atoms. The second model describes the expulsion of surface atoms as a consequence of the conversion of covalent bonds in the lattice to antibonding potentials (see section 2.2.4). This process is proposed to be due to a localized region of multiple electronic excitation caused by the impact of the HCI. This scenario is similar to the structural instability model which describes surface sputtering by intense laser pulses [45].

Obviously, both of these models predict removal of matter and thus the appearance of craters rather than the protrusions seen in all the above studies. To explain this apparent discrepancy, the authors propose that the layered structure of graphite has to be taken into account. The weak van der Waals bonding of the graphene layers possibly allows for easy delamination and causes Coulomb explosion to result in a protrusion as

seen in the STM images. In the structural instability model, delamination could be a consequence of local target expansion caused by the stretching of bonds from electronic excitation.

Meguro et al. [94], [95] reported the occurrence of "nanodiamonds" on HOPG surfaces after bombardment with Ar^{8+} ions (400 eV kinetic energy) and subsequent treatment of the impact region with electron injection from an STM tip or He-Cd laser irradiation. The formation of these structures is ascribed to a localized transition of sp^2 to sp^3 hybridization. Experimental evidence of this transition was found in the I-V characteristics
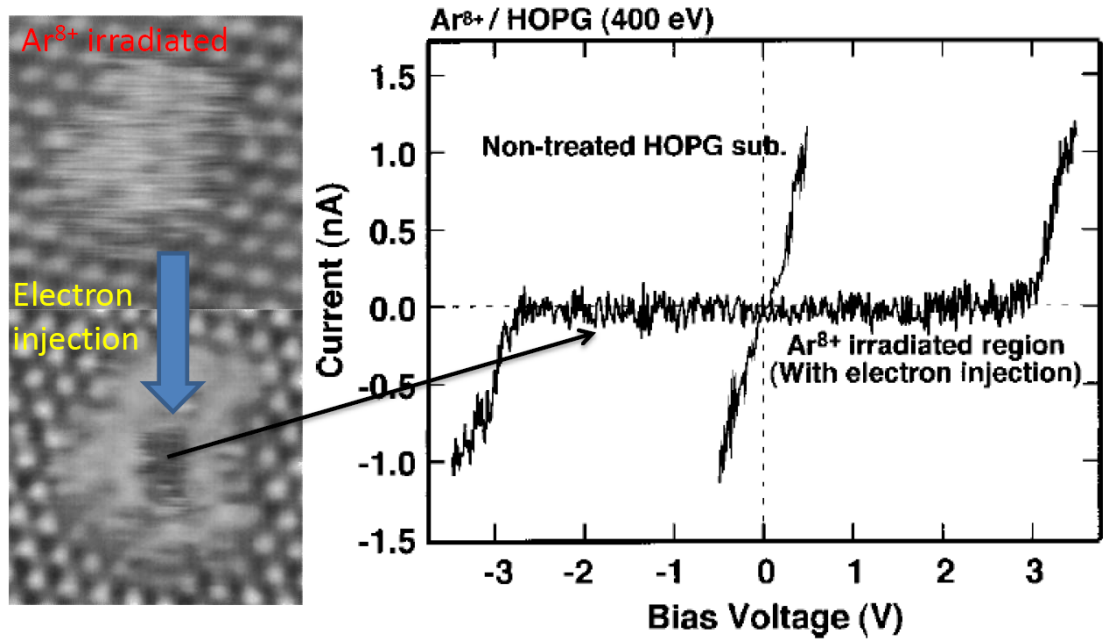
Figure 55: "Nanodiamonds" on HOPG: I-V characteristics of the treated area as well as of the non-treated substrate are shown [94].

of the treated area (dark area in Fig. 55) and its surrounding. The curves show metallic characteristics around the dark area, which itself becomes nonconductive. Additionally, the bandgap of bulk diamond (~ 5.6 eV) is very similar to the obtained value. Raman spectra were recorded to confirm the results from the STM measurements.

By using two different ion sources which provide charge states below and above Z^{40+}, respectively, Nakamura et al. [96] were able to extend the studies on energy dependences. Fig. 56 presents dimensions of Xe^{23+} ion induced defects in a kinetic energy range of 1 - 300 keV together with the data from [93]. No pronounced kinetic energy dependence is perceptible. In Fig. 57 the dependence on the incident ion charge is plotted together with the results from the previously described studies ([89], [90] and [93]).
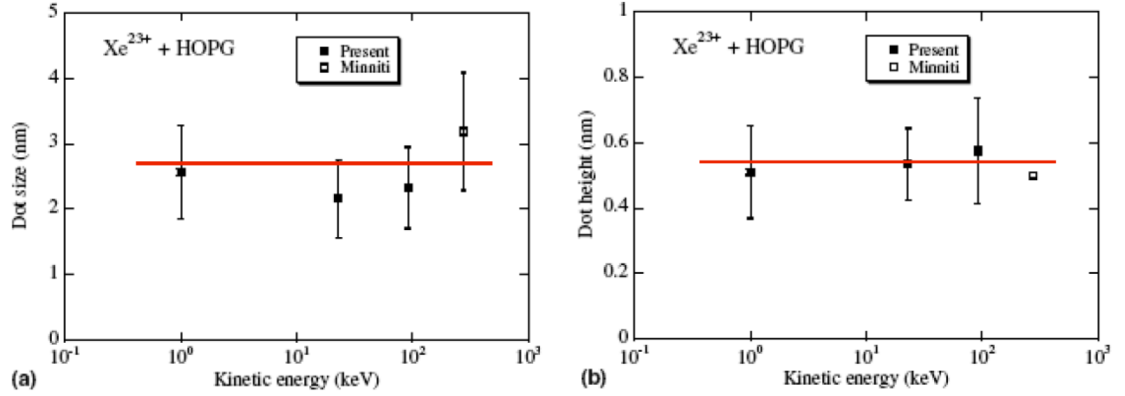
Figure 56: Dependence of hillock dimensions on the kinetic energy of Xe^{23+} ions in a range of 1 - 300 keV [96].
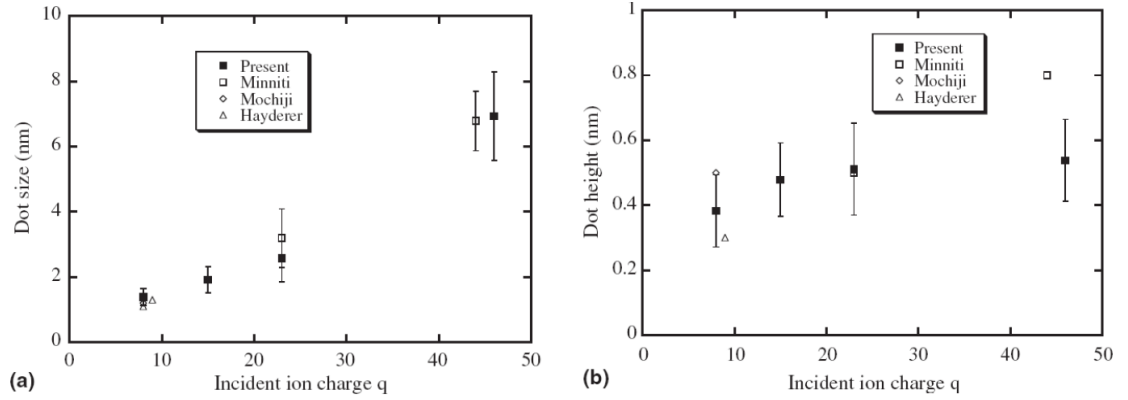

Figure 57: Dependence of hillock dimensions on incident ion charge state [96].

Again a clear increase in diameter with rising charge state is evident which is also, although to a somewhat lesser extent, true for the height.

As stated earlier, the non-existence of protrusions in the AFM images, has led the respective researchers to the assumption that the observed structures are no real topographic surface modifications but rather correspond to a change in the electronic density of states.

Terada et al. [97], however, were able to see structures in both imaging modes. Areas of Xe^{46+} (kinetic energy of 138 keV) irradiated samples were recorded in STM mode and hereafter imaged in non-contact AFM mode under UHV conditions without changing the tip (Fig. 58).
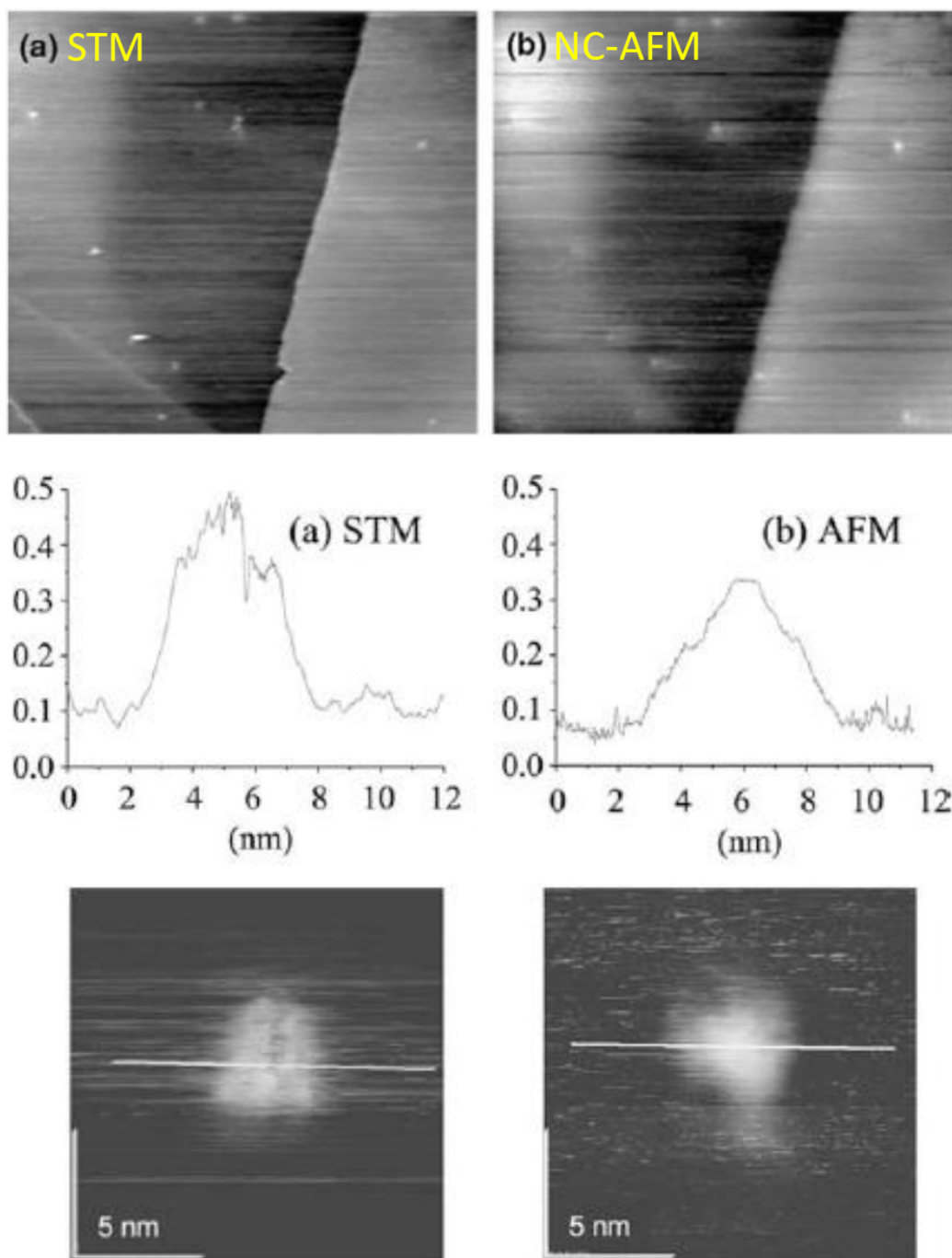
Figure 58: Xe^{46+} ion-induced defects observed in both STM and AFM imaging mode [97].

It should be noted that both the charge state and kinetic energy used in this study were considerably higher than in previous experiments which attempted to image structures with AFM. The strong repulsive forces in contact mode AFM, which was used in the previous studies, might damage the features created by the HCI. Moreover, several groups reported that no true atomic resolution (i.e. imaging of individual atoms) was achieved in contact mode, although they were able to image the periodic structure of the surface. Further studies are therefore necessary to conclude under which conditions (combinations of potential and kinetic energy, contact or non-contact mode) the structures can be resolved by means of AFM.

An et al. [100] found hillocks on HOPG samples irradiated with singly charged Ar ions applying tapping mode AFM. The observed structures with heights of 0.08 - 0.15 nm are much smaller than those described in the former case ($\sim$ 0.5 nm). For future studies, it might be worthwhile to also take this technique into consideration.

Finally, Figs. 59 and 60 show the dependence of mean hillock diameters and heights on the potential energy as a summary of the experimental data obtained at different kinetic energies from the studies described above.
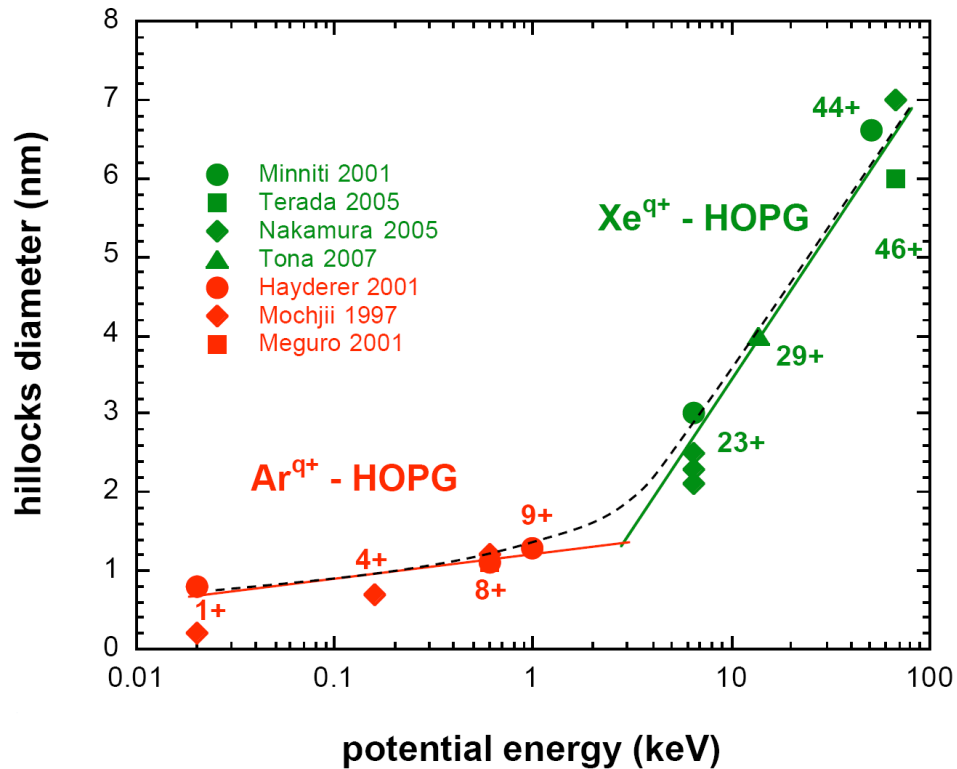
Figure 59: Summary of observed hillock diameters as a function of potential energy [2]. Data taken from ([89], [90], [93] - [97] and [99]).
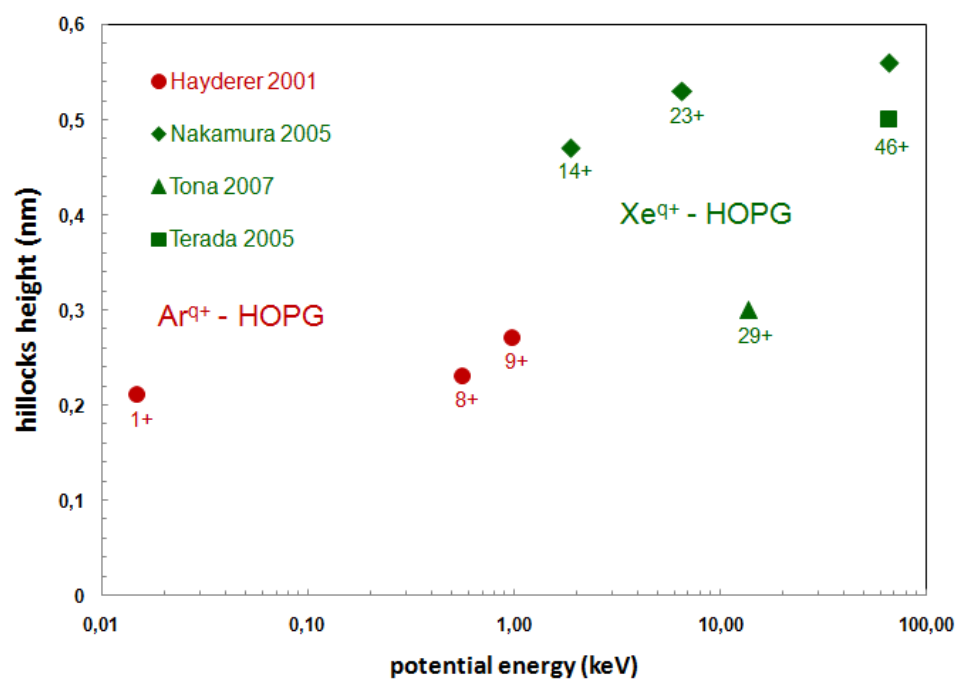
Figure 60: Summary of observed hillock heights as a function of potential energy. Data taken from ([90], [96], [97] and [99]).

5.3 Mica

The mica group belongs to the sheet silicate materials and includes several closely related materials. All are monoclinic with a tendency towards pseudo-hexagonal crystals. Similar as for graphite, the hexagonal sheet-like arrangement of the atoms results in highly perfect cleavage.
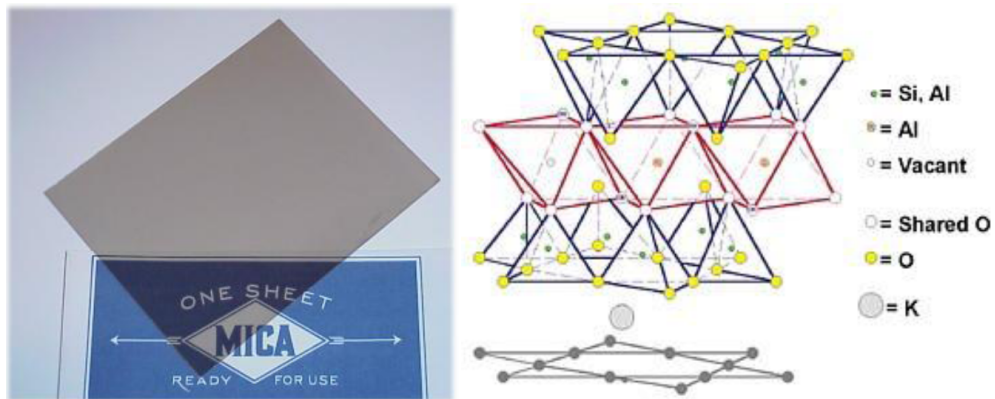

Figure 61: Muscovite mica sheet [102] and schematic drawing of crystal structure [103].

Applications:

- Material for capacitors for radio frequency applications.

- Insulator in high voltage electrical equipment.

- Used instead of glass in furnaces and kerosene heaters because of high heat resistance.

- AFM: Muscovite mica $KAl_2(AlSi_3O_{10})(OH)_2$ is one of the most common substrates.

5.3.1   Previous experiments

Mica is considered a favorable material to explore ion-induced modifications for a variety of beneficial properties. It is known to be a very good insulator and simple sample preparation by cleaving with adhesive tape or razor blades gives atomically flat surfaces with occasional occurrence of atomic steps. Mica is a commonly used substrate for AFM investigations or as a calibration material and is known to be stable under contact mode force microscopy.

First studies on the influence of slow HCI impact on mica surfaces were performed by the group at Lawrence Livermore National Laboratory ([104], [105]). In the first work, the cleaned and cleaved mica surfaces were bombarded with Kr^{35+}, Xe^{44+}, Th^{74+} and U^{70+} ions extracted from an EBIT source at typical velocities of 2.2 keV/amu and total ion fluences of $\sim 10^9$ ions/cm^2. AFM investigation in contact mode revealed hillocks for all investigated charge states which are, comparing the number of found defects to the ion fluence, a consequence of single ion impact.

The defects generated by Xe^{44+} ion bombardment had a height of about 0.4 nm and a base diameter of about 10 nm. The range of hillock height in the complete series was around 0.1 - 3 nm, and diameters from 10 - 60 nm were found. The mean hillock volume as a function of projectile charge state shows a somewhat linear increase due to an increase in diameter rather than height. Increasing the potential energy seems to have a lesser effect on the height which does not display the same pronounced increase as the diameter. A similar behaviour was found in the systematic studies of defect creation on HOPG.
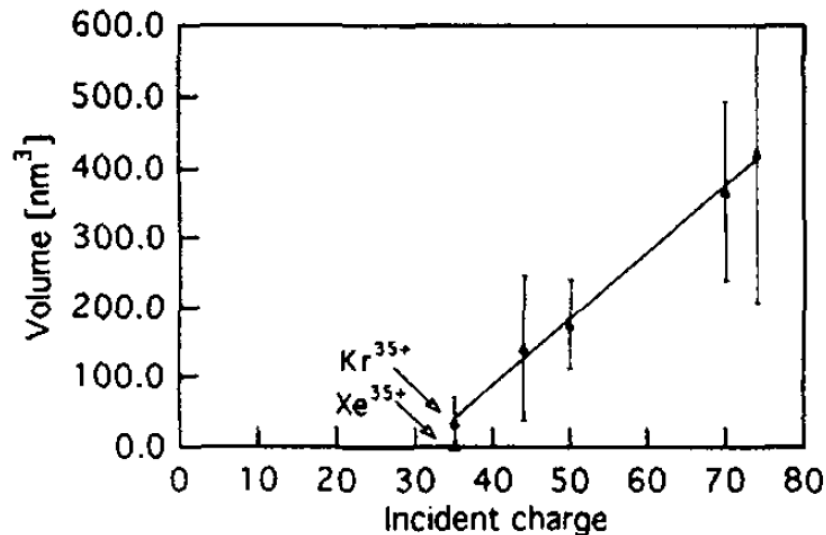

Figure 62: Mean hillock volume on mica as a function of incident ion charge [105].

Additional irradiations with singly charged and Xe^{35+} ions did not yield evidence of a topographical surface modification. From the experimental data, it was proposed that there should be a threshold charge state for the formation of hillock-like defects on mica at around q $\sim$ 30 (Fig. 62).

Two theoretical models were proposed to explain the mechanism of defect creation. One is based on the Coulomb explosion model (see section 2.2.4), the other associates defect production with the enclosure of neutral entities, indicated by the observation that similar defects are caused by heating of the mica substrate. Heating could lead to expansion of the trapped volumes or to disturbance of the charge balance by displacement of the interlayer cations.

Parks et al. [106] elaborately studied Xe^{44+} ion induced defects and the dependence of the defect size on the kinetic energy of the incident ions in a kinetic energy range of 0.1 - 20 keV/q. Via contact mode AFM measurements, protrusions with typical diameters of 20 nm and heights of 0.3 nm were observed, whereas no pronounced change in size was found for varying kinetic energies. Similar to the behaviour found in this work (see section 6.1.4), the researchers observed that, depending primarily on loading force and scan angle, the defects may appear either as hillocks or as pits in the AFM image when the scan direction is reversed (Fig. 63).
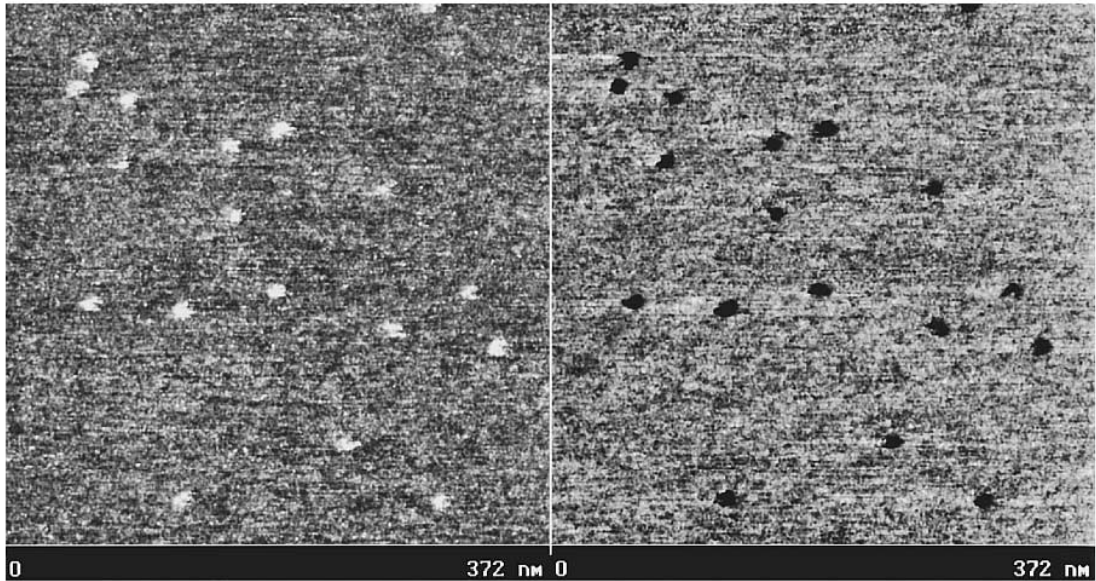
Figure 63: Defects created by Xe^{44+} ion bombardment appear as pits upon reversal of the scan direction in contact mode AFM [106].

As pits were also visible in tapping mode AFM imaging, where lateral forces are minimized, the authors propose that the pits are due to a true topographic modification and

that the contrast reversal seen in contact mode is a consequence of both topographical and frictional contributions. A study on the track formation induced by swift heavy ions on mica [107] found the same scan-angle dependent appearance of ion-induced structures. However, comparison of images recorded at different scan angles led to the conclusion that direction-dependent friction forces gave rise to artificial topographical features and that the observed contrast originated solely from friction. A detailed general discussion of the influence of lateral forces on the topography in scanning force microscopy may be found in ([108], [109]).

In a latter study [110] carried out by the same group, the potential energy dependence of the defect size was inspected. Xe^{q+} ($25 \leq q \leq 50$) ions, corresponding to potential energies of 8 - 100 keV, were extracted from two different EBIT type sources at constant kinetic energies of 100 keV.
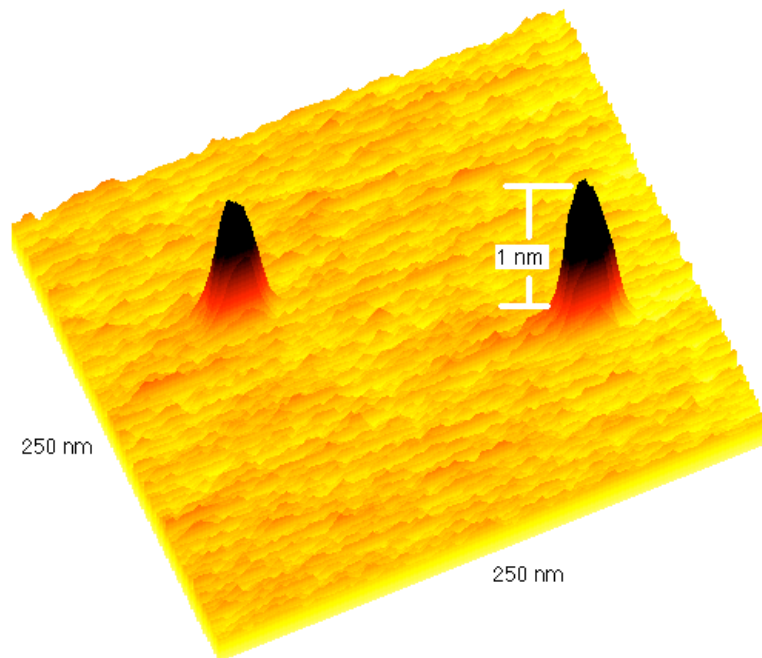
Figure 64: Atomic force microscope image of two Xe^{50+} ion impact sites on mica [110].

AFM investigations were performed with the lowest stable loading forces in order to avoid or minimize the "peeling off" of found protrusions through the scanning process, which had been observed in some of the earlier studies. Beginning at q = 30 (corresponding to the predicted threshold in [105]), hillocks were found for all charge states and their height, diameter and volume evaluated. All quantities undergo a clear increase with rising charge state.

77

The researchers assumed that hillock creation is closely related to the layered structure of mica. Adjacent sheets may be easily forced apart by coulomb repulsion due to the rapid removal of electrons in the surface near region. Locally this may be seen as a protrusion. This interpretation is also consistent with the observation that the hillocks were not stable over time but often disapeared after continuous scanning over the same area.
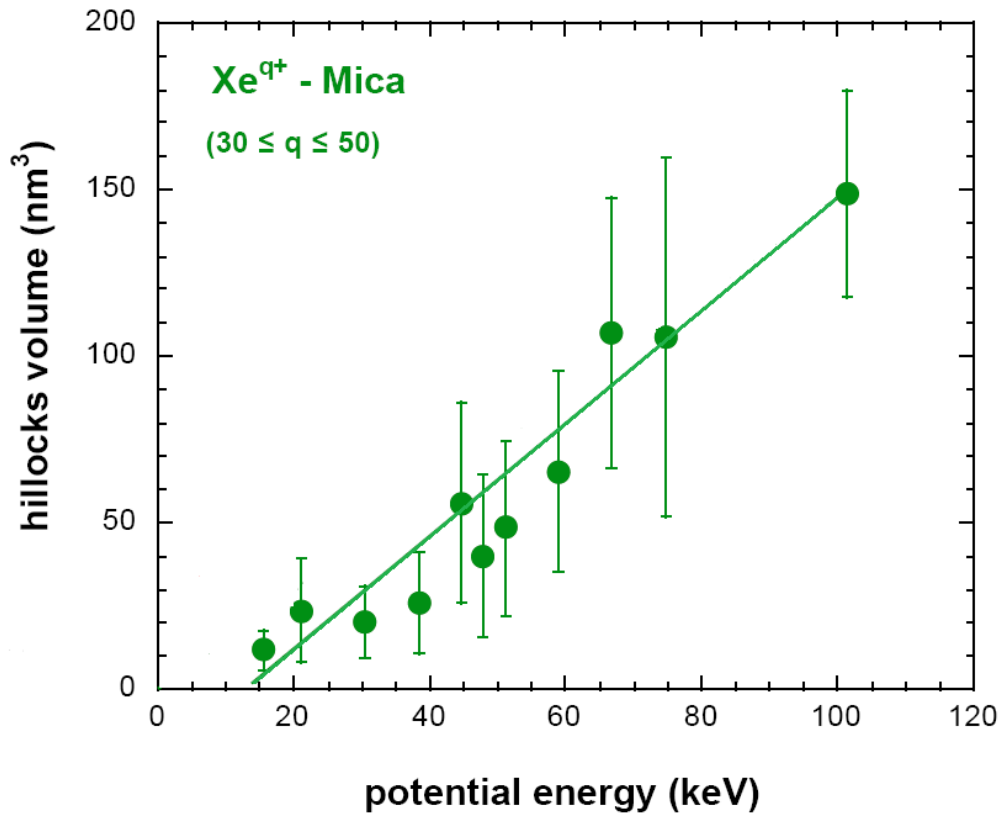
A summary of the data up to date is given in Fig. 65.

Figure 65: Mean hillock volume as a function of potential energy [2]. Data taken from [35] and [110].

6 Experimental results

6.1 Hillock formation

6.1.1 CaF$_2$

The observations described in section 5.1 not only give some answers on the principles of hillock formation on CaF$_2$, but also raise new questions: What is the exact position of the potential energy threshold? How do lower kinetic energies or higher charge states influence the results, what changes under grazing incidence?

In order to find some answers, in the course of this thesis a further series of irradiations was performed at the two-source-facility, located in the ion beam center of Forschungszentrum Dresden-Rossendorf (see section 4.1). The facility employs an EBIT source combined with a deceleration system, allowing for experiments with final ion kinetic energies as low as 5 V times charge state.

Isotope-pure ^{129}Xe^{q+} ions were extracted and decelerated before impact on the CaF$_2$ surface under normal incidence. The time-averaged beam flux varied between 10^4 and 10^6 ions/s. After exposure to fluences of about 10^{10} ions/cm^2 the crystal was transferred to an UHV-AFM/STM (Omicron) and inspected with contact mode AFM.
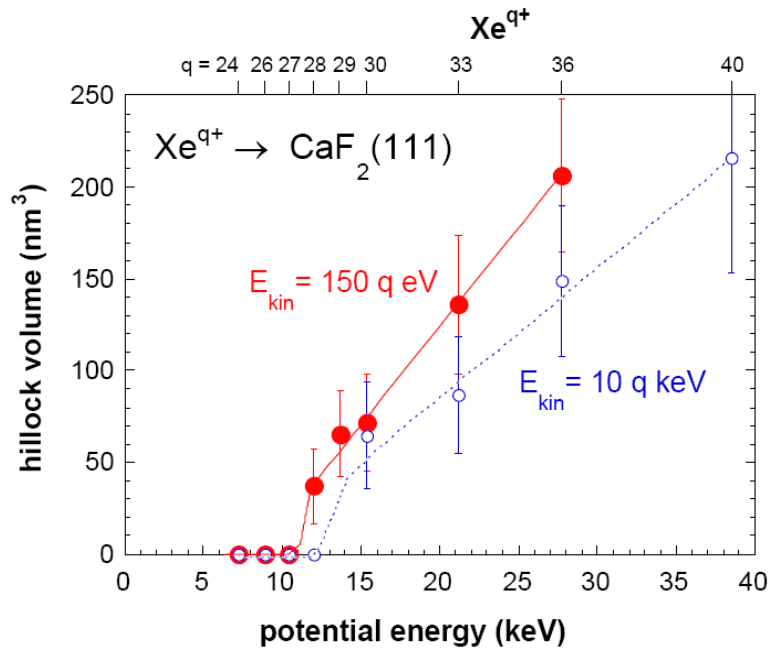
Figure 66: Mean hillock volume as a function of potential energy for two different kinetic energies [111].

The AFM images were evaluated with respect to diameter, height and efficiency in defect creation (i.e. number of hillocks per unit area/incoming ions per unit area).

To investigate the potential energy dependence, charge states were varied from q = 24 – 36 while maintaining a constant potential difference of 150 V between ion source and target surface, resulting in final impact energies of only 28 – 42 eV/amu. Surprisingly enough, hillocks were also found on the samples exposed to Xe^{28+} irradiation although no structures had been seen in the 10 kV x q series. As can be seen in Fig. 66, the threshold shifts by about 2 keV and furthermore the mean hillock volume seems to slightly increase with decreasing kinetic energy. Measurements were repeated to rule out errors in either the irradiation or the microscopy procedure and confirmed that hillocks are produced by slow (150 q eV) Xe^{28+} but not by faster (10 q keV) Xe^{28+} projectiles.

After further reducing the impact energy to the lowest stable value of 15 q eV, a further shift of the threshold was observed as structures protruded from Xe^{26+} and Xe^{27+} irradiated samples.
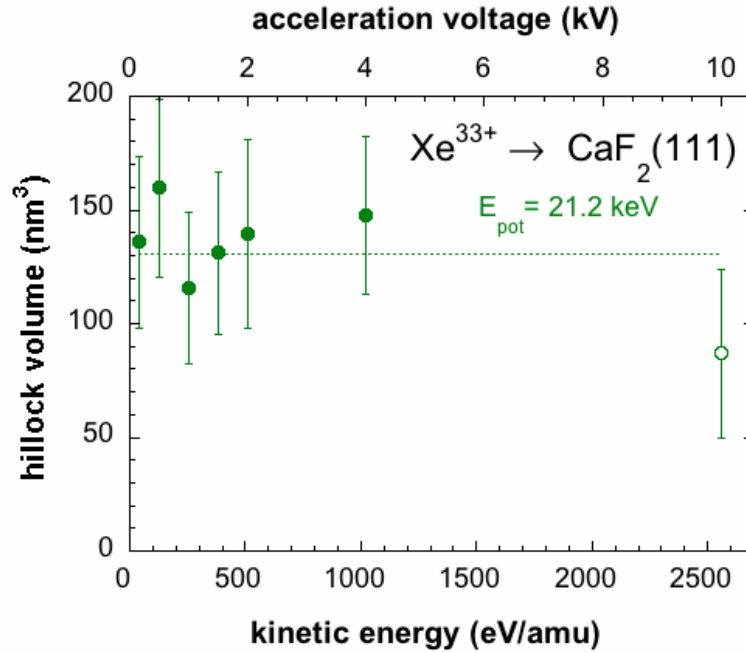
Figure 67: Mean hillock volume as a function of kinetic energy [111]

In a second series the charge state (Xe^{33+}) was kept constant and the acceleration voltage varied from 4000 down to 150 V to demonstrate that deposition of the potential rather than the kinetic energy is the crucial process in hillock formation.

Fig. 67 shows the kinetic energy dependence of the mean hillock volume. Reduction of the kinetic energy by nearly two orders of magnitude has practically no influence on the measured hillock volume. Comparison with previous results (open symbol in Fig. 67) even indicates a trend towards volume increase with lower kinetic energies. The hillock volume is calculated from diameter and height assuming the cap of a sphere (Fig. 68).
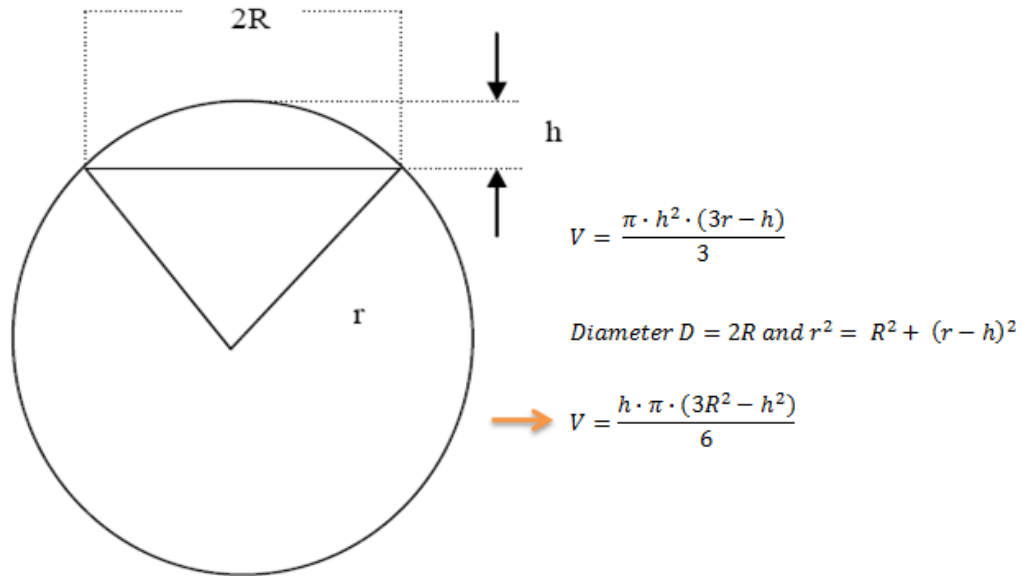

$$V = \frac{\pi \cdot h^2 \cdot (3r - h)}{3}$$

$$Diameter\ D = 2R \ and \ r^2 = R^2 + (r - h)^2$$

$$V = \frac{h \cdot \pi \cdot (3R^2 - h^2)}{6}$$

Figure 68: Calculation of the hillock volume.

To summarize the results, Table 2 gives an overview of the obtained data (and standard deviations of the mean values) for all charge states and irradiation parameters. The efficiency in defect creation is determined by comparing the found number of hillocks per unit area with the applied ion fluence.

q	D [10^9 cm^{-2}]	E_{pot} [keV]	U [V]	E_{kin} [keV]	Hillocks	d [nm]	Δd [nm]	h [Å]	Δh [Å]	Eff. [%]	ΔEff. [%]
Potential energy dependance											
24	10	7,263	150	3,60	no	0,0	0,0	0,0	0,0	0,0	0,0
26	15	8,937	150	3,90	no	0,0	0,0	0,0	0,0	0,0	0,0
27	15	10,431	150	4,05	no	0,0	0,0	0,0	0,0	0,0	0,0
28	10	12,000	150	4,20	yes	22,0	3,5	3,2	0,7	12,3	3,8
30	10	15,397	150	4,50	yes	22,6	3,0	4,1	0,8	13,7	2,2
33	10	21,165	150	4,95	yes	25,3	2,5	4,4	1,0	20,0	4,1
36	10/20	27,787	150	5,40	yes	25,1	2,2	6,9	1,5	18,0	2,4
39	5	35,707	150	5,85	yes	xxx	xxx	xxx	xxx	xxx	xxx
Kinetic energy dependance											
33	8/9	21,165	500	16,50	yes	25,6	2,3	6,2	1,0	20,2	5,8
33	10	21,165	1000	33,00	yes	26,8	2,3	4,1	0,8	24,8	2,1
33	10	21,165	1500	49,50	yes	26,1	2,2	4,9	0,9	70,5	7,0
33	9	21,165	2000	66,00	yes	21,2	1,6	7,9	1,6	75,8	4,6
33	13	21,165	4000	122,00	yes	24,4	1,9	6,3	0,9	96,5	2,1
Measurements at lowest impact energies											
25	45	8,081	15	0,38	no	0,0	0,0	0,0	0,0	0,0	0,0
26	20	8,937	15	0,39	yes	19,9	1,2	4,7	0,9	3,8	0,3
27	20	10,431	15	0,41	yes	22,2	1,5	5,8	0,9	3,4	0,5

Table 2: Summary of ion irradiation parameters, mean hillock dimensions (diameters (d) and heights (h)) and efficiencies (Eff.) in defect creation.

A selection of AFM micrographs is presented in Figs. 69 - 72.
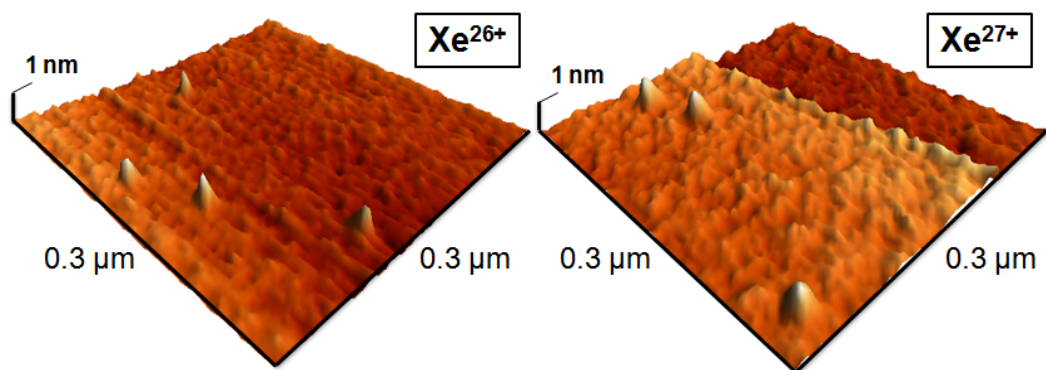
Figure 69: CaF$_2$ irradiated with different Xe charge states at kinetic energies of 15 q eV.
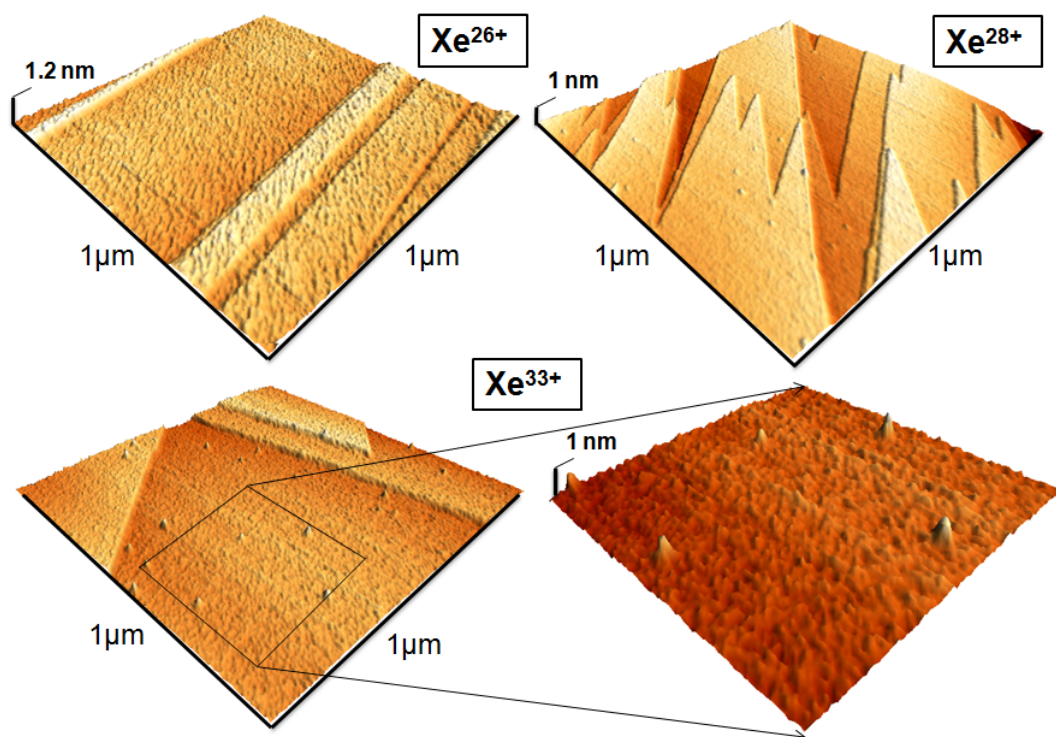
Figure 70: CaF$_2$ irradiated with different Xe charge states at kinetic energies of 150 q eV. Hillocks were found for charge states q $\geq$ 28. The structures in the top left image are not hillocks and are due to surface roughness.
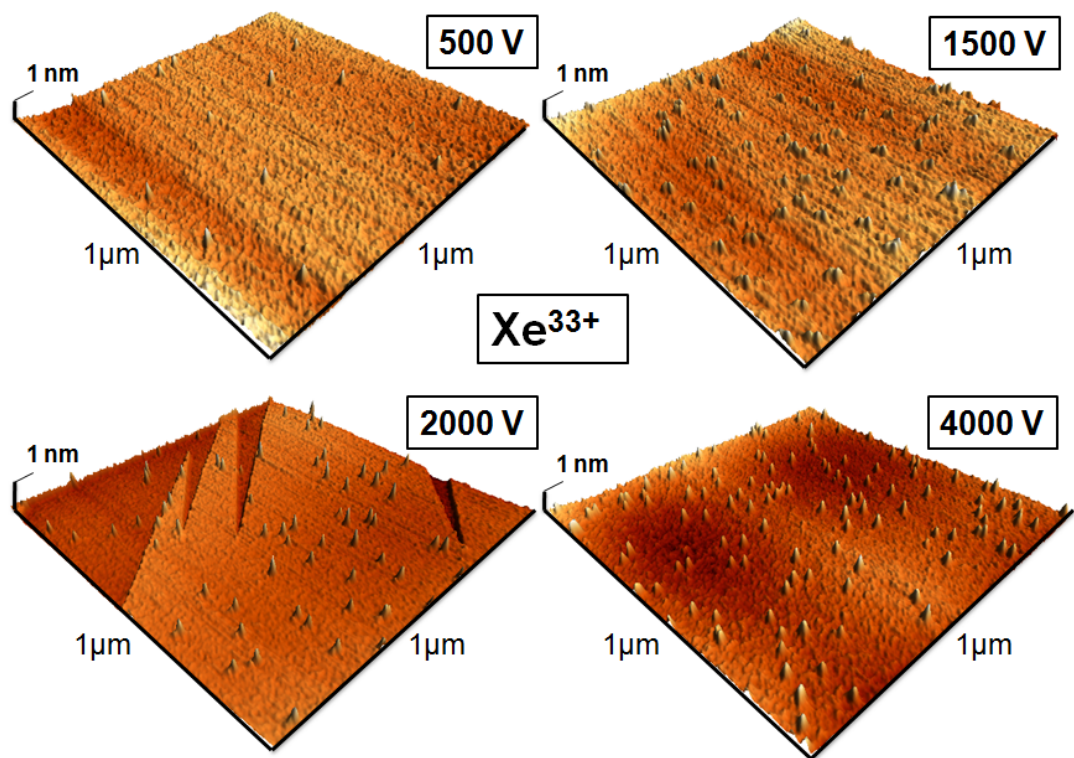
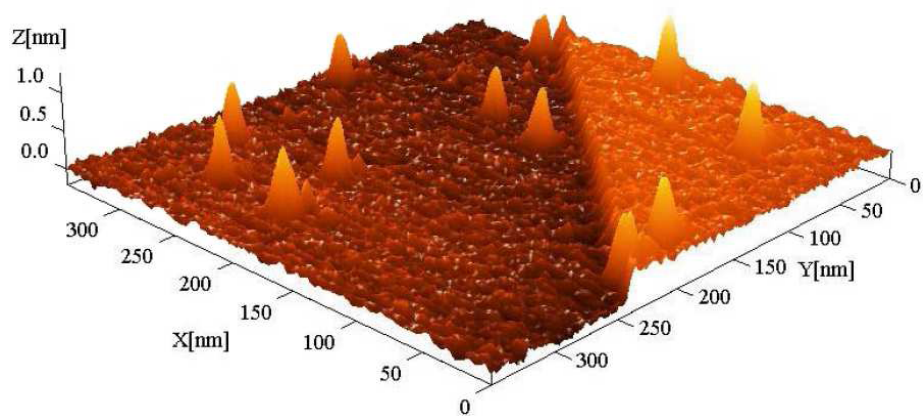Figure 71: CaF_2 irradiated with Xe^{33+} ions at different kinetic energies.

Figure 72: CaF_2 irradiated with Xe^{33+} ions at a kinetic energy of 2 q keV [111].

6.1.2   A first theoretical model for hillock formation on CaF_2

Introduction

As stated in the previous sections, the emergence of the observed thresholds in ion-induced hillock formation can be linked to phase transitions (melting and sublimation). The following model ([111], [112]) describes the hillock formation as a consequence of potential energy carried into the collision by the HCI and the subsequent heating of the crystal by electron–phonon coupling.

Starting point of the model is the so-called thermal-spike model originally developed for swift heavy ions ([113], [114]). Therein track formation is associated with local heating above the melting temperature.

In the case of slow HCI, however, energy deposition proceeds markedly different, as they solely deposit potential energy and penetrate the solid only a few atomic layers (c.f. chapter 2).

This can also be described in terms of different primary electron distributions, the starting point of the thermal spike, generated by a swift heavy ion and a slow HCI. As opposed to the kinetic energy of swift heavy ions, only a fraction of the total potential energy of slow HCI is responsible for the increase of energy density in the impact region. A significant fraction of the potential energy is stored in deep inner shell vacancies of the projectiles, which may either decay radiatively or by emission of fast ($\sim$ keV) electrons. In the former case, the energy is effectively lost for heating, while the heating efficiency is significantly reduced in the latter. Due to the small penetration depth of the slow HCI, high energy electrons are likely (probability up to 50%) to escape into vacuum and their energy is lost for crystal heating.

The situation can be described nicely if one compares the scenarios e.g. for Ar^{17+} and Ar^{18+} ions. The difference between these two charge states with respect to their potential energy comes mainly from the additional inner shell vacancy, resulting in the emission of one additional K-Auger-electron in the neutralization sequence of an Ar^{18+} ion (Fig. 73). Consequently, one half of all Ar^{18+} ions will deposit a similar amount of energy as Ar^{17+}, 25% of Ar^{18+} ions even much less (a single K-Auger electron has an energy of 3 - 4 keV). Despite these numbers, hillocks are only observed on Ar^{18+} irradiated samples with close to 100% efficiency.

• both electrons stay in target

$\sim E_{pot}$ **of Ar^{18+}**

25% probability

• one electron emitted to vacuum

$\sim E_{pot}$ **of Ar^{17+}**

50% probability

• both electrons emitted to vacuum

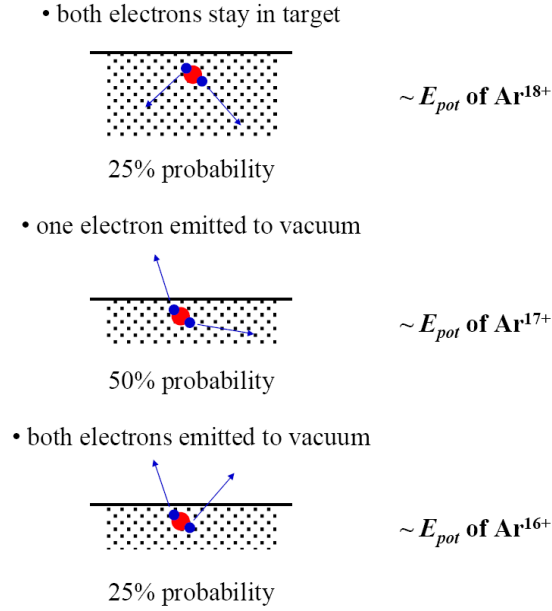$\sim E_{pot}$ **of Ar^{16+}**

25% probability

Figure 73: Possible scenarios for the energy deposition of an Ar^{18+} ion [115].

Contrary to naive expectations, the decisive difference between below and above threshold charge states is not the additional fast Auger electron but the many additional slow electrons emitted along the deexcitation sequence resulting from the filling of the additional core hole, as will be explained in the following.

Excitation of the electronic system

Upon impact on solid surfaces, highly charged ions undergo a large number of neutralization and deexcitation processes (see chapter 2). The projectiles reach the surface far from ground state and a large fraction is still highly charged. The ongoing deexcitation sequence after entering the target material involves states below or in resonance with the insulators valence band.

Simulations of the neutralization sequence in ([111], [112]) are based on the classical over the barrier model [25] and its extension for insulator surfaces ([26], [27]). Two processes are taken into account: Deexcitation processes (radiative and Auger decay) as a consequence of classically allowed electron transfers into excited states and Auger capture processes. In the latter case, both interacting electrons originate from the target valence band, one of them populating an inner shell of the projectile and the other carrying the excess kinetic energy.

Electron transport simulation and heating efficiency

In the simulation, primary electrons created in the in course of the neutralization of the HCI are followed and their transport through the medium is approximated as a classical zig-zag trajectory. Elastic and inelastic scattering processes are taken into account and lead to the creation of secondary electrons which are as well followed along their subsequent trajectories. Energy transfer to the lattice (excitation of phonons) through elastic scattering of electrons on target nuclei will eventually lead to heating and melting of the crystal.

The simulation shows that the heating efficiency (number of excited phonons) of the primary electrons depends on deposited energy density rather than the total deposited energy. As low energy electrons undergo a large number of elastic scattering events, expressed by the lower elastic mean free path in the low energy region in Fig. 74a, they excite a large number of photons within in a small volume and efficiently contribute to the heating of the crystal. High energy electrons (inner shell Auger electrons), on the other hand, travel more than an order of magnitude farther before interaction with the target material sets in. The resulting energy density close to the point of their emission will thus be small as compared to the case of low energy electrons (Fig. 74b). If we return to the cases of Ar^{17+} (below threshold) and Ar^{18+}, the difference in energy
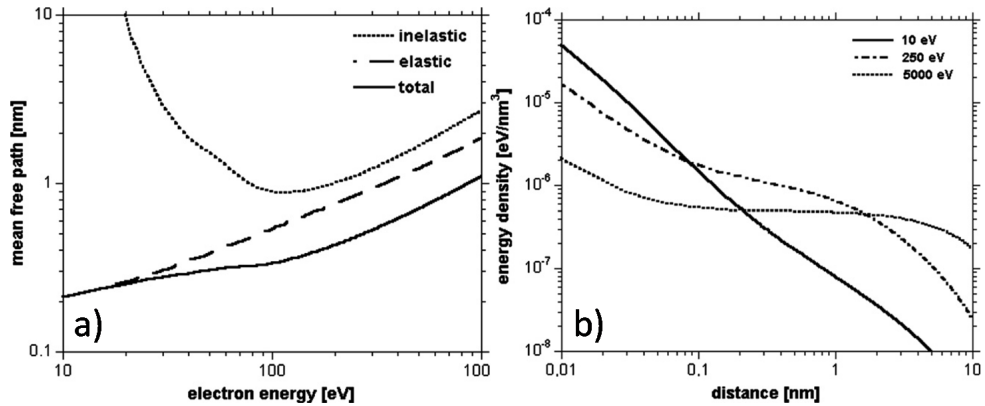
Figure 74: a) Inelastic, elastic and total mean free paths in CaF_2 as a function of electron energy, b) Deposited energy density for different primary electron energies as a function of distance from point of emission [112].

deposition and therefore heating efficiency can be assigned to ~ 3 more low to mid energy electrons emitted per projectile with the threshold charge state.

Fig. 75 illustrates the shape dependence of the volume where electronic energy is effectively converted into lattice heating on the velocity and the charge state of the projectiles (taken from [111]): If either the velocity is increased or the potential energy reduced (smaller initial charge states) the diameter of the heated volume shrinks [111].

Although the present simulation assumes a structureless medium, neglecting possible effects of the crystalline structure, it nevertheless provides important information on the spatial distribution of energy deposition: The volume in which the required energy density for melting (0.55 eV/atom) is reached ("hot core" indicated in yellow in Fig. 75) amounts about 2.5 nm^3 or 15 unit cells of CaF_2 for Xe^{28+} ions with 150 q eV kinetic energy. The linear dimension of the hot core is equally important to retain the required energy density for a sufficient period of time. To initiate restructurization before cooling sets in, the diameter of the core should exceed the size of a unit cell. For smaller values (Fig. 75c), energy is apparently dissipated too quickly for melting and subsequent hillock formation to set in.
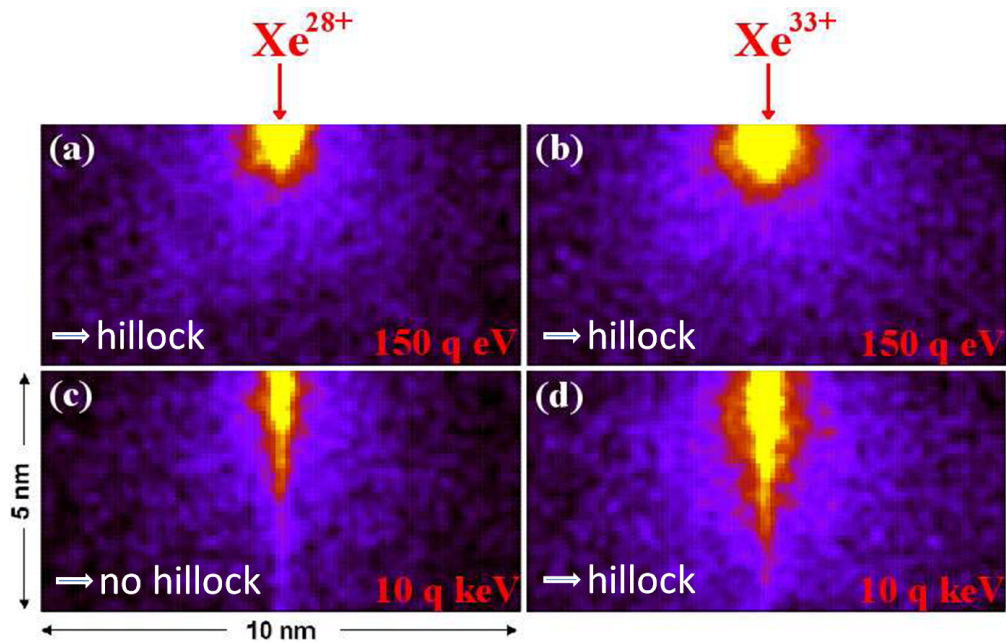
Figure 75: Calculated energy depositions for Xe^{28+} and Xe^{33+} ions in CaF_2 with kinetic energies of 150 q eV and 10 q keV, respectively. Image taken from [111].

6.1.3   HOPG

Although the hillock formation on HOPG has been extensively studied via STM, the found structures, with the exception of two cases (see section 5.2), were never seen with AFM. Aim of the present study was to obtain AFM data on hillock formation and possible emergence of thresholds and as a result gain more insight on the mechanism of energy deposition which, due to the lamellar structure, should be markedly different than for e.g. ionic crystals.

Experiments were carried out at GANIL (Grand Accélérateur National d'Ions Lourds) in Caen, France. Xe^{q+} (q = 23 and 27) and Ar^{q+} (q = 9, 12, 14 and 16) ions were extracted from an 14.5 GHz ECRIS (see section 4.1) and accelerated onto the samples under normal incidence to final impact energies of 150 - 216 keV.

For every desired charge state, four (two HOPG and two mica) samples were fixed on a target holder and mounted in the target chamber at pressures of $\sim 10^{-7}$ mbar. Time averaged beam fluxes of 10^9 - 10^{10} ions/s and irradiation times of 20 seconds up to 10 minutes resulted in total ion fluences of 10^{11} - 6 x 10^{11} ions/cm^2. For each charge state, two different fluences were applied By counting the number of defects per unit area and comparing with the respective fluence, the defects could be clearly ascribed to ion bombardment. Irradiated samples were immediately investigated with a Nanoscope III (Digital Instruments, Santa Barbara, USA) AFM in constant force contact mode.
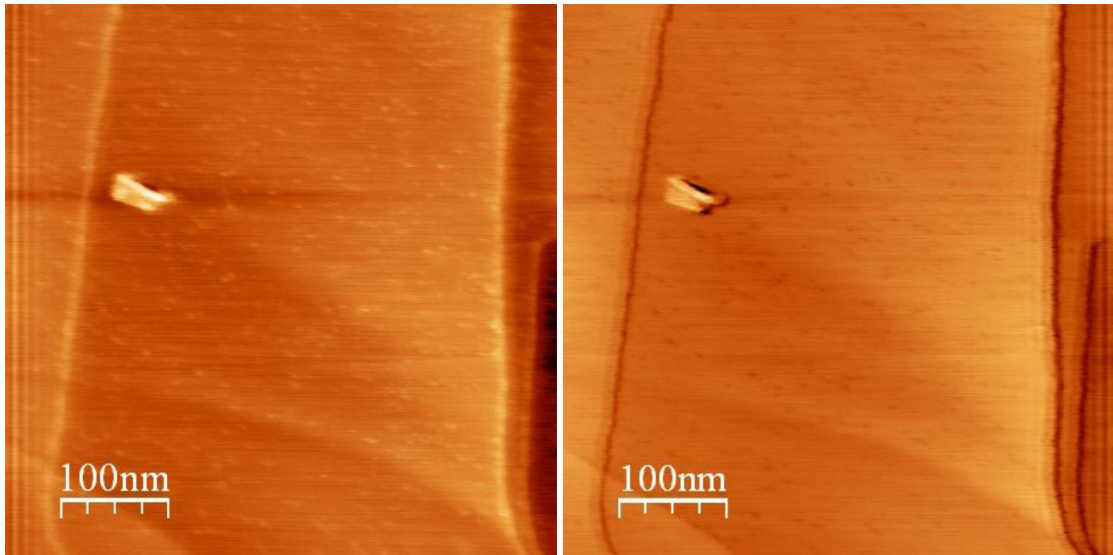
Figure 76: Height trace (left) and retrace (right) on HOPG irradiated with Ar^{9+} ions (E_{kin} = 180 keV) at a total ion dose of 6 x 10^{11} ions/cm^2.
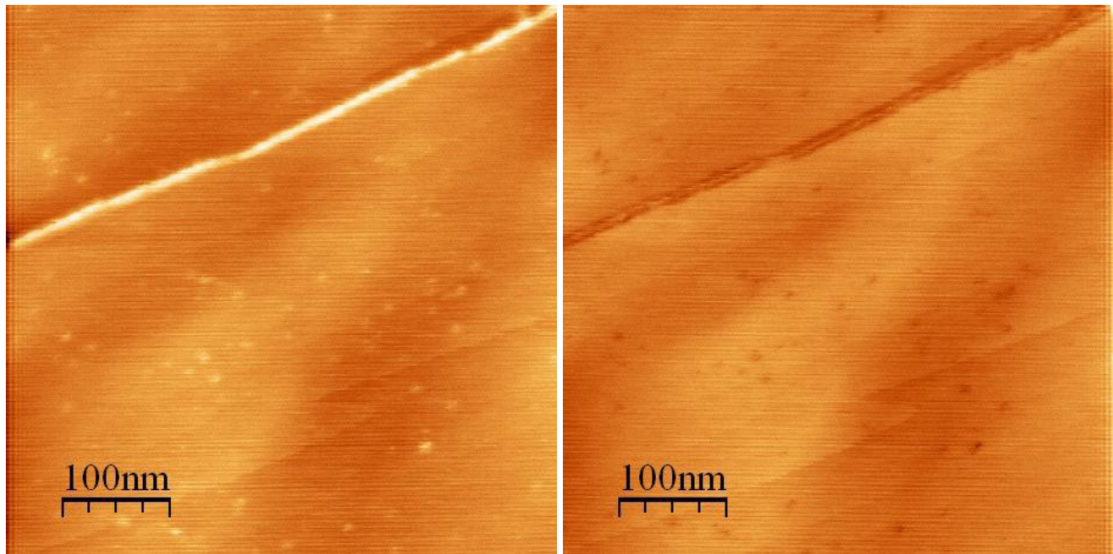
Figure 77: Height trace (left) and retrace (right) on HOPG irradiated with Ar^{9+} ions (E_{kin} = 180 keV) at a total ion dose of 2 x 10^{11} ions/cm^2.
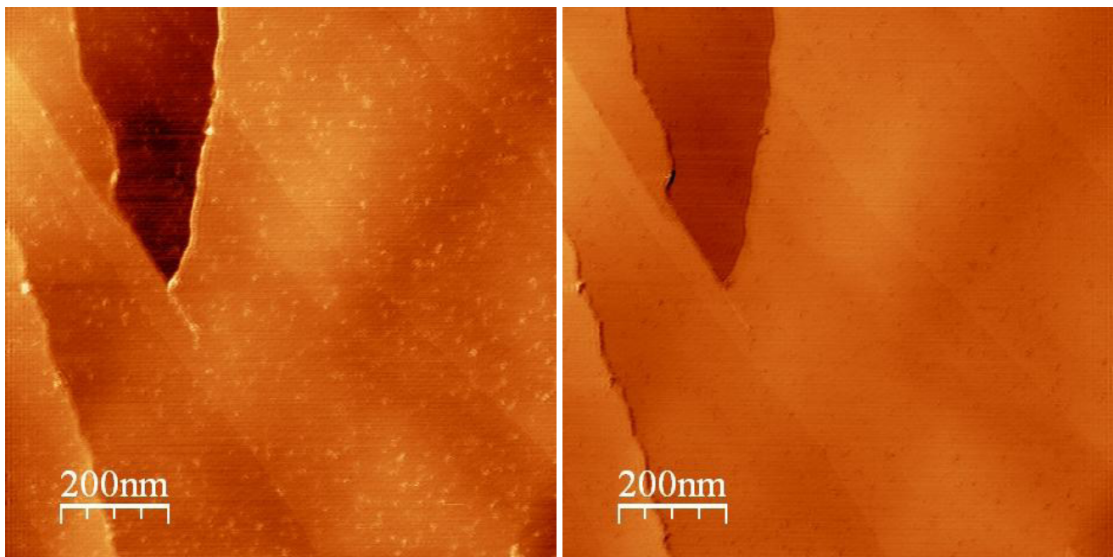
Figure 78: Height trace (left) and retrace (right) on HOPG irradiated with Xe^{23+} ions (E_{kin} = 180 keV).

Quite surprisingly, structures were found for all investigated charge states. However the scanning process revealed great differences compared to the hillocks as seen e.g. on CaF_2. Contrast formation in the respective scanning directions was found to be heavily dependent on changes of the scan angle: Features could appear as protrusions in the forward scan and as pits in the back scan (Figs. 76 - 78) or show similar appearances in both scanning directions.

In any case, the strongest signal was found in the lateral force trace in which the lateral torsion of the cantilever is recorded. It has been long known that lateral forces which are mostly due to friction can give rise to topographic artifacts. This effect is especially pronounced if light beam deflection is used to sense the motion of the cantilever (as in these studies) and is a consequence of measuring the bending angle of the cantilever rather than the deflection itself ([108], [109]).

In the constant force mode the loading force then not only arises from perpendicular forces but also has a contribution from the lateral forces. Hence, variations of the lateral force may cause the feedback loop to respond and the resulting apparent changes in height add to the true topography and depend heavily on the scan angle. These apparent height changes are not necessarily small compared with the height of typical topographic features and can even be the dominant (pseudo)topographic contribution on very flat surfaces.
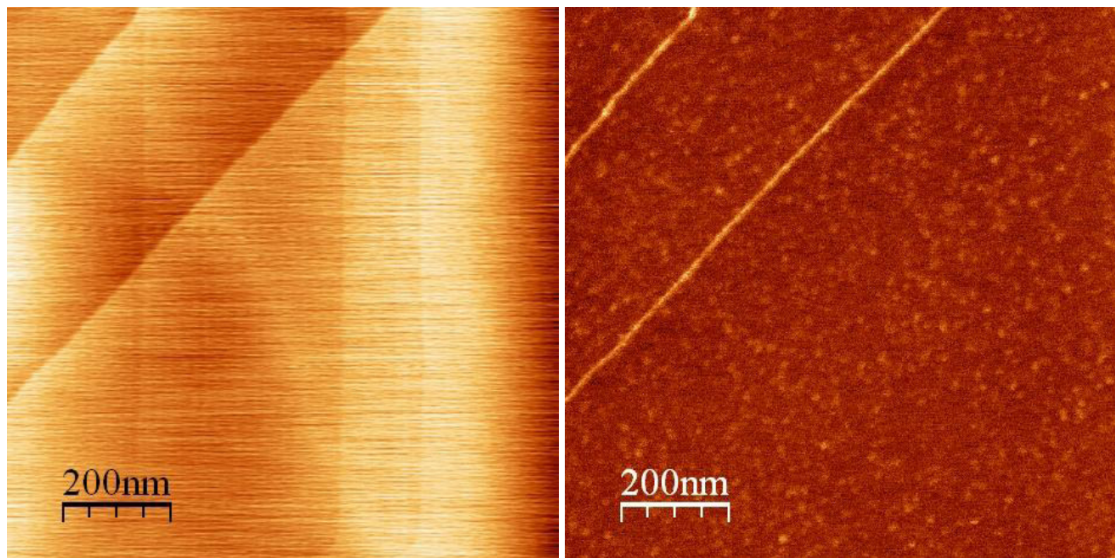
Figure 79: Height trace (left) and corresponding lateral force trace (right) on HOPG irradiated with Ar^{14+} ions (E_{kin} = 150 keV).
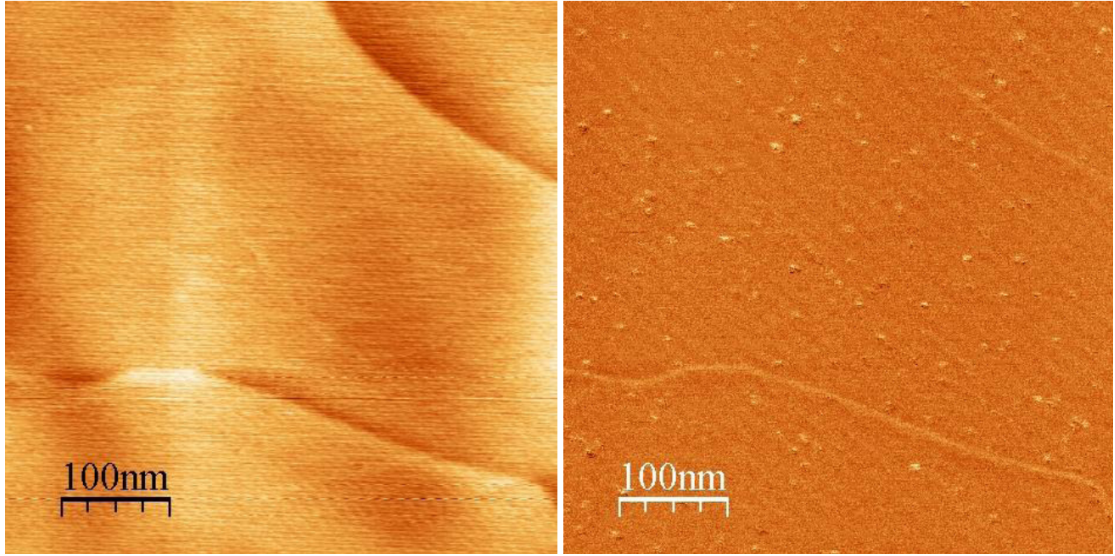
Figure 80: Height trace (left) and corresponding lateral force trace (right) on HOPG irradiated with Xe^{27+} ions (E_{kin} = 216 keV).

Repeated studies with the AFM at the TU Wien (Asylum Research MFP-3D) reveal smooth surfaces with occasional steps resulting from cleavage and hillock-like structures, very similar in diameter as found in the former measurements, were only found in the lateral force traces, independent of the scan angle (Figs. 79 and 80).

From the experimental data, it has to be concluded that the resulting features do not represent a real topographic modification of the surface but rather regions of enhanced friction. This effect, however, can be unambiguously identified as a result of the ion bombardment (e.g. Fig. 76 shows a much higher density of defects than Fig. 77 accordingly to the triple ion dose).

The fact that the mean defect diameters evaluated for all charge states remain nearly constant (see trendline in Fig. 81) and that the values are considerably larger ($\sim$ 10 nm) than in STM studies (typically below 5 nm in the investigated potential energy regime) points to an influence of the tip dimensions on the measurements. The efficiency in defect creation seems to increase with increasing potential energy (Fig. 81). Determination of total ion doses and efficiency is, however, afflicted with a variety of uncertainties, e.g. a beam flux strongly varying within a short irradiation time.

Table 3 gives a summary of irradiation parameters, diameters and efficiencies in defect creation (and standard deviations of the mean values) for the investigated charge states.
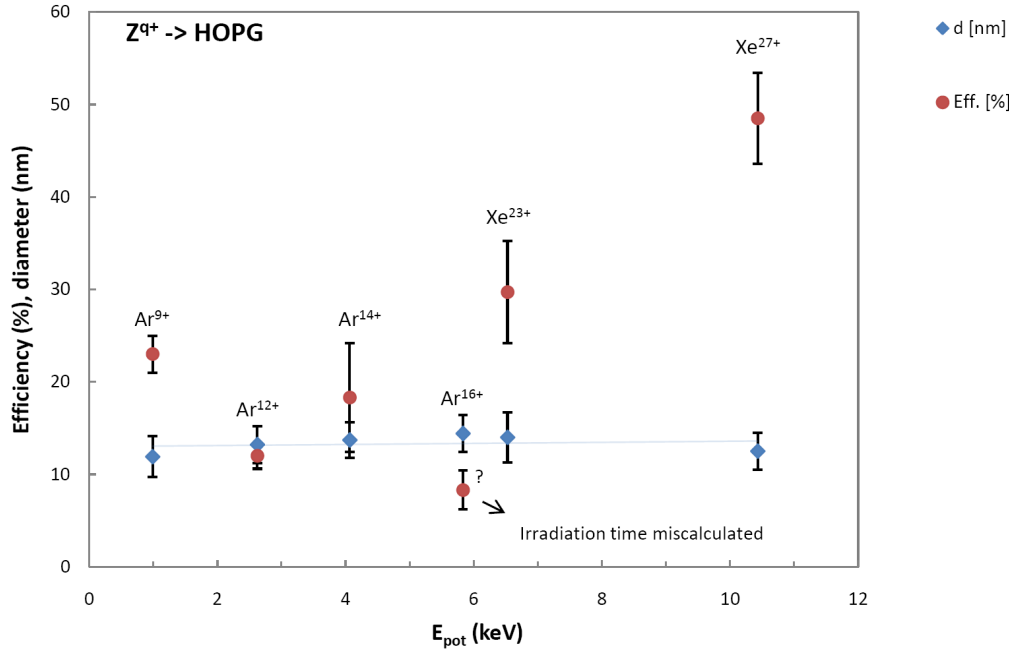
Figure 81: Mean defect diameter and efficiency in defect creation as a function of potential energy.

q	D [10^{11} cm^{-2}]	E$_{pot}$ [keV]	E$_{kin}$ [keV]	Hillocks	d [nm]	Δd [nm]	Eff. [%]	ΔEff. [%]
Ar9+	2	0,988	180,00	yes	11,9	2,2	23,0	2,0
Ar12+	2	2,623	180,00	yes	13,2	2,0	12,0	1,4
Ar14+	6	4,07	150,00	yes	13,7	1,9	18,3	5,9
Ar16+	6	5,83	150,00	yes	14,4	2,0	8,3	2,1
Xe23+	3	6,527	180,00	yes	14,0	2,7	29,7	5,5
Xe27+	1	10,431	216,00	yes	12,5	2,0	48,5	4,9

Table 3: Summary of ion irradiation parameters, mean defect diameters (d) and efficiencies (Eff.) in defect creation for all investigated charge states.

STM investigation

First preliminary results from STM investigations of the HOPG samples irradiated at
GANIL as described in the previous paragraph became available in the final stages of
this work. A rough statistical evaluation of the diameters of the found hillocks for three
charge states (Ar^{9+}, Ar^{14+} and Xe^{23+}) seems to be in good agreement with the literature
(Fig. 82). Additionally, the number of defects per unit area as seen with the STM seems
to be in better agreement with the applied ion dose than the values obtained in the AFM
measurements.
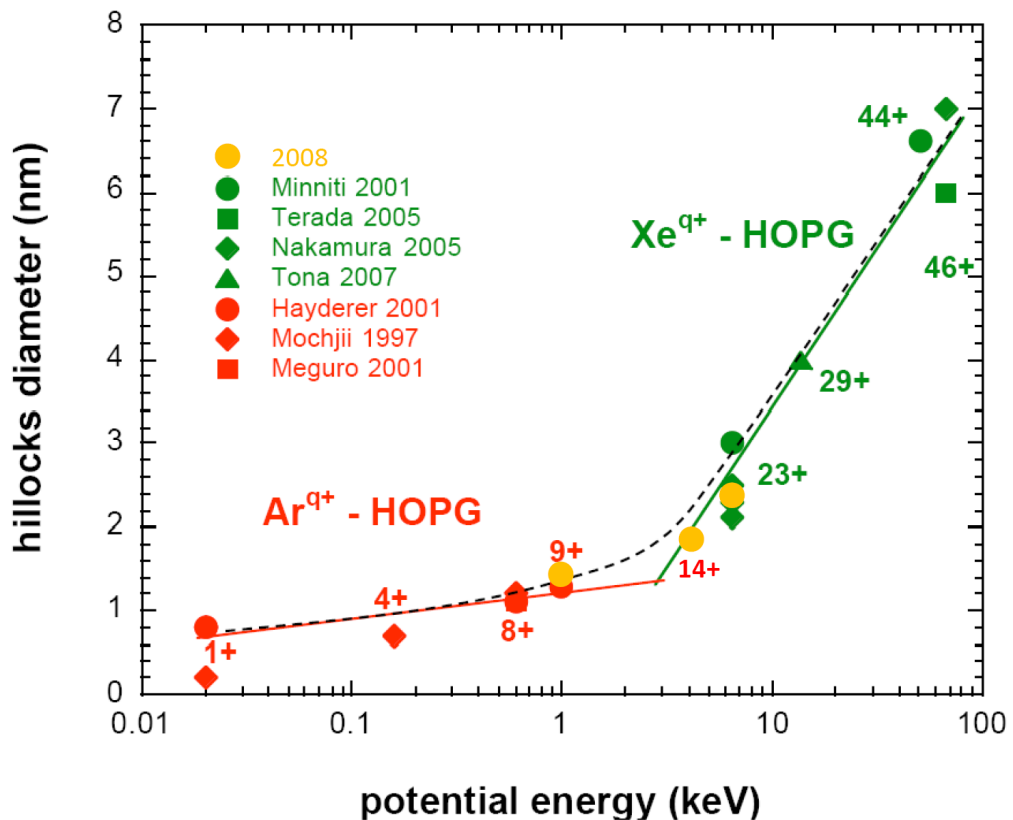
Figure 82: Mean hillock diameter as a function of potential energy: Picture reproduced
from section 5.2 with three new data points (orange).

The following images were recorded with an Omicron UHV-STM in constant current
mode with a typical setpoint current of 0.3 nA and a gap voltage of 0.7 V.
The shape of the defect in Fig. 85 is not typical, it is possibly the result of multiple ion
impact, and was observed only once.
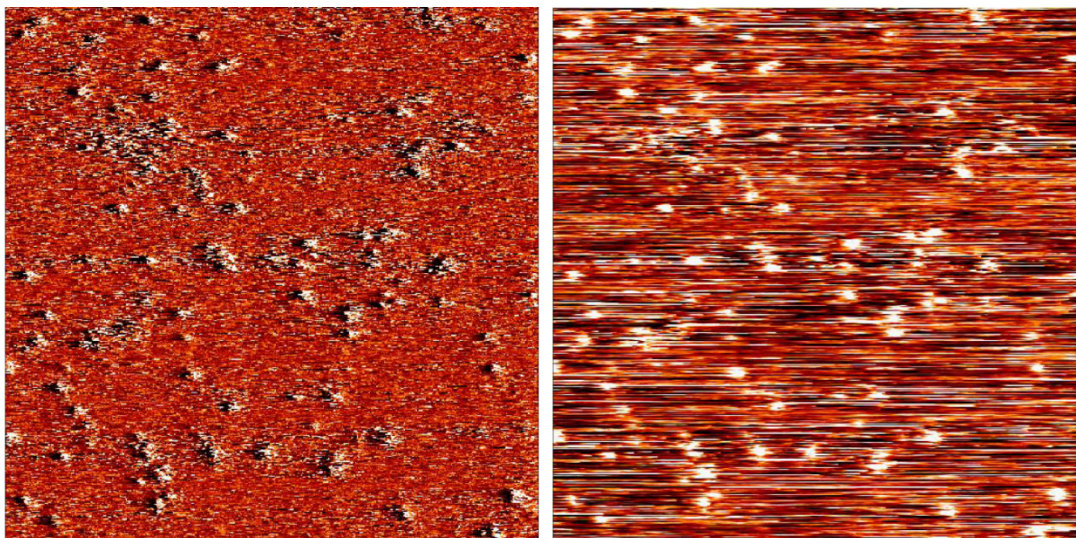
Figure 83: Current (left) and height image (right) of Ar^{9+} ion ($E_{kin} = 180$ keV) induced defects on HOPG, scansize: 100 nm x 100 nm.
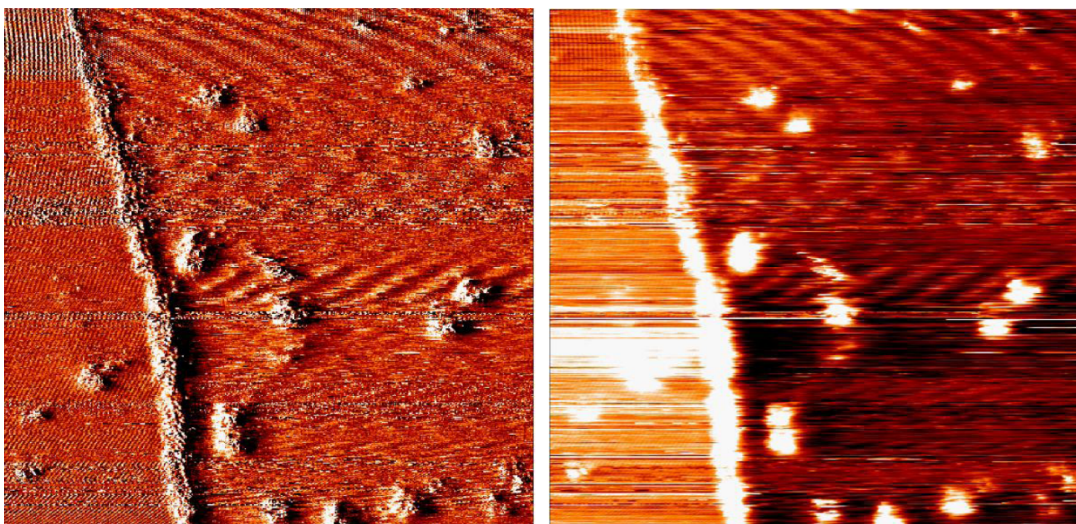
Figure 84: Current (left) and height image (right) of Xe^{23+} ion ($E_{kin} = 180$ keV) induced defects on HOPG, scansize: 50 nm x 50 nm.
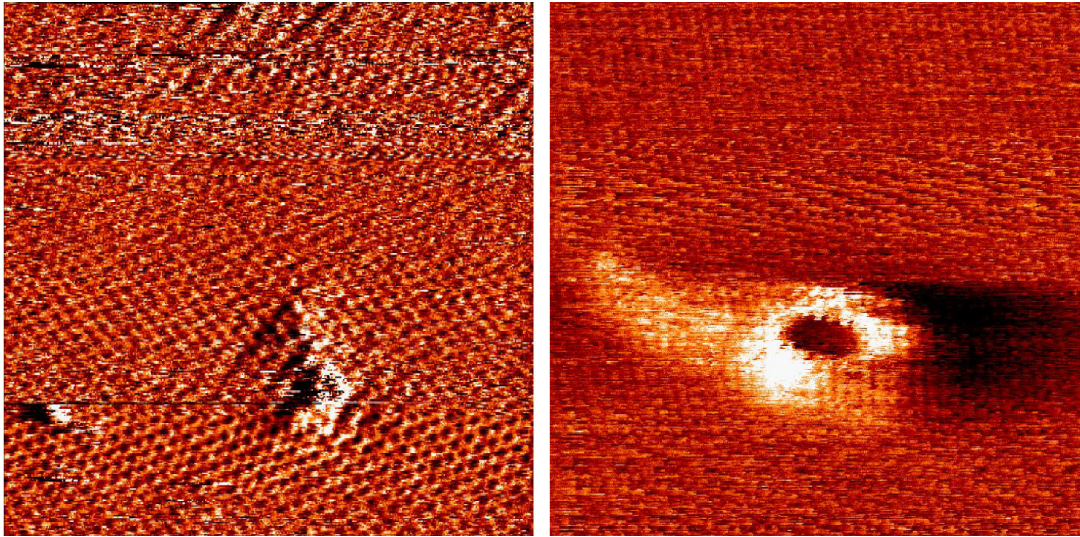
Figure 85: Current images of an Ar^{9+} ion (E_{kin} = 180 keV) impact site (left) and a peculiar defect produced by Ar^{14+} (right) ion (E_{kin} = 150 keV) bombardment, scansize: 10 nm x 10 nm.

6.1.4   Mica

Freshly cleaved mica samples were irradiated under the conditions described in the previous section and immediately investigated afterwards with contact mode AFM.

First measurements on samples irradiated with relatively high Ar charge states (q = 12 and 16) showed flat surfaces and occasional occurrence of topographic features which were caused by surface contamination (Figs. 86 and 87). The structures in Fig. 87 were originally ascribed to ion bombardment but after closer inspection (heights of the structures are > 3 nm, areal density is too small by a factor of 200) this possibility had to be ruled out.

For the investigated Xe charge states (q = 23 and 27), however, structures were found which could be clearly attributed to the ion bombardment after comparing the areal defect densities for two different ion doses (Fig. 88). The same scan angle dependent appearance of the features as reported for the HOPG samples and also in earlier literature on the hillock formation on mica [106] was found (Figs. 89 and 90) and repeated scanning sometimes resulted in a "peeling off" of the found features (Fig. 91).

Contrary to the findings in [106], tapping mode AFM imaging which was performed subsequently did not yield evidence of a topographic surface modification. Studies with the AFM at the TU Wien again supported the interpretation of the impact sites as regions of enhanced friction since structures were solely observed in the lateral force trace.
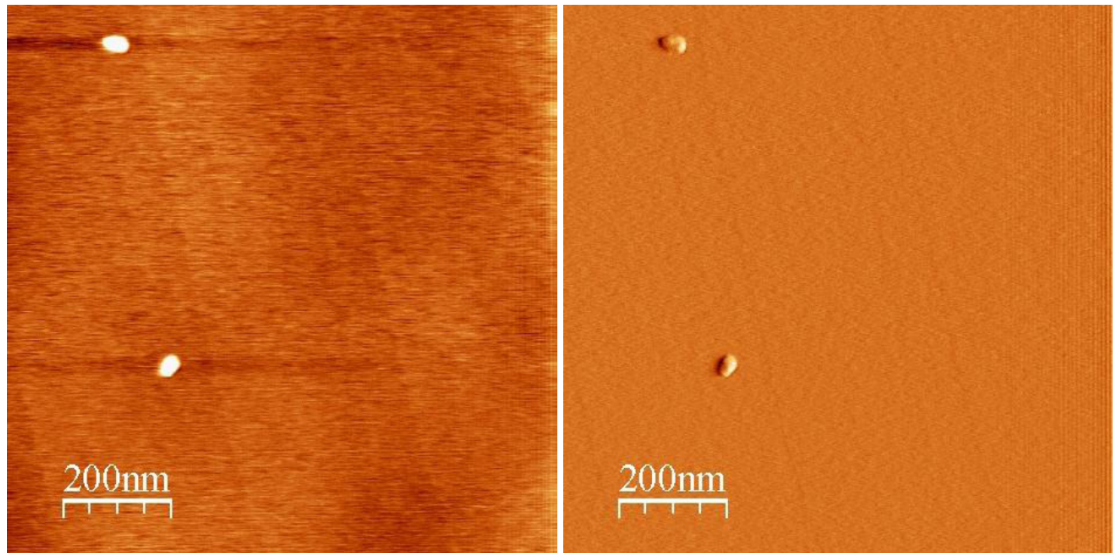
Figure 86: Height trace (left) and deflection trace (right) on mica irradiated with Ar^{12+} ions (E_{kin} = 180 keV).
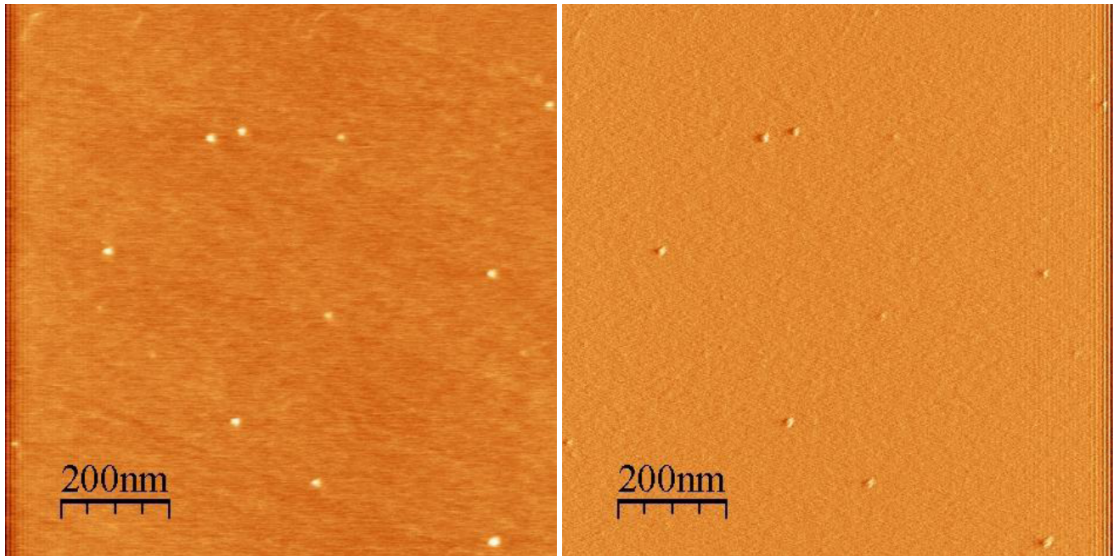
Figure 87: Height trace (left) and deflection trace (right) on mica irradiated with Ar^{16+} ions (E_{kin} = 150 keV).
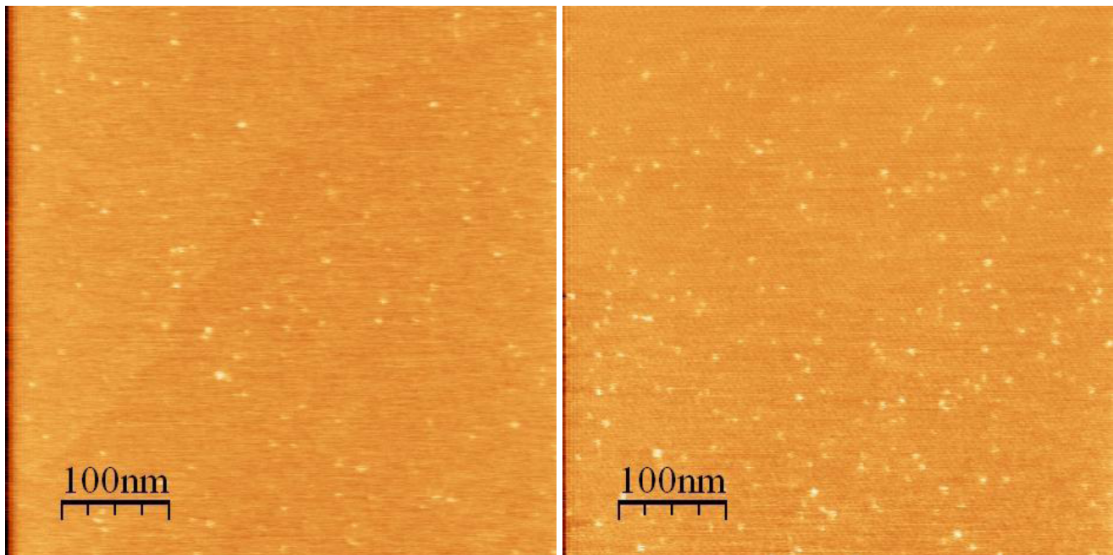

Figure 88: Height traces on mica irradiated with two different doses of Xe^{23+} ions (E_{kin} = 180 keV): 2 x 10^{11} ions/cm^2 (left) and 6 x 10^{11} ions/cm^2 (right).
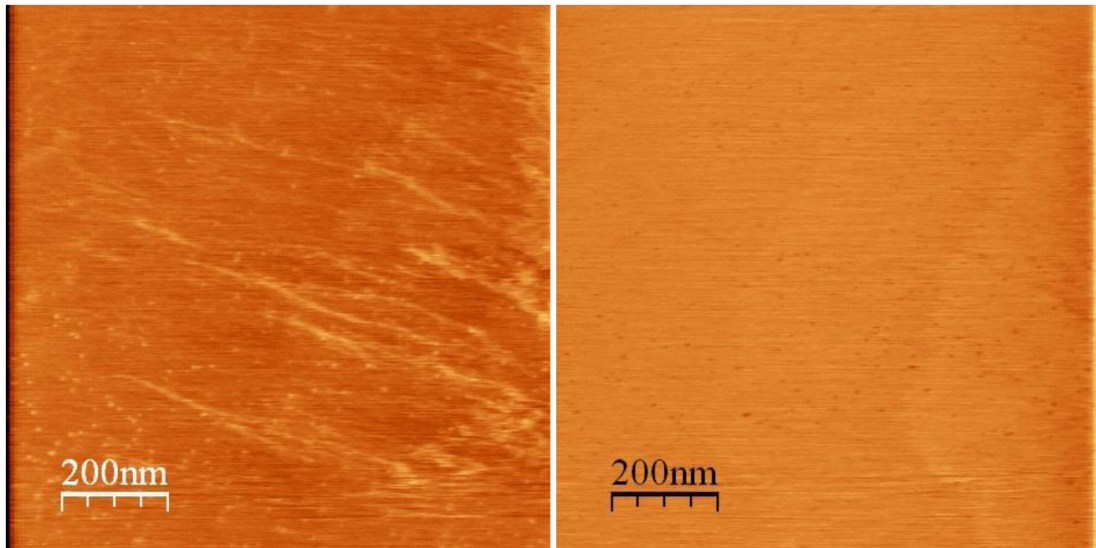
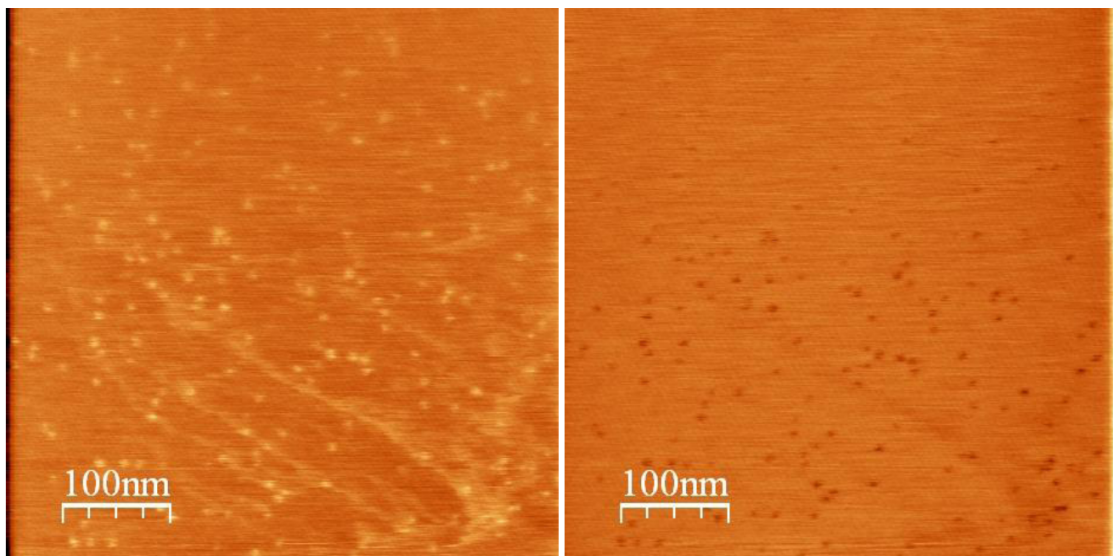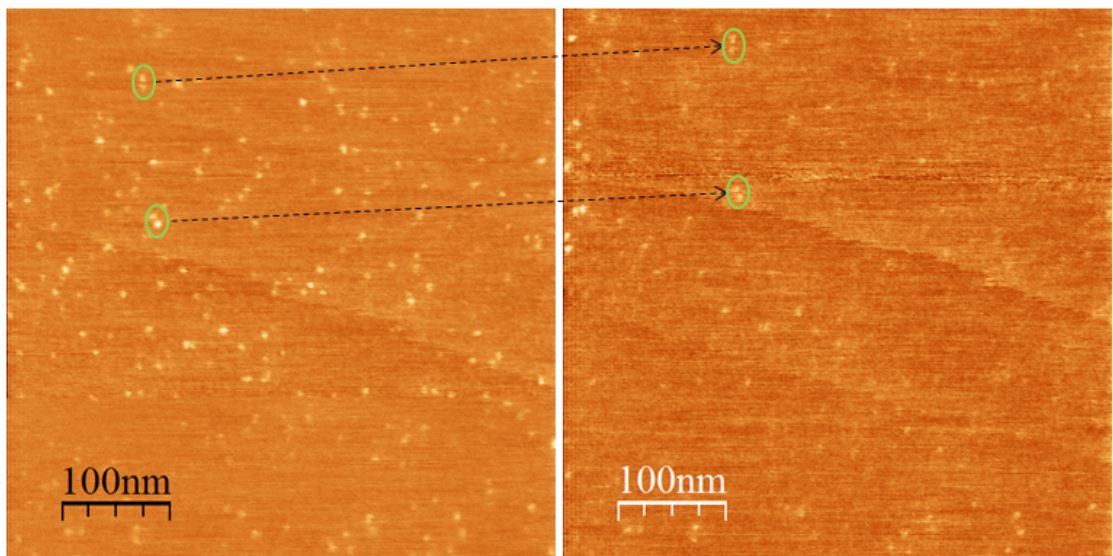Figure 89: Height trace (left) and retrace (right) on mica irradiated with Xe^{23+} ions ($E_{kin} = 180$ keV).

Figure 90: Height trace (left) and retrace (right) on mica irradiated with Xe^{27+} ions ($E_{kin} = 216$ keV).

Figure 91: First scan over an area of Xe^{23+} ($E_{kin} = 180$ keV) irradiated mica (left) and same area after 3 complete scans (right). Most of the defects are no longer or barely visible after continuous scanning. The slight change in position of the remaining features (e.g. in the green circles) is due to drift.

Whereas the discovered defects could not be identified as "hillocks" in the common sense, the results of this study are new and interesting nonetheless, as it was the first time that effects were observed on mica for charge states below q = 30.

Table 4 gives a summary of irradiation parameters, diameters and efficiencies in defect creation (and standard deviations of the mean values) for the investigated charge states. Although effects were found only for two charge states (Xe^{23+} and Xe^{27+}), the acquired data seem to indicate the same trend as for the HOPG series, i.e. constant diameters and a higher efficiency in defect creation with rising charge states.

For experiments in the future it is desirable to continue the Xe series down to lower charge states to search for a possible threshold and to perform more systematic investigations on the scan angle dependence.

q	D [10^{11} cm^{-2}]	E_{pot} [keV]	E_{kin} [keV]	Hillocks	d [nm]	Δd [nm]	Eff. [%]	ΔEff. [%]
Ar12+	1	2,623	180,00	no	0,0	0,0	0,0	0,0
Ar16+	4	5,83	150,00	no	0,0	0,0	0,0	0,0
Xe23+	2	6,527	180,00	yes	9,5	1,7	29,7	9,2
Xe27+	1	10,431	216,00	yes	12,9	1,9	58,3	10,4

Table 4: Summary of ion irradiation parameters, mean defect diameters (d) and efficiencies (Eff.) in defect creation for all investigated charge states.

6.2   MFM of ultrathin Fe films on Cu(100)

The following experiments were first approaches to utilize the ion-induced magnetic transformation, described in section 3.2, for magnetic patterning with ion beam lithography. The sample preparation can be divided into the following steps:

- Cleaning

  The substrate, a Cu(100) single crystal (disc-shaped, $\sim$ 8 mm diameter), is cleaned by sputtering with 500 eV Ar^+-ions.

- Annealing

  To regain a smooth surface after the sputtering process, the crystal is annealed via heating to 550 °C for about 30 minutes.

- Deposition

  The Fe films are grown at room temperature in ultra-high vacuum at a typical pressure of less than 2 x 10^{-10} mbar by thermal evaporation from a Fe wire heated by electron bombardment. The deposition rate is monitored with a quartz-crystal microbalance and is typically $\sim$ 1 ML per minute. The film thickness is subsequently checked by quantitative Auger spectroscopy.

- Capping layer

  To protect the film against oxidation in air, a 2 nm Au capping layer is deposited with the same evaporator type used for the Fe deposition. Apart from the protecting aspect, the ions are also moderated in the Au layer which makes possible an efficient transformation with higher energy ions than for the uncovered Fe film.

- Patterning

  The final patterning was performed at IMS Nanofabrication AG in Vienna [116] with patterned Si masks and a special ion beam lithography system.

6.2.1   First preparation

The first preparation to be investigated was meant as an initial attempt to observe the magnetic transformation on a smaller scale than in previous SMOKE experiments. Additionally it was necessary to test cantilevers suited for MFM measurements and find ideal settings for critical parameters such as the parameter "delta height" and scan rate. 1.6 nm of Fe (~ 8 ML) were grown on the Cu substrate with a 2 nm Au capping layer. The sample was irradiated with singly charged Ar ions at different doses with kinetic energies of 2 keV and 5 keV, respectively (Fig. 92). A mask divided into 4 circular "zones" with a 12.5 μm grating constant was used as a writing pattern.
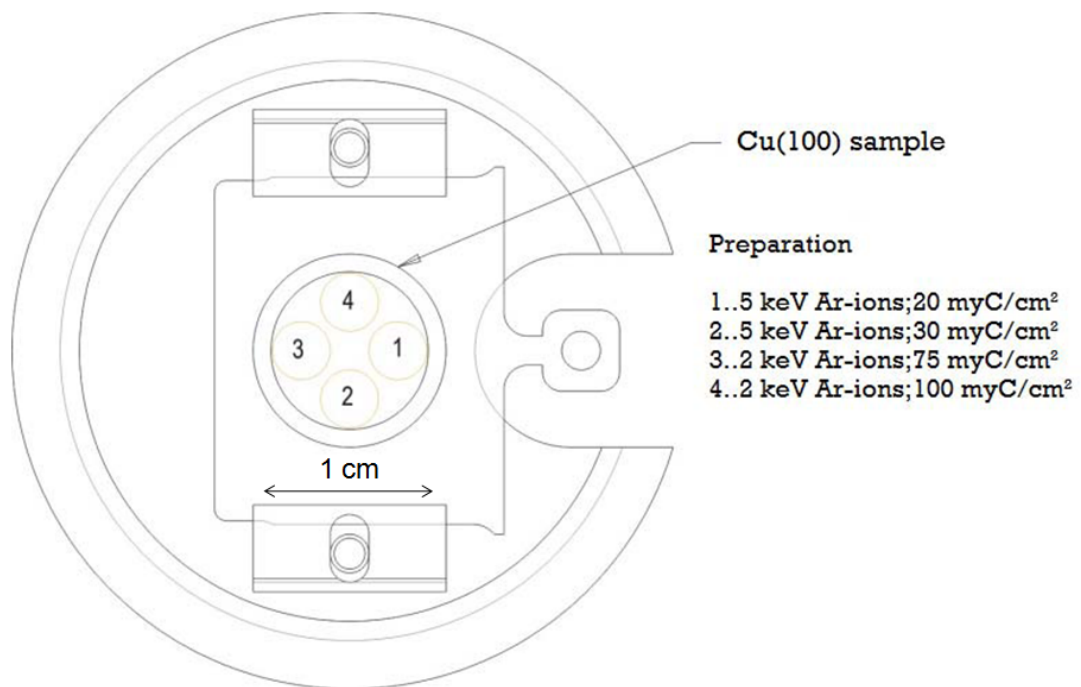
Figure 92: Irradiation mask with four circular openings [58].

Magnetic information was first found in zone 3 (Figs. 94 and 95) using a high coercitivity cantilever (tetrahedral tip shape, tip height: 14 μm, nominal tip radius < 10 nm), consisting of Si, coated with CoPt and FePt and a coercitivity greater than 5000 Oe. Other cantilevers considered were standard MFM cantilevers, coated with CoCr and a coercitivity of 300 - 450 Oe, as well as low moment and high moment cantilevers, all manufactured by Asylum research (Santa Barbara, USA).

Tip magnetization was performed along the axis of the tip (perpendicular to the surface) with a neodym-iron-boron magnet mounted on a precision lever (Fig. 93). This method provides a reproducible magnetization process and allows for comparison of magnetic signals observed with different types of setups (cantilever, scan rate, delta height, etc.). Magnetic contrast was visible with all four types of cantilevers, but best results and reproducibility were obtained with standard cantilevers and especially with high coercitivity cantilevers, making them the preferred probes. However, continuous scans over the same areas of interest show reduction in image quality, assumedly caused by damaging of the magnetic coating and to a lesser extent changes in the domain structure of the tip induced by the sample's stray field.

Figure 93: A permanent magnet mounted on a precision lever allows for reproducible tip magnetization.

For high resolution, it is desirable to decrease the "delta height" to the smallest possible value for higher signal-to-noise ratios. Once the "delta height" becomes smaller than the surface roughness, vibrations occur as the cantilever strikes the surface and the "delta height" must be reset [80]. Images presented throughout this work were recorded with an Asylum Research MFP-3D AFM at typical "delta height" values of 30 - 40 nm.
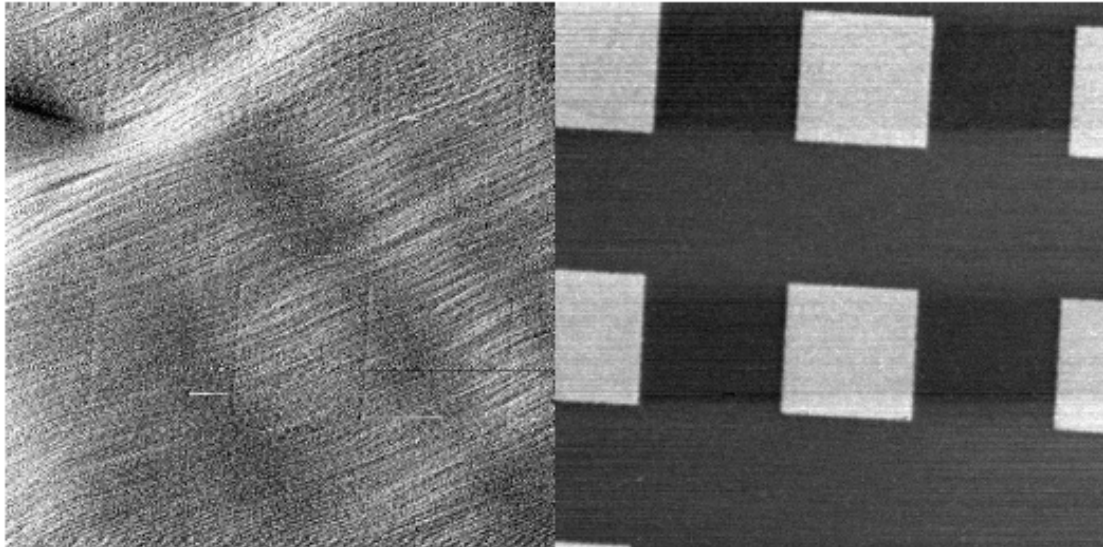
Figure 94: Zone 3: Amplitude trace (left) and magnetic signal (right) of the same area, recorded with a high coercitivity cantilever, 50 μm x 50 μm.
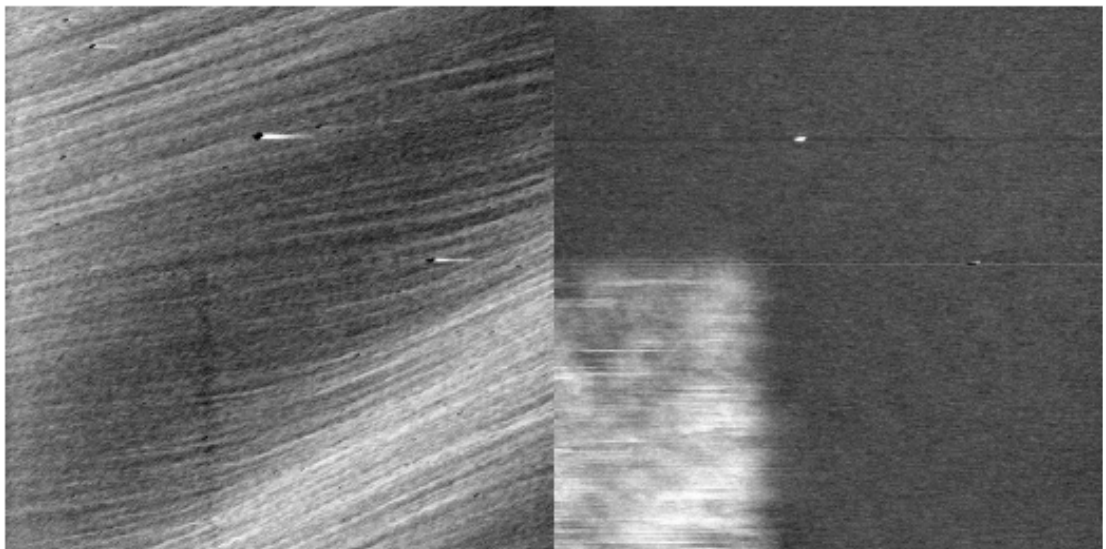

Figure 95: Zone 3: Amplitude trace (left) and magnetic signal (right) of the same area, recorded with a high coercitivity cantilever, 10 μm x 10 μm.
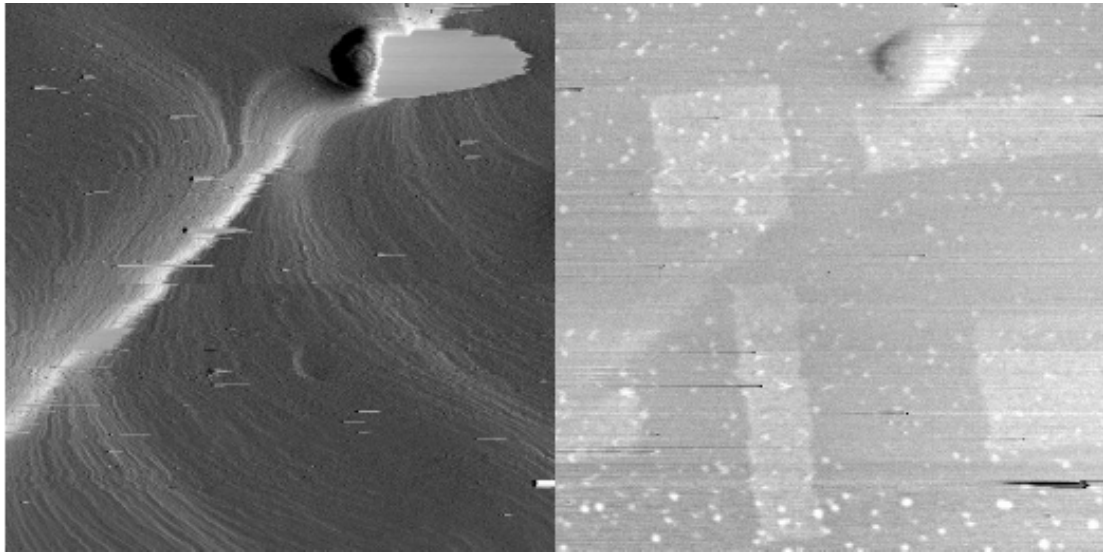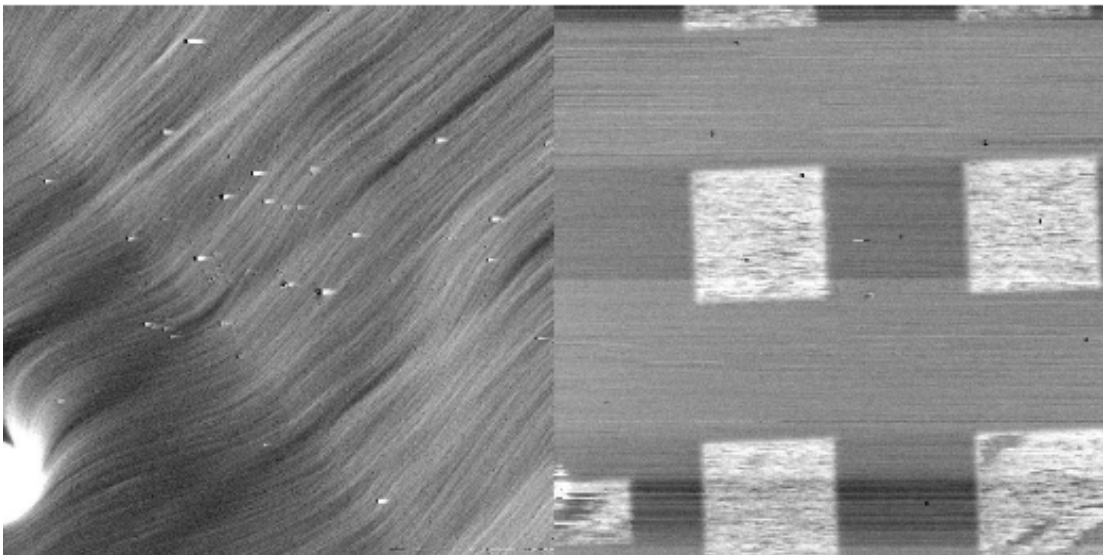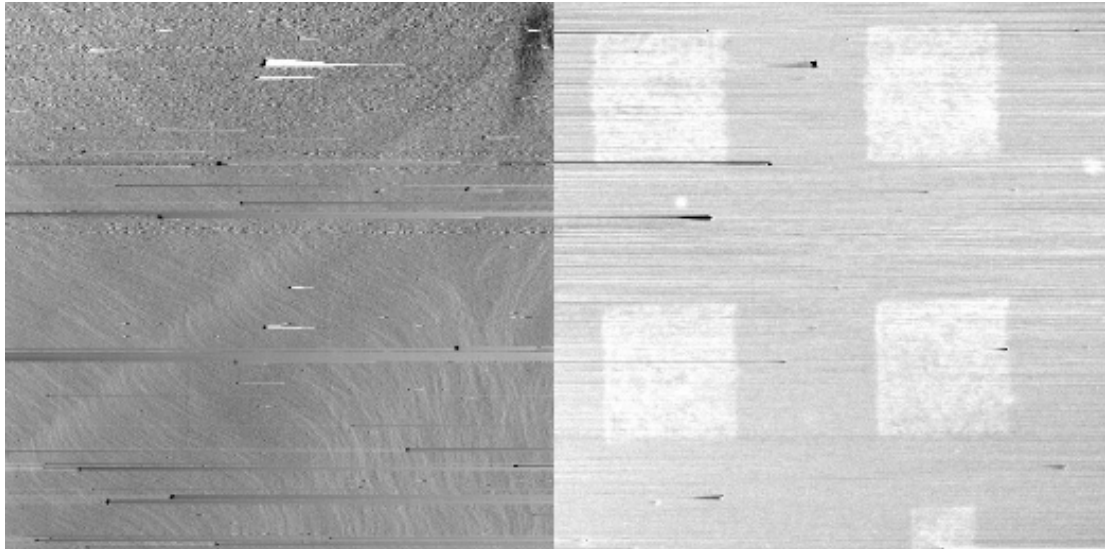
Figure 96: Zone 1: Amplitude trace (left) and magnetic signal (right) of the same area, recorded with a standard MFM cantilever, 50 μm x 50 μm.

Figure 97: Zone 2: Amplitude trace (left) and magnetic signal (right) of the same area, recorded with a high coercitivity cantilever, 50 μm x 50 μm.

Figure 98: Zone 4: Amplitude trace (left) and magnetic signal (right) of the same area, recorded with a standard MFM cantilever, 50 μm x 50 μm.

The highest contrast was found in zone 3 (E = 2 keV, j = 75 μC/cm^2), also showing the most uniform magnetic signal. In zones 2 and 4, variations can be seen in the phase signal from the irradiated area, pointing to incomplete magnetic transformation (Figs. 97 and 98).

The images expose imperfections in the mask structure; stripes break the regular squared pattern.

6.2.2   Second preparation

For the second preparation, again 1.6 nm of Fe were grown on Cu(100) with a 2 nm Au capping layer. A total of 37 spots were irradiated with 5 keV and 10 keV singly charged Ar ions, using a projection-mask (Fig. 99) that was scaled down by a factor of 200 by means of a lens system.
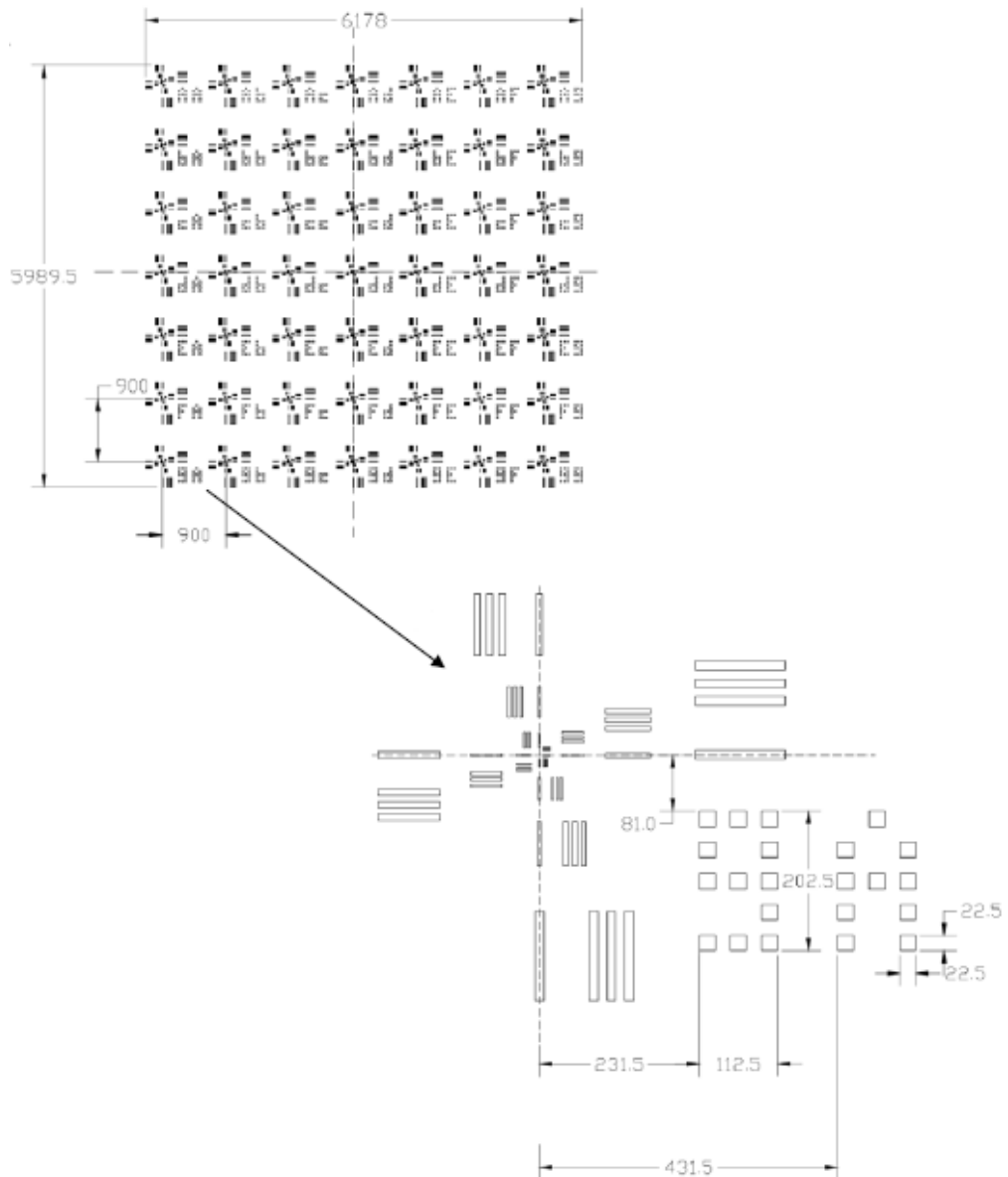
Figure 99: Projection mask, all values in μm.
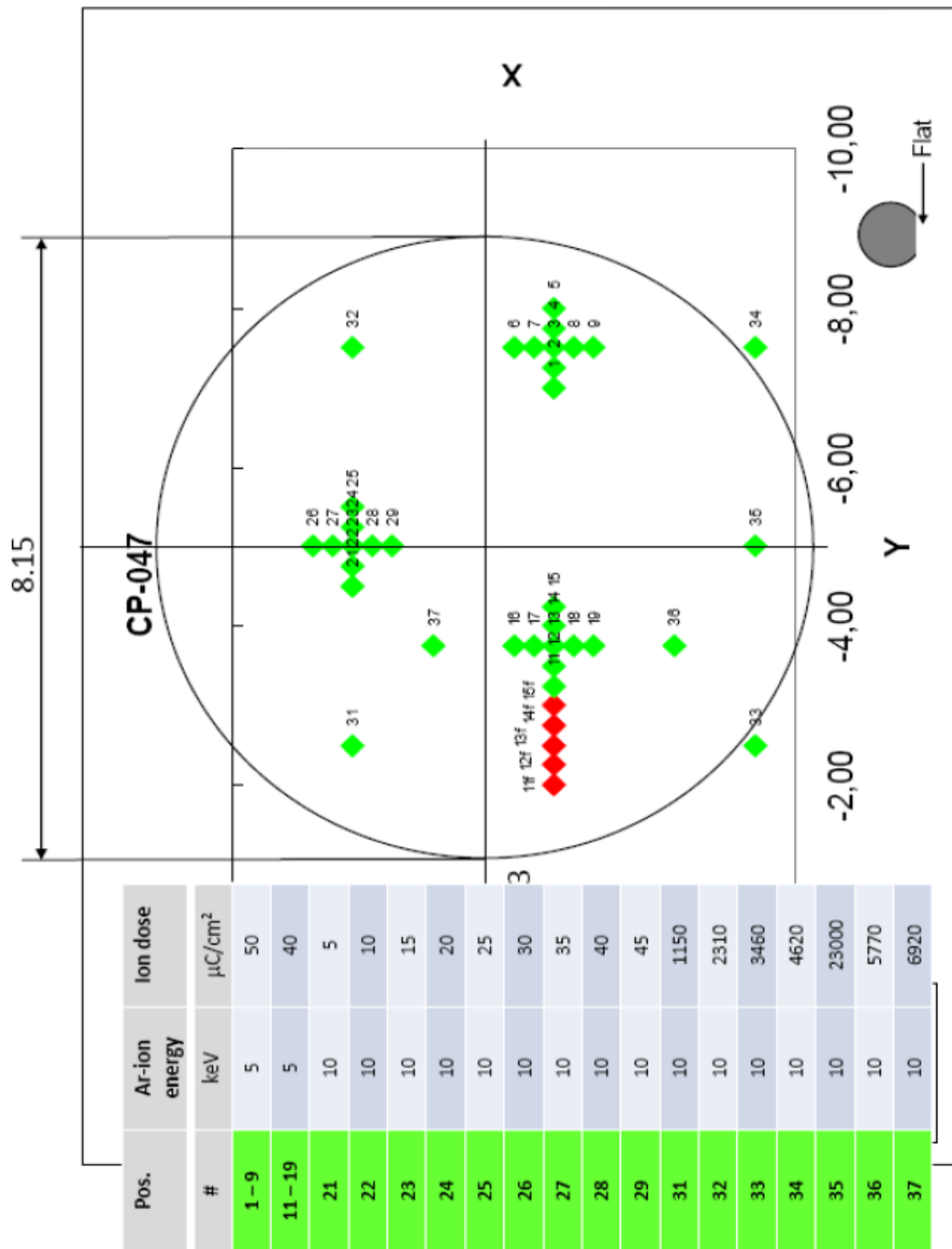
Figure 100: Positioning of ion beams with corresponding ion energies and doses.

The aim of this study was to determine how well single structures can be resolved and to compare magnetic transformation at different ion doses.
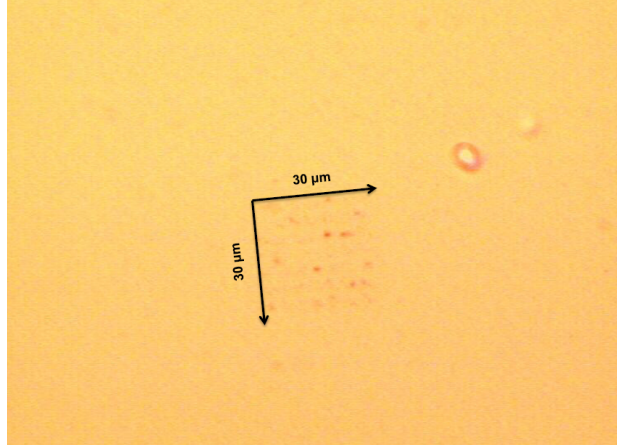
Figure 101: Optical microscopy image of spot 31.

Doses ranging from 1150 $\mu C/cm^2$ to 23000 $\mu C/cm^2$ were applied to seven single spots (31 - 37, see Fig. 100). At these doses, surface atoms are sputtered away and only topographic changes are visible in AFM images, used as positional markers on the target. Lower doses were applied to 3 different areas in cross-like patterns, spots 1 - 9 (E = 5 keV, j = 50 $\mu C/cm^2$), spots 11 - 19 (E = 5 keV, j = 40 $\mu C/cm^2$) and spots 21 - 29 (E = 10 keV, j = 5 $\mu C/cm^2$ - 45 $\mu C/cm^2$) (Fig. 100). To find all the areas of interest on the sample, it was first necessary to have a means of orientation. Spots irradiated at high doses could be detected by optical microscopy (Fig. 101).
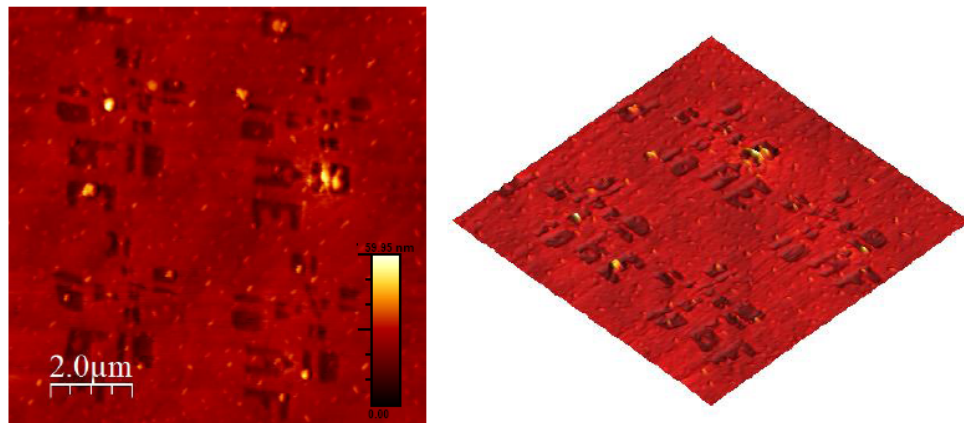

Figure 102: Amplitude trace and 3d-image of spot 31, the orientation of the visible grained structure is possibly correlated to the orientation of the Cu(100) substrate.

After the first finding of an irradiated area with the optical microscope and confirmation via topographic AFM (Fig. 102), a series of single optical microscopy images was taken, which were eventually merged together to create a map of the sample (Fig. 103).
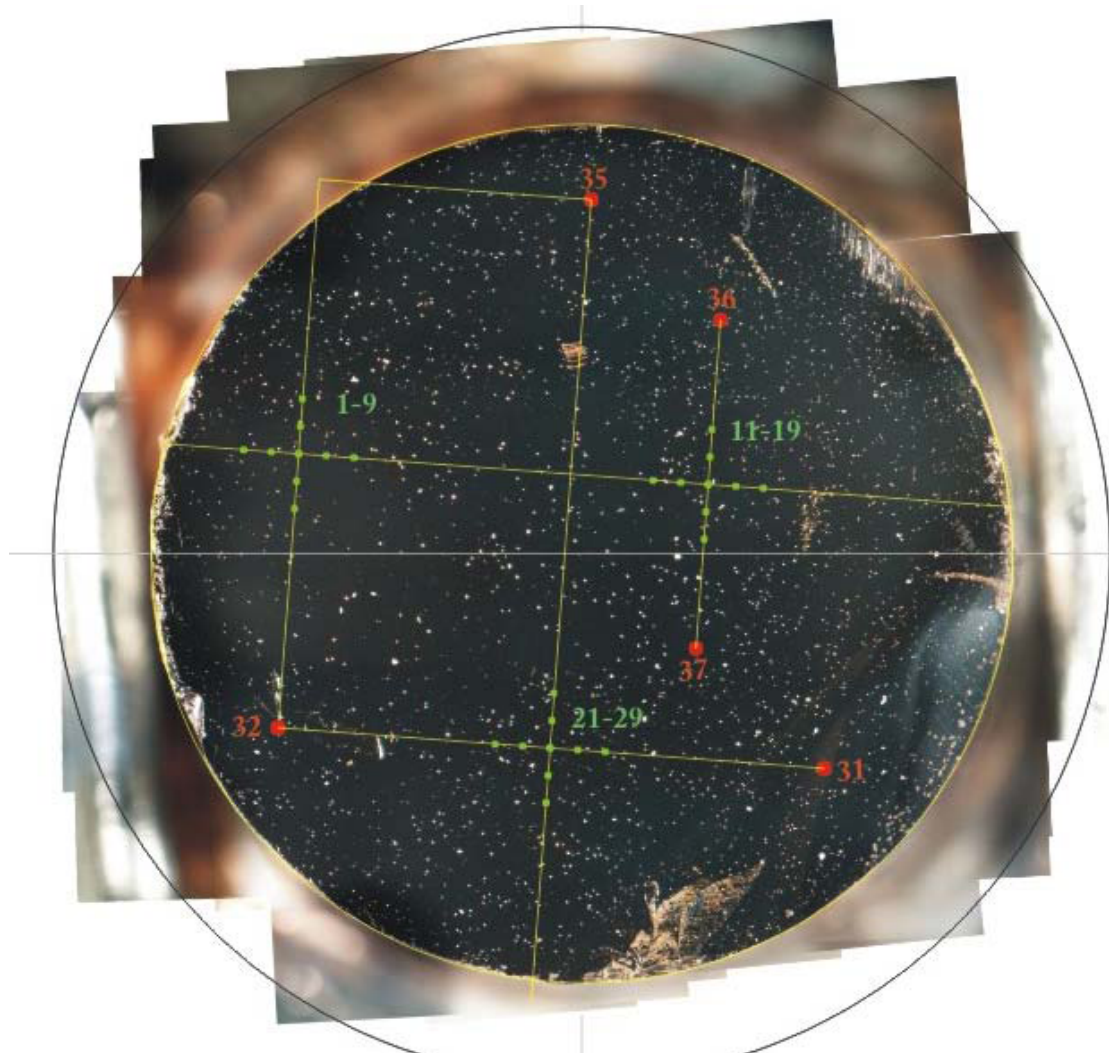

Figure 103: Merged optical microscopy images form a "defect map", allowing for orientation on the sample.

Red markers (high doses) in Fig. 103 correspond to spots that could be seen with the optical microscope at appropriate magnification. Green markers (low doses) indicate spots where magnetic transformation was measured. These were located constructively.
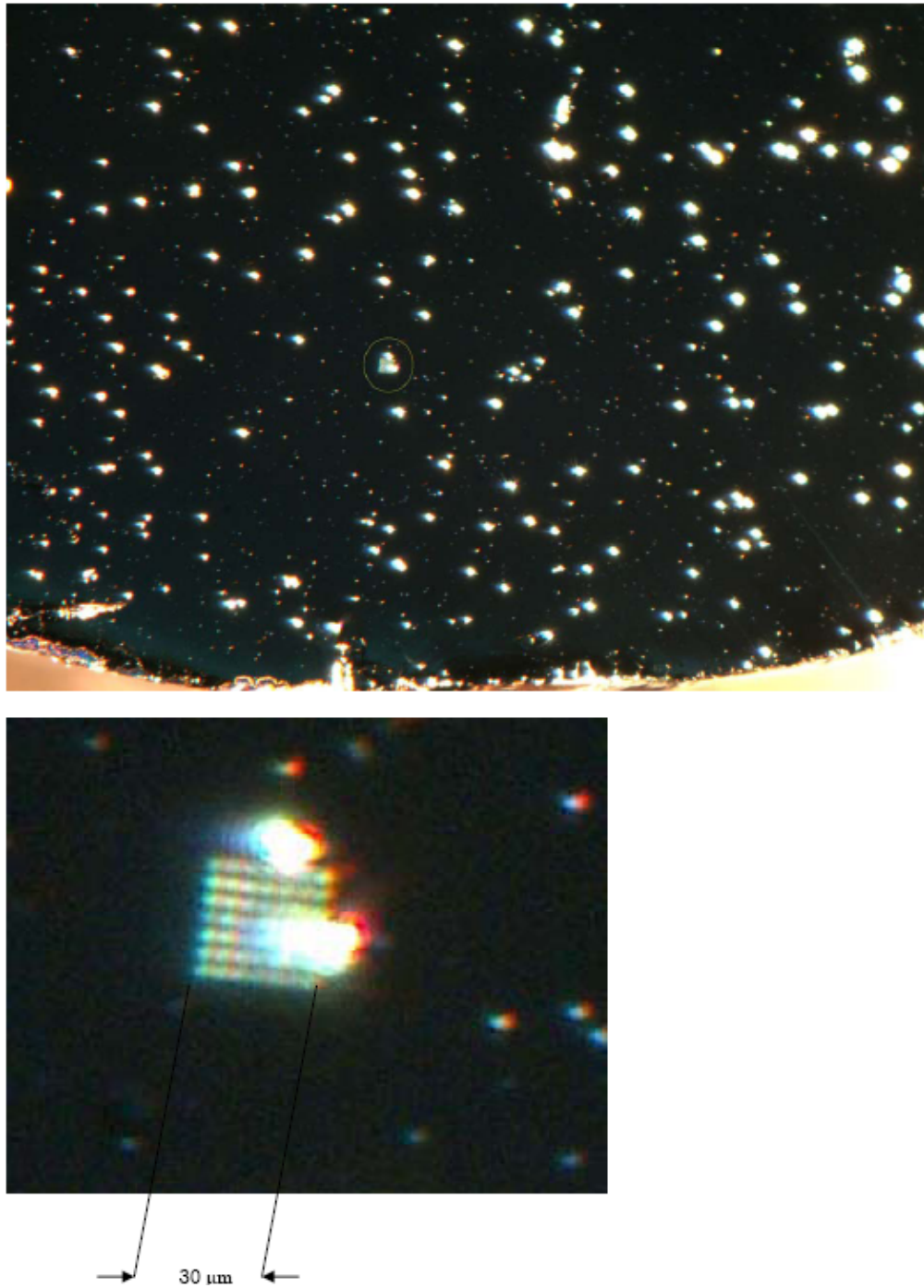
30 μm

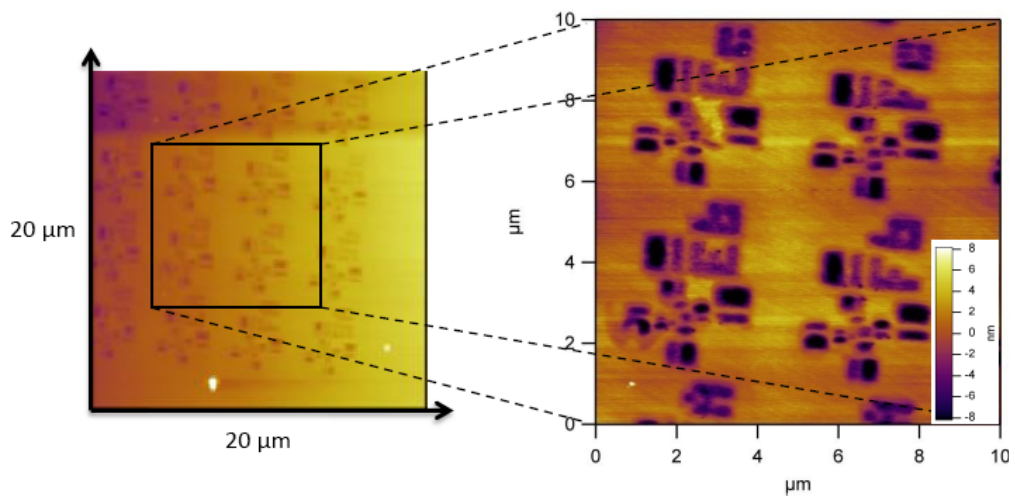Figure 104: Optical microscopy images of spot 35.

Figure 105: Height trace of spot 35 recorded in contact mode AFM.

In order to find the magnetically transformed regions, areas of interest were magnified and the images used as maps for defect-wise orientation (Fig. 106).
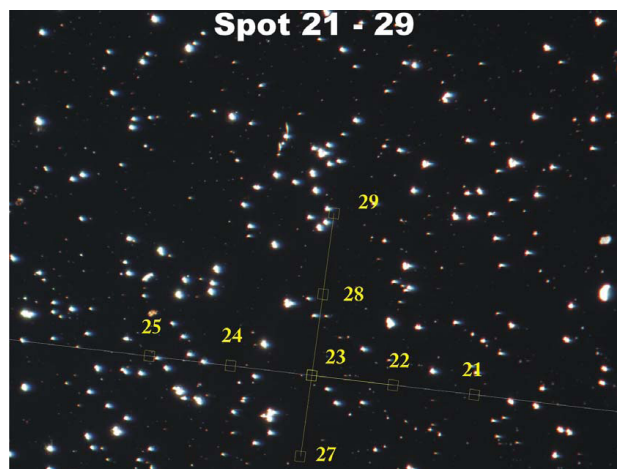

Figure 106: Location of irradiated spots.

The MFP-3D microscope is equipped with top view optics, providing for orientation on opaque samples. Comparison of the surface features as seen on the optical microscopy images with those from the live camera image allowed for a point wise approach to irradiated areas.
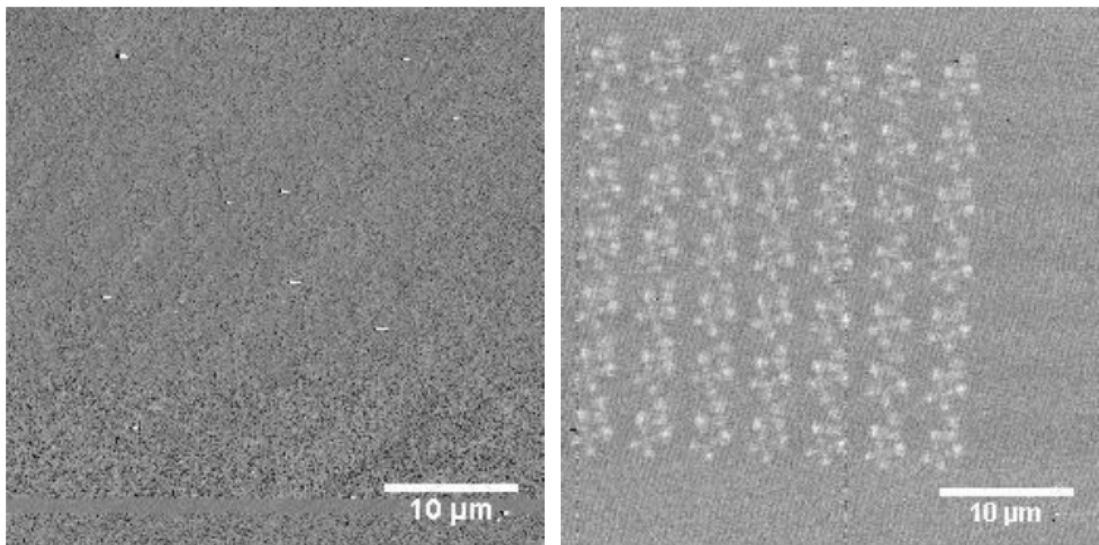
Figure 107: Spot 14: Height trace (left) and magnetic signal (right) of the same area, recorded with a standard MFM cantilever.
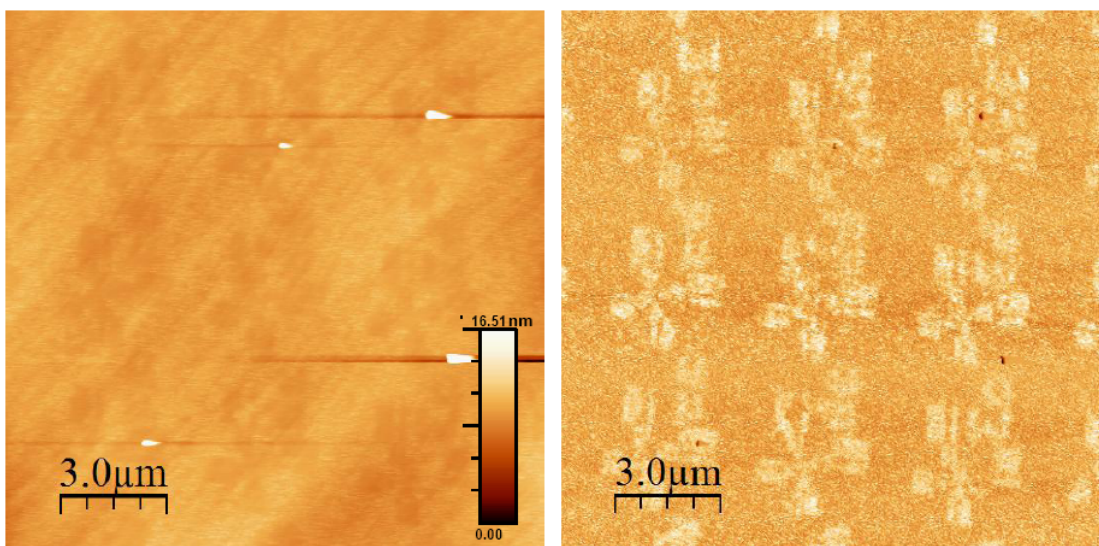

Figure 108: Spot 14: Height trace (left) and magnetic signal (right) of the same area, recorded with a standard MFM cantilever (zoomed in from Fig. 107).

114

The first images were taken from spot 14 with a standard MFM tip at a "delta height" of 40 nm. In Fig. 107, topographic and magnetic information are completely separated. In Fig. 108, mask details can also be seen in the height trace. Whether irradiation at these doses really creates damage, or if the effect is due to magnetic forces, could not unequivocally be answered.

The next series of images was recorded with a high coercitivity cantilever at a delta height of 30 nm. After finishing the series, the first scan was repeated to make sure that tip properties and therefore image quality had not changed during the scanning process to guarantee comparability between the images.

With increasing ion doses in Figs. 111 - 113 (spot 23: j = 15 μC/cm^2; spot 25: j = 25 μC/cm^2; spot 29: j = 45 μC/cm^2), magnetic contrast becomes stronger and more clear cut. Unsurprisingly, the possible topographic effect, most evidently in Figs. 109 and 113, also increases with ion dose.
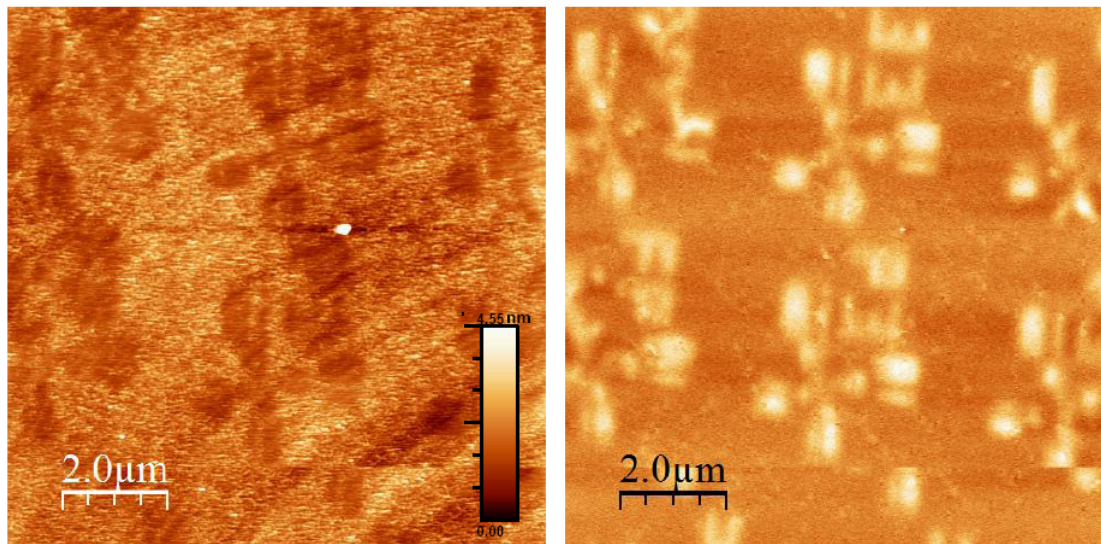

Figure 109: Spot 13: Height trace (left) and magnetic signal (right) of the same area, recorded with a high coercitivity cantilever.
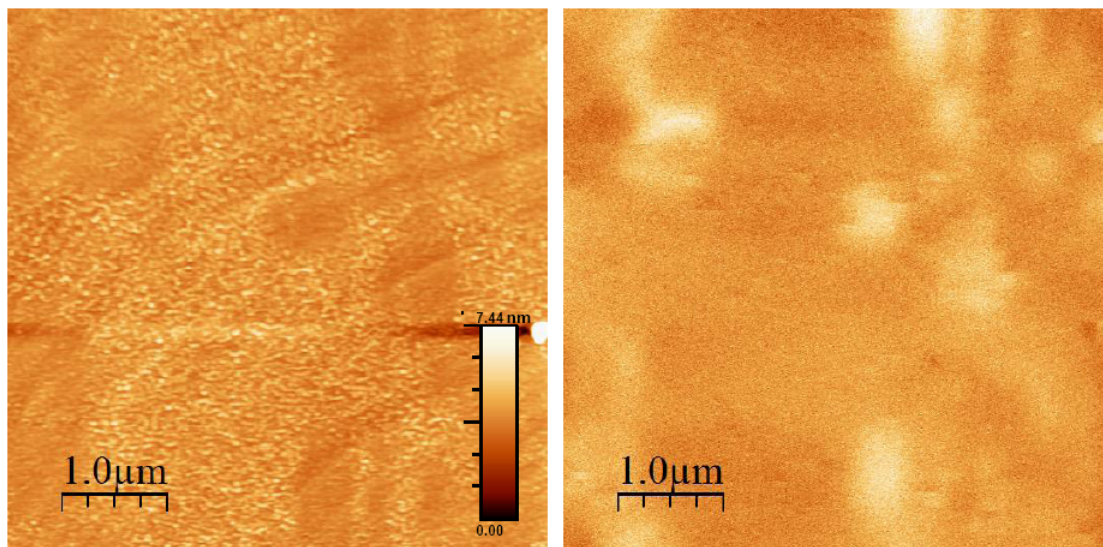
Figure 110: Spot 13: Height trace (left) and magnetic signal (right) of the same area, recorded with a high coercitivity cantilever.

Figure 111: Spot23: Amplitude trace (left) and magnetic signal (right) from the same area, recorded with a high coercitivity cantilever.
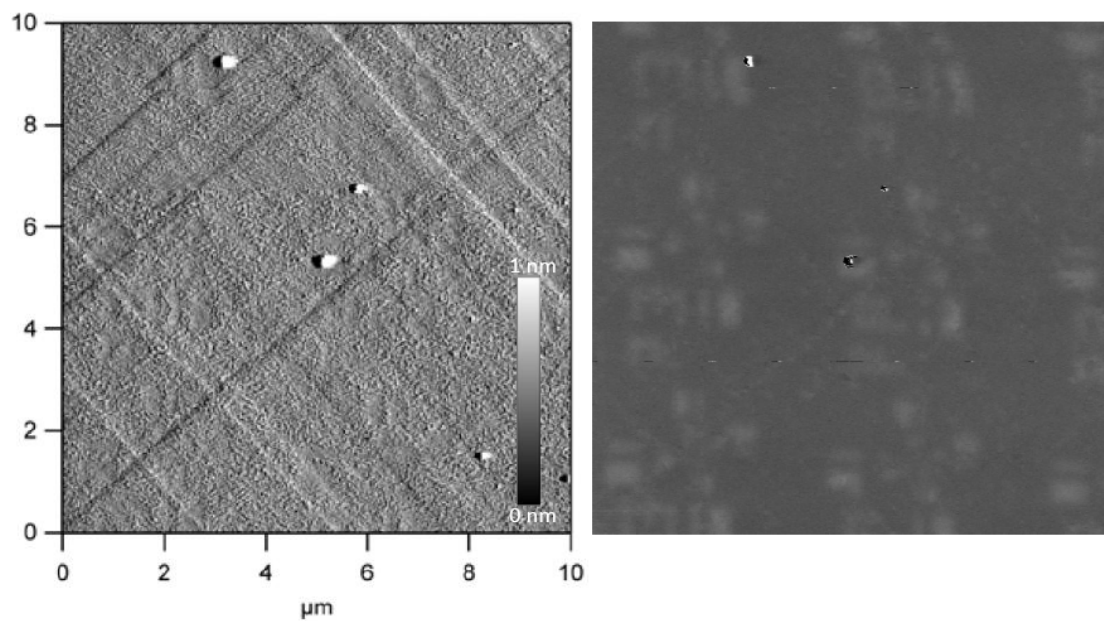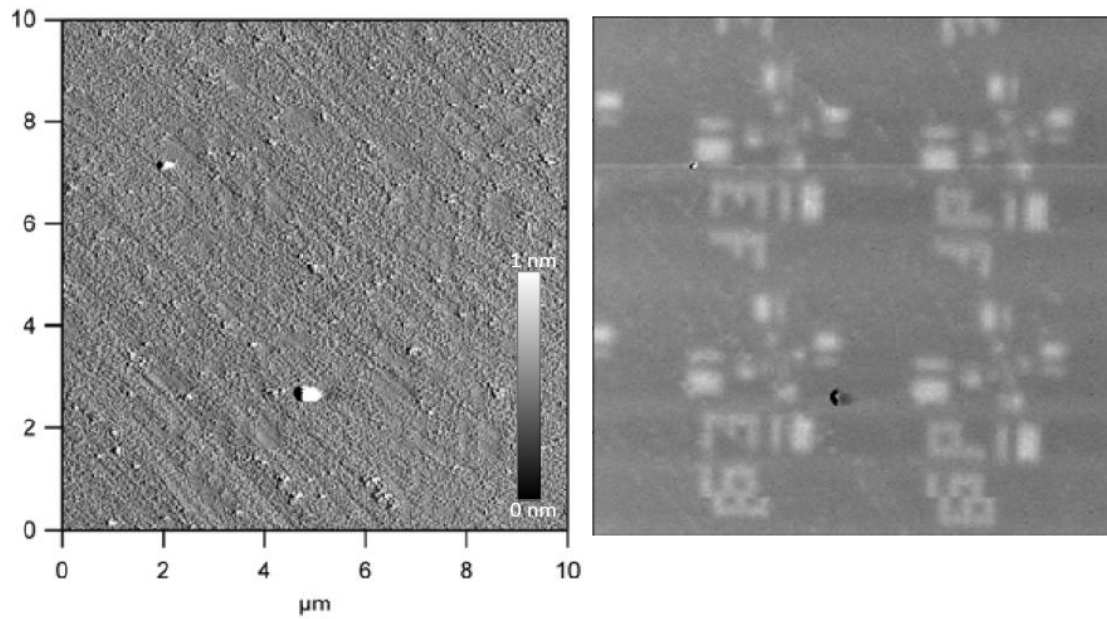
Figure 112: Spot 25: Amplitude trace (left) and magnetic signal (right) from the same area, recorded with a high coercitivity cantilever.
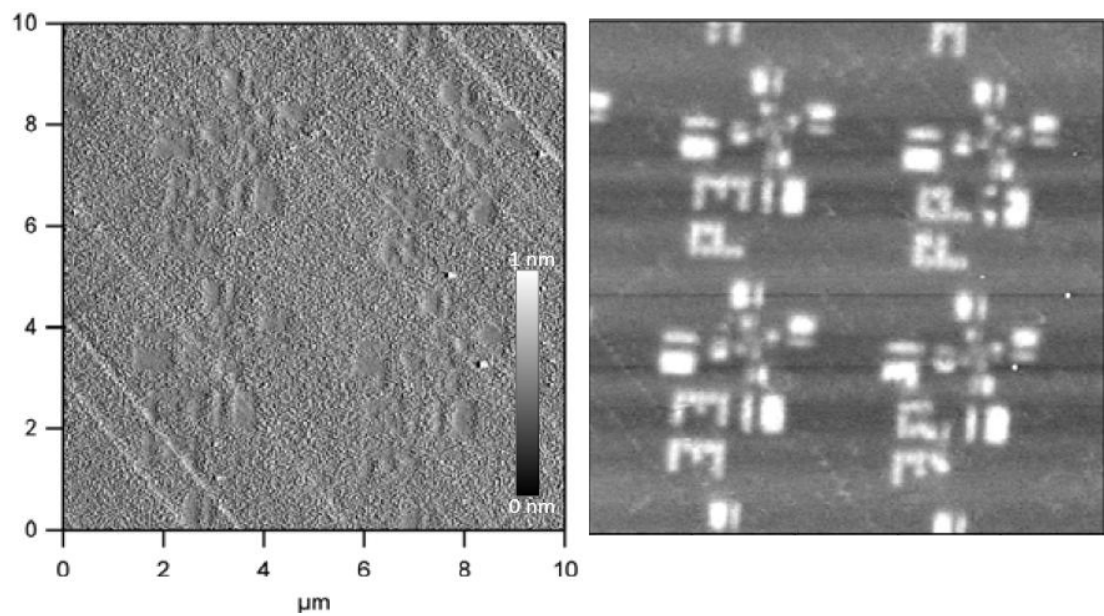
Figure 113: Spot 29: Amplitude trace (left) and magnetic signal (right) from the same area, recorded with a high coercitivity cantilever.

A measurement of spot 29 two weeks after the first results showed comparable contrast in the magnetic signal but no more visible features in the amplitude trace (Fig. 114). An attempt to investigate the same spot with a silicon-nitride cantilever in contact mode AFM did not yield any evidence of a topographic modification.

Figure 114: Spot 29: Amplitude trace (left) and magnetic signal (right) of the same area, recorded with a standard MFM cantilever.

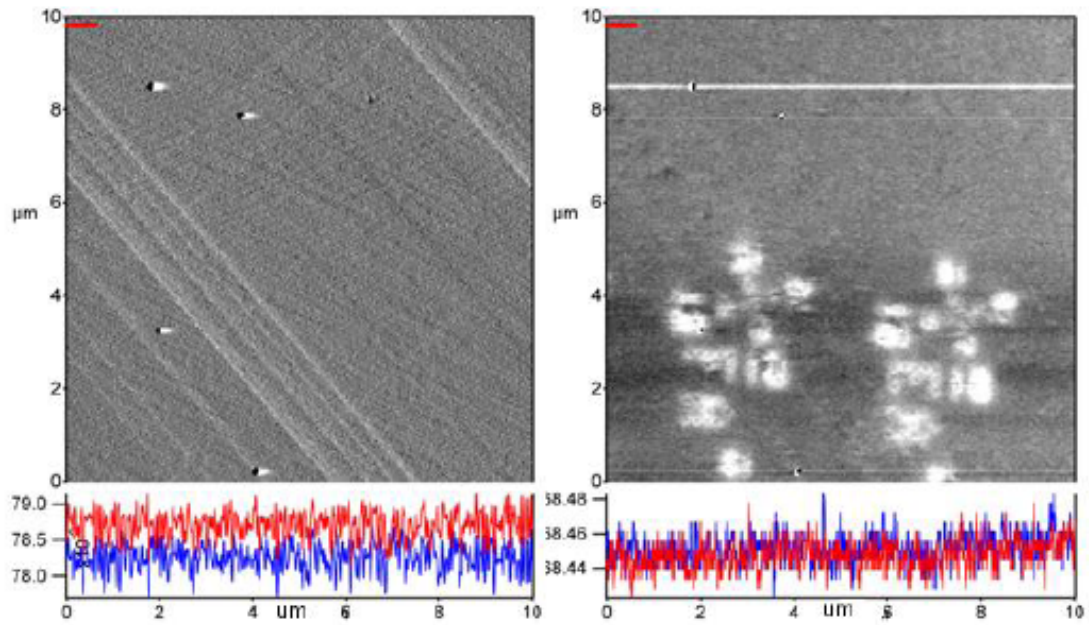# 7   Conclusions and outlook

Experiments described and carried out in this work have shown that the large potential energy stored in highly charged ions alone can be sufficient to induce effects (e.g. potential sputtering and nanodefect formation) in analogy to the case of fast ions which, however, unavoidably cause some unwanted radiation damage in deeper layers by depositing their high kinetic energies. The restriction of ion-surface interactions to the topmost surface layers make slow highly charged ions a promising new tool for "gentle" surface nanostructuring [1].

In the case of CaF_2, the experimental work with respect to evaluation of hillock dimensions in dependence of potential energy and kinetic energy can be considered quite complete. Based on the observations, a modified inelastic thermal spike model ([9], [112]) has been developed and successfully applied to qualitatively explain the existence and shift of the threshold charge state for hillock formation observed for projectiles with different kinetic energies. Since potential energy thresholds for the production of surface-nanodefects seem to emerge for a larger variety of materials, it is planned to further refine this model and to make test predictions for other materials.
One of the long term goals is to proceed from a random distribution of surface structures to well ordered patterns. A method which holds a lot of promise to achieve precise projectile positioning is based on self-organized guiding of charged projectiles through nano-capillaries ([117], [118]).

Interpretation of the results obtained in the studies on HOPG and mica, due to the complicated image formation in atomic force microscopy, is difficult. Although the found structures, for now, cannot be interpreted as hillocks in the common topographic sense, the results are still very encouraging and a continuation of the studies seems worthwhile as structures had never been seen before with AFM in the investigated charge state regimes. Therefore further experiments are being planned to investigate the nature of the defects more systematically.

First MFM results from 8 ML thick Fe films on Cu(100) demonstrate the feasibility of magnetic nanopatterning by ion beam lithography and set the stage for further investigations. It remains to be determined if the found resolution of ~ 100 nm is limited by inaccurate focusing, by the resolution of the instrument or a combination of both.

The study of ion-surface interactions holds a plethora of new potential applications which may soon find entry into our everyday lives. Especially the relatively young field of slow highly charged ion-induced surface modifications which is widely unexplored will increasingly attract interest in the years to come.

Acknowledgements

Lieber Fritz,

Ich danke Dir herzlich, dass Du immer ein offenes Ohr für meine Sorgen bezüglich dieser Arbeit und der Voranbringung derselben hattest. Du hast mir die Möglichkeit gegeben, an einem interessanten Projekt teilzunehmen und meinen wissenschaftlichen Horizont durch diverse Auslandsaufenthalte zu erweitern. Die Gelassenheit und Geduld, die Du trotz Deiner zahllosen Verpflichtungen und Engagements immer ausstrahlst, schaffen für alle Mitglieder dieser Arbeitsgruppe ein sehr angenehmes Arbeitsklima. Du bist ein echter Mentor, der Schülern sein Wissen und seine Erfahrungen mit aller Kraft weiterzugeben versucht und sie immer als gleichberechtigte Kollegen betrachtet. Ich habe die Zeit sehr genossen und viel mitnehmen dürfen, vielleicht wird es ja auch nicht unsere letzte Zusammenarbeit bleiben...

Liebe Ille,

Mit deiner Vorlesung "Introduction to Nanotechnology" hast du mir Augen und Ohren für die "Nanowelt" und gleichzeitig die Tür zu unserer Arbeitsgruppe geöffnet. Auch wenn die Diplomarbeit nicht ganz das geworden ist, was wir anfangs geplant hatten, möchte ich Dir dafür ganz herzlich danken. Du strahlst eine Begeisterung für das Fach und gleichzeitige Kompetenz aus, mit der Du auch Außenstehende spielend in deinen Bann ziehen kannst. Deinem inner- und außeruniversitärem Engagement zolle ich größte Bewunderung und ich bin mir sicher, dass Du mit Deiner Energie und Lebensfreude noch viele junge Wissenschaftler inspirieren wirst.

Liebe Kollegen,

Im Zuge meiner Studienzeit durfte ich viele, überaus begabte und freundliche Kollegen kennenlernen, Erfahrungen sammeln und weitergeben und Freundschaften schließen, die weit über das Interesse am gemeinsamen Studium hinausgehen. Ich möchte hiermit allen, einigen aber explizit meinen Dank aussprechen:

Lieber Thomas, von der ersten Minute auf der Uni haben wir praktisch alles gemeinsam gemacht, gelernt und den schweren Studieneinstieg rückblickend doch erstaunlich gut hinter uns gebracht. Nun haben sich zwar im letzten Jahr unsere Wege einigermaßen getrennt, aber ich bin guter Dinge, dass wir bald auf unsere Abschlüsse anstoßen können und wieder an die guten alten Zeiten anschließen. Hier sei auch meiner "Buddy-Gruppe" aus der regulären Studienzeit gedankt: Christoph Deutsch, Robert Amsüss und Markus Schiebl.

Acronyms

AD   *Auger deexcitation*

AI   *auto-ionization*

amu   *atomic mass unit*

AN   *Auger neutralization*

AFM   *atomic force microscope/microscopy*

bcc   *body-centered cubic*

COB model   *classical over-the-barrier model*

DS   *defect mediated sputtering*

EBIS   *electron beam ion source*

EBIT   *electron beam ion trap*

ECRIS   *electron cyclotron resonance ion source*

fcc   *face-centered cubic*

HCI   *highly charged ion*

HOPG   *highly ordered pyrolytic graphite*

ID   *interstitial defect*

KAPS   *kinetically assisted potential sputtering*

KE   *kinetic emission*

MCI   *multiply charged ion*

MFM   *magnetic force microscope/microscopy*

ML *monolayer*

MOKE   *magneto-optic Kerr effect*

PE   *potential emission*

QRN   *quasi-resonant neutralization*

RI   *resonant ionization*

RN   *resonant neutralization*

SMOKE   *surface magneto-optic Kerr effect*

SPM   *scanning probe microscope/microscopy*

SRIM   *stopping and range of ions in matter*

STE   *self-trapped exciton*

STH   *self-trapped hole*

STM   *scanning tunneling microscope/microscopy*

UHV   *ultra high vacuum*

VD   *vacancy defect*

References

[1] *Slow Highly Charged Ions - A New Tool For Surface Nanostructuring?*
F. Aumayr and H. P. Winter,
e-J. Surf. Sci. Nanotech. **1**, 171 (2003).

[2] *Nano-sized surface modifications induced by the impact of slow highly charged ions - A first review,*
F. Aumayr, A. S. El-Said and W. Meissl,
doi:10.1016/j.nimb.2008.03.106 in print.

[3] *Nuclear tracks in solids: registration physics and the compound spike,*
L. T. Chadderton,
Radiation Measurements **36**, 13 (2003).

[4] *Energy dissipation of fast heavy ions in matter,*
G. Schiwietz, E. Luderer, G. Xiao and P. L. Grande,
Nucl. Instrum. Meth. B **175**, 1 (2001).

[5] *Damage structure in the ionic crystal LiF irradiated with swift heavy ions,*
C. Trautmann, M. Toulemonde, K. Schwartz, J. M. Costantini and A. Muller,
Nucl. Instrum. Meth. B **164**, 365 (2000).

[6] *Characterization of swift heavy ion tracks in CaF_2 by scanning force and transmission electron microscopy,*
N. Khalfaoui, C. C. Rotaru, S. Bouffard, M. Toulemonde, J. P. Stoquert, F. Haas, C. Trautmann, J. Jensen and A. Dunlop,
Nucl. Instrum. Meth. B **240**, 819 (2005).

[7] *Ion tracks on LiF and CaF_2 single crystals characterized by scanning force microscopy,*
C. Müller, M. Cranney, A. El-Said, N. Ishikawa, A. Iwase, M. Lang and R. Neumann,
Nucl. Instrum. Meth. B **191**, 246 (2002).

[8] *Study of heavy-ion induced modifications in BaF_2 and LaF_3 single crystals,*
A.S. El-Said, M. Cranney, N. Ishikawa, A. Iwase, R. Neumann, K. Schwartz, M. Toulemonde and C. Trautmann,
Nucl. Instrum. Meth. B **218**, 492 (2004).

[9] *Potential energy threshold for nano-hillock formation by impact of slow highly charged ions on a CaF$_2$(111) surface,*
A. S. El-Said, W. Meissl, M.C. Simon, J. R. Crespo López-Urrutia, C. Lemell, J. Burgdörfer, I. C. Gebeshuber, H. P. Winter, J. Ullrich, C. Trautmann, M. Toulemonde and F. Aumayr,
Nucl. Instrum. Meth. B **258**, 167 (2007).

[10] *Planar patterned magnetic media obtained by ion irradiation,*
C. Chappert, H. Bernas, J. Fer´a, V. Kottler, J. Jamet, E. Chen, Y. Cambril, T. Devolder, F. Rousseaux, V. Mathelt and H. Launois,
Science **280**, 1919 (1998).

[11] *Inelastic interactions of slow ions and atoms with surfaces,*
F. Aumayr and H. P. Winter,
Nucl. Instrum. Meth. B **233**, 111 (2005).

[12] *Interaction of slow multicharged ions with solid surfaces,*
A. Arnau, F. Aumayr, P. M. Echenique, M. Grether, W. Heiland, J. Limburg, R. Morgenstern, P. Roncin, S. Schippers, R. Schuch, N. Stolterfoht, P. Varga, T. J. M. Zouros and H. P. Winter,
Surf. Sci. Reports **27**, 113 (1997).

[13] *Topical review: Hollow atoms,*
H. P. Winter and F. Aumayr,
J. Phys. B: At. Mol. Opt. Phys. **32**, R39 (1999).

[14] *The interaction of slow highly charged ions on surfaces,*
J.-P. Briand, G. Giardino, G. Borsoni, V. Le Roux, N. Béchu, S. Dreuil, O. Tüske and G. Machicoane,
Rev. Sci. Instrum. **71**, 627 (2000).

[15] *Precise total electron yield measurements for impact of singly or multiply charged ions on clean solid surfaces,*
H. Eder, M. Vana, F. Aumayr and H. P. Winter,
Rev. Sci. Instrum. **68**, 165 (1997).

[16] *Electron emission from ion-bombarded aluminium,*
B. Svensson and G. Holmén,
J. Appl. Phys. **52**, 6928 (1981).

[17] *Electron emission from a metal surface bombarded by slow highly charged ions,*
M. Delaunay, M. Fehringer, R. Geller, D. Hitz, P. Varga and H. P. Winter,
Phys. Rev. B **35**, 4232 (1987)**.**

[18] *Collisions of atoms and ions with surfaces under grazing incidence,*
H. Winter,
Physics Reports **367**, 387 (2002).

[19] *Auger ejection of electrons from tungsten by noble gas ions,*
H. D. Hagstrum,
Phys. Rev. **96**, 325 (1954).

[20] *Theory of Auger ejection of electrons from metals by ions,*
H. D. Hagstrum,
Phys. Rev. **96**, 336 (1954).

[21] Diplomarbeit: *Elektronen-Emission bei Beschuss von Isolator- und Metall-Oberflächen mit hochgeladenen Ionen,*
M. C. Simon, IAP TU Wien (2007).

[22] *Production of hollow atoms by the excitation of highly charged ions in interaction with a metallic surface,*
J. P. Briand, L. de Billy, P. Charles, S. Essabaa, P. Briand, R. Geller, J. P. Desclaux, S. Bliman and C. Ristori,
Phys. Rev. Lett. **65**, 159 (1990).

[23] *On the formation of hollow atoms in front of an insulating LiF surface,*
J. Limburg, S. Schippers, R. Hoekstra, R. Morgenstern, H. Kurz, M. Vana, F. Aumayr and H. P. Winter,
Nucl. Instrum. Meth. B **115**, 237 (1996).

[24] *Do hollow atoms exist in front of an insulating LiF(100) surface?*
J. Limburg, S. Schippers, R. Hoekstra and R. Morgenstern,
Phys. Rev. Lett. **75**, 217 (1995).

[25] *Above-surface neutralization of highly charged ions: The classical over-the-barrier model,*
J. Burgdörfer, P. Lerner and F. W. Meyer,
Phys. Rev. A **44**, 5674 (1991).

[26] *Above-surface neutralization of slow highly charged ions in front of ionic crystals,*
L. Hägg, C. O. Reinhold and J. Burgdörfer,
Phys. Rev. A 55, 2097 (1997).

[27] *Liouville master equation for multielectron dynamics: Neutralization of highly charged ions near a LiF surface,*
L. Wirtz, C. O. Reinhold, C. Lemell and J. Burgdörfer,
Phys. Rev. A **67**, 012903 (2003).

[28] *Emission of electrons from a clean gold surface induced by slow, very highly charged ions at the image charge acceleration limit,*
F. Aumayr, H. Kurz, D. Schneider, M. A. Briere, J. W. McDonald, C. E. Cunningham and H. P. Winter,
Phys. Rev. Lett. **71**, 1943 (1993).

[29] *Image acceleration of highly charged ions by metal surfaces,*
C. Lemell, H. P. Winter, F. Aumayr, J. Burgdörfer and F. W. Meyer,
Phys. Rev. A **53,** 880 (1996).

[30] *Mechanisms and theory of physical sputtering by particle impact,*
P. Sigmund,
Nucl. Instrum. Meth. B **27**, 1 (1987).

[31] *Potential Sputtering,*
F. Aumayr and H. P. Winter,
Phil. Trans. R. Soc. Lond. **362**, 77 (2004).

[32] *Potential sputtering of lithium fluoride by slow multicharged ions,*
T. Neidhart, F. Pichler, F. Aumayr, H. P. Winter, M. Schmid and P. Varga,
Phys. Rev. Lett. **74**, 5280 (1995).

[33] *Secondary-emission of alkali-halide crystals by bombardment with Ar^{+} – Ar^{5+} and Kr^{+} – Kr^{5+} multi-charged ions,*
S. Radzhabov, R. Rakhimov and P. Abdusalumav,
Izv. Akad. Nauk SSSR **40**, 2543 (1967).

[34] *Ion and electron-emission of LiF, NaCl and Si mono-crystals under the influence of multicharged ions of various elements,*
S. N. Morozov, D. Gurich and D. Arifov,
Izv. Akad. Nauk SSSR **43**, 612 (1979).

[35] *Ion/surface interaction studies with 1-3eV/amu ions up to Th^{80+},*
D. H. Schneider, M. A. Briere, J. McDonald and J. Biersack,
Rad. Eff. Def. Sol. **127**, 113 (1993).

[36] *Secondary ion emission from lithium-fluoride under impact of slow multicharged ions,*
T. Neidhart, F. Pichler, H. P. Winter, F. Aumayr, M. Schmid and P. Varga,
Nucl. Instrum. Meth. B **98**, 465 (1995).

[37] *Sputter yields of insulators bombarded with hyperthermal multiply charged ions,*
P. Varga, T. Neidhart, M. Sporn, G. Libiseller, M. Schmid, F. Aumayr and H. P. Winter,
Phys. Scr. **T37**, 307 (1997).

[38] *Potential sputtering of clean SiO_2 by slow highly charged ions,*
M. Sporn, G. Libiseller, T. Neidhart, M. Schmid, F. Aumayr, H. P. Winter, P. Varga, M. Grether and N. Stolterfoht,
Phys. Rev. Lett. **79**, 945 (1997).

[39] *Threshold for potential sputtering of LiF,*
G. Hayderer, M. Schmid, P. Varga, H. P. Winter, F. Aumayr, L. Wirtz, C. Lemell, J. Burgdörfer, L. Hägg and C. O. Reinhold,
Phys. Rev. Lett. **182**, 143 (2001).

[40] *Sputtering of Au and Al_2O_3 surfaces by slow highly charged ions,*
G. Hayderer, S. Cernusca, V. Hoffmann, D. Niemann, N. Stolterfoht, M. Schmid, P. Varga, H. P. Winter and F. Aumayr,
Nucl. Instrum. Meth. B **98**, 465 (1995).

[41] *Kinetically assisted potential sputtering of insulators by highly charged ions,*
G. Hayderer, S. Cernusca, M. Schmid, P. Varga, H. P. Winter and F. Aumayr,
Phys. Rev. Lett. **86**, 3530 (2001).

[42] *A highly sensitive quartz-crystal microbalance for sputtering investigations in slow ion-surface collisions,*
G. Hayderer, M. Schmid, P. Varga, H. P. Winter and F. Aumayr,
Rev. Sci. Instrum. **70**, 3696 (1999).

[43] *The stopping and range of ions in solids,*
J.F. Ziegler, J.P. Biersack and U. Littmark,
New York, Pergamon Press (1984); http://www.srim.org.

[44] *A mechanism for sputtering of non-metals by slow multiply charged ions,*
E. Parilis,
Proc. Int. Conf. "Phenomena in Ionized Gases", 324 (1969).

[45] *Theory for the laser-induced femtosecond phase transition of silicon and GaAs,*
P. Stampfli and K. Bennemann,
J. Appl. Phys. **60**, 191 (1996).

[46] *Off-center self-trapped excitons and creation of lattice-defects in alkali-halide crystals,*
R. T. Williams,.K. S. Song, W. L. Faust and C. H. Leung,
Phys. Rev. B **33**, 7232 (1986).

[47] *Subthreshold radiation-induced processes in the bulk and on surfaces and interfaces of solids,*
N. Itoh,
Nucl. Instrum. Meth. B **135**, 175 (1998).

[48] *Ultrathin metal films: Magnetic and structural properties,*
M. Wuttig and X. Liu,
Springer Berlin, Vol. **206** (2004).

[49] *Stabilization of metastable expanded face-centered-tetragonal manganese,*
J.T. Kohlhepp and W. J. M. de Jonge,
Phys. Rev. Lett. **96**, 237201 (2006).

[50] *Ion-beam induced ferromagnetism of ultrathin Fe films,*
W. Rupp, B. Kamenik, R. Ritter, A. Biedermann, Ch. Klein, E. Platzgummer, M. Schmid and P. Varga,
submitted for publication.

[51] *Surface magneto-optic Kerr effect (SMOKE),*
Z. Q. Qiu and S. Bader,
J.Magn.Magn.Mater. **200**, 664 (1999).

[52] *Magnetic properties of novel epitaxial films,*
S. D. Bader and E. R. Moog,
J. Appl. Phys. **61**, 3729 (1987).

[53] *Magnetic live surface layers in Fe/Cu(100),*
J. Thomassen, F. May, B. Feldmann, M. Wuttig and H. Ibach,
Phys. Rev. Lett. **69**, 3831 (1992).

[54] *Surface magnetism of ultrathin γ-Fe films investigated by nonlinear magneto-optical Kerr effect,*
M. Straub, R. Vollmer and J. Kirschner,
Phys. Rev. Lett. **77**, 743 (1996).

[55] *Nucleation of bcc iron in ultrathin fcc films,*
A. Biedermann, M. Schmid and P. Varga,
Phys. Rev. Lett. **86**, 464 (2001).

[56] *Crystallographic structure of ultrathin Fe films on Cu(100),*
A. Biedermann, R. Tscheließnig, M. Schmid and P. Varga,
Phys. Rev. Lett. **87**, 086103 (2001).

[57] *Local atomic structure of ultra-thin Fe films grown on Cu(100),*
P. Varga, M. Schmid, A. Biedermann and R. Tscheliessing,
Appl. Phys. A **78**, 807 (2004).

[58] Dissertation: *Ionenstrahl induzierter Ferromagnetismus von dünnen Fe Schichten auf Cu(100),*
Werner Rupp, IAP TU Wien (in progress).

[59] *Handbook of ion sources,*
B. Wolf (Editor),
CRC Press (1995).

[60] Dissertation: *Quantum interference in the dielectronic recombination of heavy highly charged ions,*
A. J. González Martínez, Ruperto-Carola Universität Heidelberg (2005).

[61] *A new ion beam facility for slow highly charged ions,*
G. Zschornack, S. Landgraf, S. Facsko, D. Kost,W. Möller, H. Tyrroff, F. Großmann, U. Kentsch, V. P. Ovsyannikov, M. Schmidt and F. Ullmann,
Proceedings of EPAC, Lucerne, 1189 (2004).

[62] *First investigations of a warm electron beam ion trap for the production of highly charged ions,*
V. P. Ovsyannikov and G. Zschornack,
Rev. Sci. Instrum. **70**, 2646 (1999).

[63] *Highly charged ions produced in a warm electron beam ion trap,*
V. P. Ovsyannikov, G. Zschornack, F. Grossmann, S. Landgraf, F. Ullmann and T. Werner,
Rev. Sci. Instrum. **71**, 690 (2000).

[64] *A novel room temperature electron beam ion trap for atomic physics and materials research,*
V. P. Ovsyannikov, G. Zschornack, F. Grossmann, O.K. Koulthachev, S. Landgraf, F. Ullmann and T. Werner,
Nucl. Instrum. Meth. B **161**, 1123 (2000).

[65] *The Dresden EBIT: An ion source for materials research and technological applications of low-energy highly charged ions,*
T. Werner, G. Zschornack, F. Grossmann, V. P. Ovsyannikov and F. Ullmann,
Nucl. Instrum. Meth. B **178**, 260 (2001).

[66] *Dresden EBIT: Results and perspectives,*
U. Kentsch, S. Landgraf, G. Zschornack, F. Grossmann, V. P. Ovsyannikov and F. Ullmann,
Rev. Sci. Instrum. **73**, 660 (2002).

[67] *X-ray spectroscopy and ion extraction at the Dresden EBIT,*
U. Kentsch, S. Landgraf, M. Schmidt, G. Zschornack, F. Grossmann, V. P. Ovsyannikov and F. Ullmann,
Nucl. Instrum. Meth. B **205**, 260 (2003).

[68] *Extraktion hochgeladener Ionen aus der Dresden EBIT im Überlaufregime,*
R. Heller and G. Zschornack,
http://www.mpipks-dresden.mpg.de/∼eas/beitraege27/heller/ueberlauf.pdf.

[69] *http://www.physik.tu-dresden.de/apg/apeecr1.htm*

[70] *http://www.its-leif.org/ACTIVITIES/ARIBE.htm*

[71] *LIMBE: A new facility for low energy beams,*
L. Maunoury, R. Leroy, T. Been, G. Gaubert, L. Guillaume, D. Leclerc, A. Lepoutre, V. Mouton, J. Y. Pacquet, J. M. Ramillon and R. Vicquelin,
Rev. Sci. Instrum. **73**, 561 (2002).

[72] *Classification of scanning probe microscopies,*
G. Friedbacher and H. Fuchs,
Pure Appl. Chem. **71**, 1337 (1999).

[73] *Surface studies by scanning tunneling microscopy,*
G. Binnig, H. Rohrer, C. Gerber, E. Weibel,
Phys. Rev. Lett. **49**, 57 (1982).

[74] *http://www.iap.tuwien.ac.at/www/surface/STM_Gallery,*
     Michael Schmid, IAP TU WIEN.

[75] *Atomic force microscope,*
     G. Binnig and C.F Quate,
     Phys. Rev. Lett. **56**, 930 (1986).

[76] *http://www.bphys.uni-linz.ac.at/bioph/download/BioNano-Praktikum.pdf*

[77] http://www.nanoscience.com/education/i/F-z_curve.gif

[78] http://www.nature.com/v2/n11/images/nmat1001-f7.gif

[79] *Magnetic force microscopy: General principles and application to longitudinal recording media,*
     D. Rugar, H. J. Mamin, P. Guethner, S. E. Lambert, J. E. Stern, I. McFadyen and T. Yogi,
     J. Appl. Phys. **68**, 1169 (1990).

[80] *Magnetic force microscopy,*
     Digital Instruments Support Note No. **229** (1996).

[81] *http://www.iisb.fraunhofer.de/de/jber99/crys_2.gif*

[82] *http://people.uis.edu/kdung1/Gemini/CaF2/corners.jpg*

[83] *Surface nanostructures induced by slow highly charged ions on CaF_2 single crystals,*
     A.S. El-Said, W. Meissl, M. C. Simon, J. R. Crespo López-Urrutia, I. C. Gebeshuber, M. Lang, H. P. Winter, J. Ullrich and F. Aumayr,
     Nucl. Instrum. Meth. B **265**, 346 (2007).

[84] *Novel method for unambiguous ion identification in mixed ion beams extracted from an electron beam ion trap,*
     W. Meissl, M. C. Simon, J. R. Crespo López-Urrutia, H. Tawara, J. Ullrich, F. Aumayr and H. P. Winter,
     Rev. Sci. Instrum. **77**, 093303 (2006).

[85] *https://www.veecoprobes.com/*

[86] *http://www.spmtips.com/products/hopg*

[87] *http://www.azom.com/*

[88] *Scanning tunneling microscopy observation of local damges induced on graphite surface by ion implantation,*
L. Porte, C. H. de Villeneuve and M. Phaner,
J. Vac. Sci. Techn. B **9**, 1064 (1991).

[89] *Scanning tunneling microscopy and atomic force microscopy study of graphite defects produced by bombarding with highly charged ions,*
K. Mochiji, S. Yamamoto, H. Shimizu, S. Ohtani, T. Seguchi and N. Kobayashi,
J. Appl. Phys. **82**, 6037 (1997).

[90] *STM studies of HCI-induced surface damage on highly oriented pyrolitic graphite,*
G. Hayderer, S. Cernusca, M. Schmid, P. Varga, H. P. Winter and F. Aumayr,
Phys. Scr. **T92**, 156 (2001).

[91] *Nanoscopic surface modification by slow ion bombardment,*
I.C. Gebeshuber, S. Cernusca, F. Aumayr and H.P. Winter,
Int. Jour. Mass Spect. **229**, 27 (2003).

[92] *Tracks of swift heavy ions in graphite studied by scanning tunneling microscopy,*
J. Liu, R. Neumann,C. Trautmann and C. Müller,
Phys. Rev. B **64**, 184115 (2001).

[93] *In-situ observation of surface modification induced by highly charged ion bombardment,*
R. Minniti, L. P. Ratliff and J. D. Gillaspy,
Phys. Scr. **92**, 22 (2001).

[94] *Creation of nanodiamonds by single impacts of highly charged ions upon graphite,*
T. Meguro, A. Hida, M. Suzuki, Y. Koguchi, H. Takai, Y. Yamamoto, K. Maeda and Y. Aoyagi,
Appl. Phys. Lett. **79**, 3866 (2001).

[95] *Nanoscale modification of electronic states of HOPG by the single impact of HCI,*
T. Meguro, Y. Yamaguchi, H. Fukagawa, H. Takai, N. Hanano,Y. Yamamoto, K. Kobashi and T. Ishii,
Nucl. Instrum. Meth. B **235**, 431 (2005).

[96] *SPM observation of nano-dots induced by slow highly charged ions,*
N. Nakamura, M. Terada, Y. Nakai, Y. Kanai, S. Ohtani, K. Komaki and Y. Yamazaki,
Nucl. Instrum. Meth. B **232**, 261 (2005).

[97] *Observation of an HCI-induced nano-dot on an HOPG surface with STM and AFM,*
M. Terada, N. Nakamura, Y. Nakai, Y. Kanai, S. Ohtani, K. Komaki and Y. Yamazaki,
Nucl. Instrum. Meth. B **235**, 452 (2005).

[98] *Nanodots formation with slow highly charged ions,*
Y. Yamazaki,
J.Phys.Conf.Proc. **72**, 1 (2007).

[99] *Observation of HCI-induced nanostructures with a scanning probe microscope,*
M. Tona, H. Watanabe, S. Takahashi, Y. Fujita, T. Abe, S. Jian, N. Nakamura, N. Yoshiyasu, C. Yamada, M. Sakurai and S. Ohtani,
J.Phys.Conf.Proc. **58**, 331 (2007).

[100] *Surface structure on Ar^+-ion irradiated graphite by scanning probe microscopy,*
B. An, S. Fukuyama, K. Yokogawa and M. Yoshimura,
Jpn. J. Appl. Phys. **39**, 3732 (2000).

[101] *Vacancy and interstitial defects at graphite surfaces: Scanning tunneling microscopic study of the structure, electronic property, and yield for ion-induced defect creation,*
J. R. Hahn and H. Kang,
Phys. Rev. B **60**, 6007 (1999).

[102] *http://www.antiquestoves.com/mica/0006.jpg*

[103] *http://www.pcimag.com/PCI/2003/05/Files/Images/82552.jpg*

[104] *Observation of defects on insulator surfaces following bombardment with slow Kr^{35+}, Xe^{44+}, Th^{74+}, and U^{70+} ions,*
D. Schneider, M.A. Briere, J. McDonald and W. Siekhaus,
Nucl. Instrum. Meth. B **87**, 156 (1994).

[105] *AFM studies of a new type of radiation defect on mica surfaces caused by highly charged ion impact,*
C. Ruehlicke, M.A. Briere and D. Schneider,
Nucl. Instrum. Meth. B **99**, 528 (1995).

[106] *Nanometer-size surface features produced by single, low energy highly charged ions,*
D.C. Parks, R. Bastasz, R.W. Schmieder and M. Stöckli,
J. Vac. Sci. Technol. B **13**, 941 (1995).

[107] *Friction force microscopy of heavy-ion irradiated mica,*
T. Hagen, S. Grafström, J. Ackermann, R. Neumann, C. Trautmann, J. Vetter and N. Angert,
J. Vac. Sci. Techn. B **12**, 1555 (1994).

[108] *Analysis of lateral force effects on the topography in scanning force microscopy,*
S. Grafström, J. Ackermann, T. Hagen, R. Neumann and O. Probst
J. Vac. Sci. Techn. B **12**, 1559 (1994).

[109] *Analysis of lateral force contribution to the topography in contact mode AFM,*
G. Shang, X. Qiu, C. Wang and C. Bai,
Appl. Phys. A **66**, 333 (1998).

[110] *Non-kinetic damage on insulating materials by highly charged ion bombardment,*
D. C. Parks, M. P. Stöckli, E. W. Bell, L. P. Ratliff, R. W. Schmieder, F. G. Serpa and J. D. Gillaspy,
Nucl. Instrum. Meth. B **134**, 46 (1998).

[111] *Creation of nano-hillocks on CaF$_2$ surfaces by single slow highly charged ions,*
A. S. El-Said, R. Heller, W. Meissl, R. Ritter, S. Facsko, C. Lemell, B. Solleder, I. C. Gebeshuber, G. Betz, M. Toulemonde, W. Möller, J. Burgdörfer and F. Aumayr,
submitted for publication.

[112] *On the nano-hillock formation induced by slow highly charged ions on insulator surfaces,*
C. Lemell, A. S. El-Said, W. Meissl, I. C. Gebeshuber, C. Trautmann, M. Toulemonde, J. Burgdörfer and F. Aumayr,
Sol.–State. Electronics **51**, 1398 (2007).

[113] *Transient thermal process after a high-energy heavy-ion irradiation of amorphous metals and semiconductors,*
M. Toulemonde, C. Dufour and E. Paumier,
Phys. Rev. B **44**, 362 (1992).

[114] *Transient thermal processes in heavy ion irradiation of crystalline inorganic insulators,*
M. Toulemonde, Ch. Dufour, A. Meftah and E. Paumier,
Nucl. Instrum. Meth. B **166**, 903 (2000).

[115] *A theorist's view of hillock formation on CaF_2,*
C. Lemell, B. Solleder, K. Tökesi and J. Burgdörfer,
Poster for the 3S'08 conference, St. Christoph, Austria, 2 - 8. 03. 2008.

[116] *Progress in projection maskless lithography,*
C. Klein, E. Platzgummer, H. Loeschner and G. Gross,
SPIE Newsroom (2008): http://spie.org/documents/Newsroom/Imported/1026/1026-2008-02-04.pdf.

[117] *Transmission of 3 keV Ne^{7+} ions through nanocapillaries etched in polymer foils: Evidence for capillary guiding,*
N. Stolterfoht, J.-H. Bremer, V. Hoffmann, R. Hellhammer, D. Fink, A. Petrov and B. Sulik,
Phys. Rev. Lett. **88**, 133201 (2002).

[118] *Production of a microbeam of slow highly charged ions with a tapered glass capillary,*
T. Ikeda, Y. Kanai, T. M. Kojima, Y. Iwai, T. Kambara, Y. Yamazaki, M. Hoshino, T. Nebiki and T. Narusawa,
Appl. Phys. Lett. **89**, 163502 (2006).